

Reply to Reviewer #2 (comments for Atmos. Chem. Phys. Discuss., 14, 26971–27038, 2014, A multi-year study of lower tropospheric aerosol variability and systematic relationships from four North American regions, by J. P. Sherman, et al.)

We thank anonymous reviewer #2 for her/his suggestions and include responses below each reviewer comment.

Comments

Reviewer Comment 1: Abstract: Line 32-33: States that AOP from 1996-2009 at BND and 1997-2009 at SGP are presented. Table 4 presents data on the trend but not the AOP measurements. One of the most important conclusions of the abstract is “Statistically-significant trends in σ_{sp} (decreasing), PM1 scattering fraction (decreasing), and b (increasing) are found at BND from 1996-2013 and at SGP from 1997- 2013.” However, there is not plot in the paper, nor the supplement showing this result. The paper needs such a plot to support this important conclusion, please add.

Authors’ response to comment 1: We agree with the reviewer and have made the below-listed changes to the manuscript.

Changes in manuscript: We have added time series plots of all AOPs whose trends are reported in Sect. 4.3. Plots of PM1 variables with the most notable, statistically-significant trends (σ_{sp} , R_{sp} , and b) are now shown in Figure 9 of the paper. We did not label the plots in Fig. 9 with letters, due to the fact that the plots are not discussed individually and the plot titles make identifying the plots obvious. Time series plots for the other AOPs whose trend results are included in Table 4 are placed in the Supplemental Materials (Fig(s). S24-S25). We also state in Sect. 4.3 that “*Visual examination of Figure 9 reveals that the trends in these AOPs since ~2009 are somewhat more pronounced than in earlier years, pointing out the pitfalls associated with trend analysis on short-term time series.*” Beyond this assertion, there is really not much more that we can say (without speculating) that has not already been discussed in Sect. 4.3.

Reviewer Comment 2: It is great that the authors incorporate uncertainties in their analysis; however, their presentation of uncertainty is confusing in several places. Line 357-358: “uncertainties can hence be neglected when comparing measurements made at different sites and times” “Neglected”??? There are no uncertainties? Seems that the authors want to say that the measurement uncertainty at one site is the same as the uncertainty at another site. Is this correct? The uncertainty is still there, it is just the same, hence can be “neglected”

Authors’ response to comment 2: We agree with the reviewer that this passage was poorly-worded and also believe that the paragraph as a whole needed improvement.

Changes in manuscript: We modified the entire paragraph in Sect. 2.4 containing this passage to better clarify our meaning: It now reads as follows:

“Identical nephelometers, PSAPs, calibration and correction methods are used at the four sites reported in this paper, with the exception of the late replacement of PSAP with the nearly-identical CLAP at BND. As a result, some contributions to the measurement uncertainties are nearly the same for different sites and

times and approximately cancel when comparing AOPs between different sites and times, as noted by Anderson et al. (1999). Examples include the nephelometer calibration and STP correction uncertainties. The nephelometer truncation correction uncertainties are also nearly the same, due to the fact that the scattering Ångström exponent used to correct for nephelometer truncation of forward-scattered light (Anderson and Ogren, 1998) exhibits little temporal variability at each of the four sites and is of similar magnitude for each site (Fig.2g). The PSAP unit-to-unit variability term can be neglected when comparing measurements made at the same site but cannot be neglected when comparing measurements made at different sites. The other uncertainty sources described above must be considered both for intra-site and inter-site AOP comparisons. We follow a similar methodology to that employed by Anderson et al. (1999). We consider the combined effect of all uncertainty sources which would not be expected to cancel or nearly-cancel when comparing AOPs measured at different sites or times. We refer to their combined effect as measurement precision uncertainty, using the same notation as Anderson et al. (1999). We note that Anderson et al. (1999) did not include the nephelometer RH correction uncertainty nor the PSAP calibration uncertainty in their reported measurement precision uncertainties so our reported measurement precision uncertainties may represent upper bounds. We use the measurement precision uncertainties (Table 3) for comparing AOPs measured at different sites and times. Differences in AOPs between sites/seasons are assessed by comparison with the measurement precision uncertainty ranges (Sect. 2.5). The uncertainties are reported for 1-hour averages but the values differ negligibly for averaging times larger than this (Sect. 1 of Supplemental Materials).”

Comment 3: I would suggest the authors use the terms precision and accuracy in their discussion. From https://en.wikipedia.org/wiki/Accuracy_and_precision#Common_definition

In the fields of [science](#), [engineering](#),], and [statistics](#), the accuracy of a [measurement](#) system is the degree of closeness of measurements of a [quantity](#) to that quantity's true [value](#).^[1] The precision of a measurement system, related to [reproducibility](#) and [repeatability](#), is the degree to which repeated measurements under unchanged conditions show the same [results](#).

Using these definitions, precision is uncertainty with an instrument and itself; while accuracy is between instruments. Hence, it seems that the author are saying that the uncertainty is the same an instrument with itself and between instruments. Can this be made clear?

When the author talk about “unit-to-unit variability” (Line 363), it is accuracy and for one unit it is precision. I would suggest using “accuracy” uncertainties instead of total as is done in Table 3. Also, may want to add a sentence defining these terms.

Authors’ response to comment 3: We respectfully disagree with the reviewer on this point. Accuracy refers to agreement with "truth". There is no reference instrument which can be assumed to serve as “truth” for the measurements used in this study. Hence the term “accuracy” does not apply with respect to the set of measurements used in this study. Precision can also apply to a method, i.e., the degree to which a collection of instruments agrees within itself. It's very hard to separate precision and accuracy in our methods, which is why we use the blanket term "uncertainty". Some of our corrections (truncation, Bond) are applied to improve the accuracy of the corrected value. Others, e.g., neph background subtraction, flowmeter calibrations, spot size determination, affect both precision and accuracy. It doesn't make sense to try and separate precision and accuracy uncertainties.

Changes in manuscript: None

Comment 4: Additionally, I do not believe that all the sites have the same instrument for the full duration of the measurement period even at a single site and hence instrument variability may be important even at a single site. Maybe the absorption measurements were conducted with the same instrument for the 2010-2013 period but was this the case at SGP for 1996-2013 period? Either it should be explicitly stated what serial number instrument was used at a single site or the accuracy uncertainty should be used.

Authors' response to comment 4: The same model nephelometer (TSI 3563) was used for the scattering measurements made at all sites for the entire period (see Table 1 of paper). Absorption data for SGP prior to 2010 is not used in this study (See Sect. 2.3). We have better clarified this in our revised Table 1. The PSAP at BND was replaced by the CLAP in 2012 (see Table 1) and the reviewer makes a good point in suggesting that the effect of this change should be considered as a source of uncertainty, if we are correctly interpreting her/him. In fact, an inter-comparison of BND PSAP versus CLAP -measured absorption coefficient was conducted over 13 months, with PSAP absorption ~2% higher than that measured by CLAP (See last paragraph of Sect. 2.2). This small difference is of similar magnitude to that found at other sites. Adding a 2% uncertainty for BND absorption in quadrature with the other sources of absorption uncertainty (Table S1 of Supplemental Materials) is strictly correct but results in negligible modification to the absorption coefficient uncertainty, due to the dominance of the unit-to-unit variability and calibration terms in the uncertainty (Table S1). For this reason, we do not include this term in the absorption coefficient uncertainty for BND. Also see our response to Reviewer Comment 3 as to why we choose not to use the term 'accuracy uncertainty'.

Changes in manuscript: We modified Table 1 to clearly state that SGP absorption data before 2010 was not used in the study.

Comment 5: I have a large issue with using an annual-mean value to determine an uncertainty of a measured parameter as is done with the scattering and absorption values. The article supplement provides uncertainty calculations in terms of percentages of the value measured; however, a mean value is then used to determine the uncertainty. This can be very confusing as the scattering has a larger uncertain (1.9 Mm^{-1}) than the absorption (0.52), while in fact the percentage uncertainty is larger for absorption. For scattering and absorption, percentages should be used and given in the tables and plots. Uncertainty in a measurements should not be given in term of an annual mean when a percentage could just as easily be given, such as for the scattering and absorption in Table 3. This could be very miss leading to other scientist that would just take the uncertainty and apply it to their measurements. Percentage uncertainties need to be calculated for each parameter in table 3 and then applied. The calculations are straight forwards and easy to apply but does take a little time. I feel this is very important to understanding the results of the paper. While applying this methodology is unlikely to change any of the conclusions, I feel it is important to maintain this standard as an example to other researchers where it could affect conclusions.

It is not clear why the annual averaged AOP in Figure 2 have lower uncertainties than the monthly averaged AOP. These uncertainties should be given as a percentage of the value not as a fixed value that depend on the annual mean.

Authors' response to comment 5: There appear to be three issues and we address each individually in our response:

#1. Use of annual-mean values when calculating uncertainties (e.g., Tables 3, S4, S5)

#2. Use of standard deviations vs. standard errors of the means

#3. Combining measurement uncertainties and atmospheric variability when comparing measured values (both inter- and intra-site).

#1: We modified Tables 3, S4, and S5 so that the uncertainties are now expressed as percentages. We agree with the reviewer that this is less confusing to the reader and facilitates the usage of uncertainties by others-provided that the reader understands the limitations of their usage. The use of percentages for $\Delta\sigma_{sp}$, $\Delta\sigma_{bsp}$, and $\Delta\sigma_{ap}$ also eliminates the need for the first three supplemental tables (Tables S1-S3), which stated these uncertainties for various values of σ_{sp} , σ_{bsp} , and σ_{ap} respectively. As a result, we have removed Tables S1-S3. The modified Table S4, (which is now labeled as Table S1, due to deletion of the first three tables) expresses the uncertainties $\Delta\sigma_{sp}$, $\Delta\sigma_{bsp}$, and $\Delta\sigma_{ap}$ as percentages, including the individual contributions from the uncertainty source terms. Strictly speaking, these fractional uncertainties depend weakly on the values σ_{sp} , σ_{bsp} , and σ_{ap} , through the noise terms. However, the noise contribution to total uncertainty is nearly negligible for averaging times of ≥ 1 hour (See revised Table S1) so the percentages can safely be applied under these conditions. We note this as a footnote in Table S2 of the revised Supplemental Materials and in Table 3 of the paper.

However, the uncertainties in other AOPs (e.g., the intensive AOPs) depend in a nonlinear fashion on the measured value, and cannot rigorously be represented as percentages. For these variables, we use approximate annual-mean values $\sigma_{sp,10}=30 \text{ Mm}^{-1}$, $\sigma_{ap,10}=3.0 \text{ Mm}^{-1}$, $R_{sp}=0.80$, $R_{ap}=0.88$, $b=0.14$, $\omega_0=0.91$, $\alpha_{sp}=2.0$, and $\alpha_{ap}=1.0$ to calculate fractional uncertainties. We encourage the reader (via a disclaimer in the Table 3 caption) to re-calculate these fractional uncertainties using site-specific AOP values if much different than those listed above, using equations provided in Sect. S1 of the Supplementary Materials to the manuscript.

#2. The choice of metric for representing variability (the error bars in figures) depends on the application. In this paper, our interest is in identifying significant differences in AOPs measured at different sites and times. For this application, the standard error of the mean is the appropriate metric to use. Specifically, we use 95% confidence intervals of mean values, which are related to the standard error of the mean (e.g., upper and lower error bar lengths are 1.96 standard errors of mean and given by slightly more complicated equation for 95% CIs of geometric mean).

#3. We cannot put measurement uncertainties on the figures, because the choice of measurement uncertainty depends on the goals of the analysis. If we are comparing stations, we will use one uncertainty value. If we are comparing different times at the same station, we would use a different uncertainty. We have plots that include traces (with standard errors of the mean; expressed as 95% CIs;) for multiple stations and times on the same plot, and there's no practical way to show all three "error" bars or to combine them. In light of that, we leave the figures as they are, i.e., optimized for comparisons of atmospheric variability. If a user wants to delve further into the comparison, they would have to refer to tables S1-S2 of Supplemental Materials and the accompanying uncertainty equations to assess significance of differences relative to measurement uncertainty.

Changes in Manuscript: We now express uncertainties in terms of percentages (Table 3, Tables S1-S2).

Comment 6: Details

Article – The ACP style is to indent at the start of paragraphs, why are the article's paragraph's not indented? This make things difficult to read.

Authors' response: We now indent the start of paragraphs. We do note that the paragraphs in the ACPD sample template are not indented, which is why we did not indent paragraphs in the manuscript.

Line 304-307 – Why is the font different on these lines?

Authors' response: We fixed the font in this and in a few other identified instances.

Line 349 – Two commas in a row.

Authors' response: Fixed

Line 345 – Additional spaces in sentence.

Authors' response: Fixed

Line 361 – Space between Fig. And 2g. There are a number of other examples of this, for example Fig.2 on page 1 of Supplemental Materials. Why where these simple things not fixed?

Authors' response: The ACPD sample template contains a space between the word Fig. and the corresponding number. Likewise, a space appears in the example for referencing figures, located at ACP webpage title “Manuscript Guidelines for Authors”.

http://www.atmospheric-chemistry-and-physics.net/for_authors/manuscript_preparation.html

For this reason, we leave the space in between Fig. and the number when referencing figures.

Table 1: Change to not take so much space vertically.

Authors' response: Fixed

Table 2: Why double space, fix so does not take so much space vertically.

Authors' response: Fixed

Table 3 Caption: Need space between numbers and units. I don't understand why this has not been corrected.

Authors' response: Fixed

Figure 2 and all other figures: Y-axis values should have label with the same number of figures, 2.0 and not 2

Authors' response: Fixed

Figure 3: Figures should be able to be understand independent of the text; hence, APP, BND and EGB need to be defined. The time period of the data presented need to be given. LST needs to be defined. Like “Day of Week” is the x-axis on the left, “Hour of Day” should be label on x-axis on right. Also, Week need to be capitalized.

Author's response: Acronyms for the sites are already defined in the paper (before reference to

figures) so they do not need to be defined again in figure caption, according to the ACP guide for manuscript preparation, located at

http://www.atmospheric-chemistry-and-physics.net/for_authors/manuscript_preparation.html. With regards to figure captions, the guide states that...

“Figure captions: Each illustration should have a concise but descriptive caption. The abbreviations used in the figure must be defined, unless they are common abbreviations or have already been defined in the text. Figure captions should be included in the text file and not in the figure files. “

For further clarity, we spell out each site acronym in the first figure (Fig. 1) where they are used. We also fixed the other items suggested above by the reviewer.

Figure 9 and 10: Caption needs to give time periods and define acronyms.

Author’s response: We added time periods. See our response to previous comment regarding acronyms.

Supplemental Materials: Why are the paragraphs not right justified like the main article?

Authors’ response: Fixed

Supplemental Materials – Page 2: Space between value and unit, i.e. 450 nm, 550 nm, and 700

Authors’ response: Fixed

Supplemental Materials – Page 3: Space between value and unit, i.e. 4 Mm⁻¹ etc.

Authors’ response: Fixed

1 **A multi-year study of lower tropospheric aerosol variability**
2 **and systematic relationships from four North American**
3 **regions**

4 **J.P. Sherman¹, P.J. Sheridan², J.A. Ogren², E. Andrews³, D. Hageman³,**
5 **L. Schmeisser³, A. Jefferson³, and S. Sharma⁴**

6 [1] {Dept. Physics and Astronomy, Appalachian State University, 525 Rivers St, CAP
7 Building, Room 231, Boone, NC, USA 28608}

8 [2] {NOAA, Earth Systems Research Laboratory, Global Monitoring Division/GMD-1, 325
9 Broadway, Boulder, CO USA 80305}

10 [3] {CIRES, University of Colorado, Boulder, Colorado, 80309}

11 [4] {Environment Canada, 4905 Dufferin St, Toronto, ON, M3H 5T4 Canada}

12 Correspondence to: J.P. Sherman (shermanjp@appstate.edu)

13

14 **Abstract**

15 Hourly-averaged aerosol optical properties (AOPs) measured over the years 2010-2013 at
16 four continental North American NOAA Earth System Research Laboratory (NOAA/ESRL)
17 cooperative aerosol network sites – Southern Great Plains near Lamont, OK (SGP), Bondville,
18 IL (BND), Appalachian State University in Boone, NC (APP), and Egbert, Ontario, Canada
19 (EGB) are analyzed. Aerosol optical properties measured over 1996-2009 at BND and 1997-
20 2009 at SGP are also presented. The aerosol sources and types in the four regions differ
21 enough so as to collectively represent rural, anthropogenically-perturbed air conditions over
22 much of eastern continental North America. Temporal AOP variability on monthly, weekly,
23 and diurnal timescales is presented for each site. Differences in annually-averaged AOPs and
24 those for individual months at the four sites are used to examine regional AOP variability.
25 Temporal and regional variability are placed in the context of reported aerosol chemistry at the
26 sites, meteorological measurements (wind direction, temperature), and reported regional
27 mixing layer heights. Basic trend analysis is conducted for selected AOPs at the long-term sites
28 (BND and SGP). Systematic relationships among AOPs are also presented.

29 Seasonal variability in PM1 (sub-1 μ m particulate matter) scattering and absorption
30 coefficients at 550 nm (σ_{sp} and σ_{ap} , respectively) and most of the other PM1 AOPs is much
31 larger than day of week and diurnal variability at all sites. All sites demonstrate summer σ_{sp}
32 and σ_{ap} peaks. Scattering coefficient decreases by a factor of 2-4 in September-October and
33 coincides with minimum single-scattering albedo (ω_0) and maximum hemispheric backscatter
34 fraction (b). The co-variation of ω_0 and b lead to insignificant annual cycles in top-of-
35 atmosphere direct radiative forcing efficiency (DRFE) at APP and SGP. Much larger annual
36 DRFE cycle amplitudes are observed at EGB (~40%) and BND (~25%), with least negative
37 DRFE in September-October at both sites. Secondary winter peaks in σ_{sp} are observed at all
38 sites except APP. Amplitudes of diurnal and weekly cycles in σ_{ap} at the sites are larger for all
39 seasons than those of σ_{sp} , with largest differences occurring in summer. The weekly and
40 diurnal cycle amplitudes of most intensive AOPs (e.g., those derived from ratios of measured
41 σ_{sp} and σ_{ap}) are minimal in most cases, especially those related to parameterizations of aerosol
42 size distribution.

43 Statistically significant trends in σ_{sp} (decreasing), PM1 scattering fraction (decreasing), and
44 b (increasing) are found at BND from 1996-2013 and at SGP from 1997-2013. A statistically
45 significant decreasing trend in PM10 scattering Ångström exponent is also observed for SGP
46 but not BND. Most systematic relationships among AOPs are similar for the four sites and are
47 adequately described for individual seasons by annually-averaged relationships, although
48 relationships involving absorption Ångström exponent vary with site and season.

49

50 **1 Introduction**

51 Predictions of future climate change resulting from projected increases in carbon
52 dioxide are limited by large uncertainties in the direct and indirect radiative forcing due
53 to aerosols (Andreae et al., 2005). Measurement-based estimates of globally-averaged
54 aerosol direct radiative forcing (DRF) are 55-80% greater than the model-based estimates
55 (Yu et al., 2009). The measurement-model differences are even larger on regional scales and
56 for the anthropogenic component (Yu et al., 2009). Such measurement-model discrepancies
57 are the result of a combination of differences in aerosol amount, single-scattering albedo,
58 surface albedo, and radiative transfer schemes (Yu et al., 2006). One of the high-priority
59 tasks recommended to reduce the uncertainty in aerosol radiative effects is to “*Maintain,*

60 *enhance, and expand the surface observation networks measuring aerosol optical properties*
61 *for satellite retrieval validation, model evaluation, and climate change assessments”* (Kahn et
62 al., 2009).

63 Studies based on long-term measurements made by global surface-based aerosol
64 monitoring networks such as NASA’s Aerosol Robotic Network (AERONET) and
65 NOAA’s Earth System Research Laboratory (NOAA/ESRL) have contributed to improved
66 understanding of mean values of aerosol optical properties (AOPs), spatial and
67 temporal AOP variability, and relationships among some AOPs (Dubovik et al., 2005;
68 Delene and Ogren, 2002; hereafter referred to as D&O2002). The US-based Interagency
69 Monitoring of Protected Visual Environments (IMPROVE) network (Malm et al., 2004)
70 has conducted similar studies using speciated aerosol mass concentrations, aerosol light
71 scattering coefficient (at some sites), and reconstructed aerosol light extinction coefficient
72 measurements in remote areas of the US. Recent long-term trend studies based on data
73 from surface networks indicated that aerosol optical depth (Li et al., 2014; Yoon, 2012)
74 and lower tropospheric aerosol light scattering coefficient (Collaud-Coen et al., 2013;
75 hereafter referred to as CC2013) decreased at a majority of North American aerosol
76 monitoring sites. Hand et al. (2014) reported large reductions of up to 50% in reconstructed
77 aerosol visible light extinction for the 20% haziest days annually at IMPROVE sites in
78 the US from 2002-2011, with the largest decreases in the eastern US. Through trend
79 analysis of speciated aerosol mass concentrations and emissions inventories, Hand et al.
80 (2014) showed that reductions in US SO₂ emissions have likely played a major role in the
81 reduced aerosol light extinction, particularly in the eastern US. Murphy et al. (2011)
82 applied trend analysis to data from IMPROVE sites across the US to show that elemental
83 carbon aerosol mass concentrations decreased by over 25% between 1990-2004, with
84 reductions during winter months close to 50%. Region- and season-dependent changes in
85 emissions of aerosols and precursor gases may result in changes in mean values and
86 variability of aerosol optical and microphysical properties. However, few long-term studies
87 of aerosol intensive properties (e.g., properties that are independent of aerosol loading,
88 such as single scattering albedo, asymmetry parameter, and direct radiative forcing
89 efficiency) have been conducted in or over multiple North American regions.

90 Surface-based networks employing in situ measurements of aerosol optical properties,

91 such as the WMO Global Atmosphere Watch (GAW) and NOAA/ESRL aerosol networks
92 are particularly well- suited for studies of aerosol variability on a variety of temporal
93 scales under both clear and cloudy conditions. An additional advantage of the in situ
94 measurements is the ability to derive single-scattering albedo under low aerosol loading
95 conditions. Column-averaged single scattering albedo derived from sky radiance
96 measurements made by Cimel sun/sky radiometers as part of AERONET possess high
97 uncertainties at the lower aerosol optical depths (AOD) typical of most rural North
98 American sites (Dubovik et al., 2000). A weakness of many in situ surface aerosol
99 measurement systems is the inability to determine the hygroscopic dependence of aerosol
100 light scattering. Many aerosol monitoring stations in the NOAA/ESRL and GAW networks
101 follow similar sampling protocols where the aerosols are dried to decouple the aerosol
102 properties from local variations in relative humidity (RH). Another concern is the
103 uncertainty as to when and under what conditions the near-surface measurements are
104 representative of the atmospheric column at each site. The first problem can be addressed
105 through the use of humidified light scattering measurements (e.g., Sheridan et al., 2001),
106 which are or have been made at a few ESRL network sites, including three of the four sites
107 reported in this paper. The second issue has been investigated through multi-year aircraft
108 measurement programs over instrumented surface sites. At the Southern Great Plains (near
109 Lamont, OK) and Bondville, IL sites respectively, Andrews et al. (2004) and Sheridan et
110 al. (2012) reported that median values of key low-RH intensive AOPs exhibited little
111 statistical variability up to ~2 km altitude and that long-term median values could be well-
112 approximated by the near-surface values. Instantaneous measurements of the near-surface
113 properties were often poorly-correlated with those of the column at these sites. (Andrews et
114 al., 2004; Sheridan et al., 2012).

115 D&O2002 reported multi-year measurements of AOPs at four North American sites that
116 were used to (1) highlight the need to quantify both aerosol extensive properties (e.g.,
117 properties that depend on aerosol amount) and aerosol intensive properties on regional scales
118 over at least a 1-year period; and (2) conclude that global AOD measurements made daily
119 by satellites, combined with in situ measurements of regionally-representative intensive
120 AOPs, are likely sufficient to determine aerosol DRF with a relatively small amount
121 of uncertainty. One limitation of their study was the then-lack of NOAA/ ESRL network
122 sites in the more populous eastern continental North America. D&O2002 also studied

123 systematic relationships between aerosol loading (using scattering coefficient as a proxy) and
124 other AOPs. D&O2002 argued the importance of such relationships for applications
125 including inversion of remote sensing data, whereby a dynamic model could be used to
126 specify the constraining AOPs as a function of aerosol loading.

127 The study described here utilizes four years (2010-2013) of continuous measurements of
128 aerosol light absorption, scattering, and hemispheric backscattering coefficients made at
129 four continental North American sites (Fig. 1; Table 1) in the NOAA/ESRL cooperative
130 aerosol network: (i) the Appalachian Atmospheric Interdisciplinary Research facility at
131 Appalachian State University (APP) in Boone, NC- located in the southern Appalachian
132 mountain region of the southeastern US.; (ii) the Bondville Environmental and Atmospheric
133 Research Site (BND), located in the agricultural Midwestern US near Champaign, IL; (iii)
134 the Environment Canada monitoring station at Egbert, Ontario (EGB) - located in the
135 agricultural and forested rural region north/ northwest of Toronto; and (iv) the Southern
136 Great Plains Central Facility (SGP) of the US Department of Energy Atmospheric Radiation
137 Measurement program (SGP), located in the southern plains of the US in rural Oklahoma.
138 We use these measurements to calculate several key AOPs relevant to aerosol radiative
139 forcing (Table 2). Hourly-averaged AOPs are binned by month, day of week, and hour of
140 day to study annual, weekly, and diurnal AOP cycles at each site. AOPs are also binned by
141 wind sector for each season to study the role of known regional aerosol sources on AOPs
142 and their variability at each site. Published aerosol chemistry for each site and its seasonal
143 variability are used along with published mixing layer heights for each region and
144 monthly median temperatures at the sites to help explain the AOP cycles at each site and
145 differences among sites. Basic trend analysis is conducted for selected AOPs at the long-
146 term sites (BND and SGP). Systematic relationships among AOPs are also presented.

147 The objectives are to

- 148 (1) provide an explanation of temporal and regional AOP variability that is consistent with
149 meteorology, regional aerosol sources, and reported aerosol chemistry at the sites;
- 150 (2) identify possible AOP trends at the long-term sites (SGP and BND);
- 151 (3) determine whether systematic relationships exist for key aerosol properties relevant to
152 aerosol DRF calculations.

153 In addition to our use of meteorology and published aerosol chemistry to interpret the AOP
154 variability, this study differs from the D&O2002 paper in three respects:

155 (1) The time period of the study is different, which allows for us to compare (at least for
156 BND and SGP) how the AOPs have changed in the intervening years;

157 (2) This paper has a focus on continental sites, whereas D&O2002's four sites included an
158 Arctic site and a marine site;

159 (3) We report the following for individual seasons: (a) diurnal and weekly AOP variability,
160 and (b) some systematic relationships involving aerosol absorption Ångström exponent.
161 D&O2002 reported select AOPs for full years.
162

163 **2 Methodology**

164 **2.1 Air sampling infrastructure at the sites**

165 The APP, BND, EGB, and SGP sites are all designed with similar inlet systems following
166 established NOAA/ESRL and GAW aerosol sampling protocols (e.g., Sheridan et al.,
167 2001; WMO, 2003). To minimize contamination from local activities around the stations,
168 ambient aerosols are sampled from the top of sampling stacks that are well above the
169 surrounding terrain. The top of the stack is 10 m above the ground at BND, EGB, and
170 SGP. The sampling inlet at APP is located at the top of a 34 m tall tower in order to
171 sample aerosols at a height > 5 m above the surrounding tree canopy. To reduce the
172 confounding effects of relative humidity (RH) on the aerosol measurements, the sample air
173 is gently heated when needed at all sites except EGB to achieve sample line and
174 instrument $\text{RH} \leq 40\%$ (Sheridan et al., 2001). Nephelometer instrument RH at EGB exceeds
175 40% for a majority of hours in July-September but the moderately-elevated instrument RH
176 during these months is not believed to have any substantial impact on the results presented
177 in this paper (Sect. S3 of Supplementary Materials).

178 All of the sites except EGB use a switched impactor system (e.g., Sheridan et al.,
179 2001) to alternate between sub- $10\mu\text{m}$ ($D_p < 10 \mu\text{m}$) and sub- $1\mu\text{m}$ ($D_p < 1 \mu\text{m}$)
180 aerodynamic diameter particle size ranges. We refer to the sub- $10\mu\text{m}$ and sub- $1\mu\text{m}$
181 particle size cut ranges using the common convention PM₁₀ and PM₁, respectively,
182 where PM is the acronym for *particulate matter*. APP and SGP size-cut switching occurs
183 every 15 min and 30 min, respectively, in order to facilitate ramping of the RH in the
184 humidograph system that is used to measure the hygroscopic dependence of light

185 scattering (Sheridan et al., 2001). Humidograph data are not reported in this study. Size-
186 cut switching at BND, where there is currently no humidograph system, occurs every six
187 minutes. Aerosol concentrations and optical properties typically demonstrate little change
188 on timescales less than one hour at APP, BND, and SGP so it is assumed that the same
189 aerosols are sampled for both size cuts at these switching rates over a large majority of
190 hours. The EGB system uses a 1 μm cyclone to achieve a fixed $D_p < 1 \mu\text{m}$ particle size
191 cut so PM10 aerosol properties are not available for EGB. Descriptions of the basic inlet
192 design and sampling strategy, including flow rates, tubing sizes and estimated aerosol
193 losses are provided elsewhere (Sheridan et al., 2001; D&O2002).

194 **2.2 Measurements and instruments**

195 This study reports on several primary aerosol measurements, including aerosol light
196 scattering (σ_{sp}), hemispheric backscattering (σ_{bsp}), and absorption (σ_{ap}) coefficients (Table
197 2). Each of these parameters is measured for both the PM10 and PM1 size ranges (only
198 PM1 for EGB) and used to calculate the radiative effects of sub-1 μm particles (PM1).
199 Variability of AOPs measured at the APP, BND, and SGP sites over the 2010-2013 time
200 period is similar for the PM10 and PM1 size cuts so this paper focuses primarily on PM1
201 AOPs (Sect. 2.5) for consistency with EGB measurements. Annually-averaged PM10 AOPs
202 and their annual cycles are included in the Supplementary Materials that accompany this
203 paper (Table S5 and Fig. S8)

204 A three-wavelength (3- λ) integrating nephelometer (Model 3563, TSI Inc., St. Paul, MN) is
205 used at all sites for measurement of σ_{sp} (angular range of 7° - 170°) and σ_{bsp} (angular range
206 of 90° - 170°). Aerosol light absorption coefficients are determined by filter-based
207 instruments that make measurements at wavelengths close to those of the TSI
208 nephelometer (Table 1). A 3- λ Particle Soot Absorption Photometer (PSAP, Radiance
209 Research, Seattle, WA) is used at APP and SGP for the entire dataset and at BND for a
210 majority of the study period. A single wavelength (1- λ) PSAP is used at EGB. The
211 PSAPs are modified by placing a small ($\sim 5 \text{ W}$) heater on their internal inlet lines at the
212 connection with the optical block. The temperature of the metal optical block is kept a few
213 degrees higher than the incoming sample air temperature so the RH of the air stream at the
214 sample and reference filters remains relatively low. The heater is not actively controlled

215 to maintain a specific RH, but RH variability at low RH is not believed to influence the
216 measurements as strongly as RH variability at high RH (Anderson et al., 2003). Laboratory
217 tests indicate that the heater keeps the RH at the filters below 40% most of the time. An
218 RH of 50% at the filter is exceeded only during sampling of very humid air (Sheridan et
219 al., 2012). A new light absorption instrument (Continuous Light Absorption Photometer,
220 CLAP) was recently developed by NOAA/ESRL to eventually replace the PSAP at all
221 stations in the NOAA/ESRL network (Ogren et al., 2013). The CLAP is similar to the
222 PSAP in that particles are collected on a filter of the same material as used in the PSAP
223 and light transmission through the filter is monitored continuously. A major difference
224 between CLAP and PSAP is that instead of a single sample spot, the CLAP has eight
225 sample spots. CLAP filter spots are selected by solenoids that switch to the next sample
226 spot once the filter transmittance drops below a desired limit (typically 0.7). Thus, the
227 CLAP can run eight times as long as the PSAP before requiring a filter change. The
228 similarity in the CLAP and PSAP instrument designs facilitate the same corrections to the
229 measured σ_{ap} . The CLAP replaced the PSAP at BND in March 2012, after a 13-month
230 instrument inter-comparison period. The PSAP/CLAP comparisons made during the
231 overlap period at BND indicate that the CLAP-measured σ_{ap} , when adjusted to common
232 wavelengths, is approximately 2% lower than PSAP-measured σ_{ap} for each of the three
233 measurement wavelengths (Table 1). The CLAP comes with a small heater built into the
234 optics block and is controlled to a set temperature, typically 39 °C to minimize RH effects
235 during sampling.

236 **2.3 Data processing, quality assurance, and calculated AOPs**

237 Software developed at NOAA is used to log the data at the sites, automatically transmit
238 the data to NOAA, and ingest the data into the NOAA database. The database is accessible
239 to the individual site mentors via virtual machine software. The virtual machine software
240 includes a graphical user interface for reviewing and editing data as well as tools for
241 extracting the data in a variety of formats and for desired averaging times. The data
242 acquisition, processing and virtual machine software, along with documentation, are open-
243 source and freely available from NOAA (<http://www.esrl.noaa.gov/gmd/aero/sw.html>).
244 Quality-assured data products for each site in the NOAA/ESRL network are uploaded to
245 the World Data Centre for Aerosols and made available at <http://ebas.nilu.no/Default.aspx>.

246 The data products available include hourly-averaged aerosol number concentrations (not
247 presented in this paper), σ_{sp} , σ_{bsp} , and σ_{ap} for the PM10 and PM1 size cuts.

248 Data quality assurance review for each site is typically performed by the site mentor on a
249 weekly basis. Data during periods of instrument or sampling problems and during
250 times of instrument maintenance are invalidated. Absorption data are flagged for periods
251 when the PSAP or CLAP filter transmission drops to less than 0.7 and invalidated when
252 the filter transmission drops below 0.5 because high filter loading increases the σ_{ap}
253 measurement uncertainty (Bond et al., 1999). The lack of PSAP filter changes on weekends
254 at SGP leads to an under-representation of quality-assured Sunday (all day) and Monday
255 (early morning) σ_{ap} hours over the period of this study. Quality-assured σ_{ap} data at SGP
256 are only available for 38% of Sunday thru Monday morning hours during 2010-2013,
257 versus 70-80% of the hours for the rest of the week. Weekend days with low σ_{ap} are thus
258 well- represented at SGP while weekend days with high σ_{ap} (leading to over-loaded PSAP
259 filters) are under-represented. PSAP filters are changed on weekends at the other sites.

260 Light absorption coefficient measurements at SGP are particularly sensitive to ambient RH
261 fluctuations due to air conditioning cycles, particularly during hot, humid summers. CC2013
262 did not use SGP σ_{ap} data in their trend analysis for this reason. Excessively high
263 temperatures during the summer months of June-August (and the early part of September)
264 2010-2012 resulted in high daytime dew points that often were as high as 20 to 22 °C during
265 the late afternoon. The high sample humidity coincided with unusually high noise in the
266 PSAP. The hours with noisy σ_{ap} data were removed. On average this resulted in a 15%
267 loss or 3.6 hours per day in the data. Since this time, effort was made to lower the sample
268 RH through insulation of the optics block, use of a Nafion drier on the instrument inlet and
269 rerouting the trailer ventilation. Despite the data loss, the SGP summertime σ_{ap} data does not
270 exhibit a remarkable difference compared to the other sites nor does the 2010-2012 time
271 period vary significantly from 2013, when the noise was not as apparent. We include the
272 SGP σ_{ap} data in this paper for the 2010-2013 seasonal, weekly and diurnal cycle studies and
273 the systematic relationships among AOPs. We do not include σ_{ap} or AOPs calculated using
274 σ_{ap} as part of the long term trend analysis.

275 The four NOAA-ESRL network sites discussed in this paper are located such that there

276 are no major local aerosol sources in the predominant upwind directions, although there are
277 some aerosol sources that are typically downwind but that may occasionally be sampled.
278 Brief spikes in aerosol number concentrations, σ_{sp} , σ_{bsp} , and/or σ_{ap} are flagged as local
279 contamination by the site mentor. These spikes are usually 15-20 minutes or less in
280 duration and often coincide with vehicular traffic near the sites or times of peak morning
281 commuter traffic. Broader aerosol peaks are typically retained, as they are characteristic of
282 the sampling environment of the station. One example of a broader aerosol peak not
283 marked as contaminated is elevated σ_{ap} which often persists for hours during mornings
284 with surface inversions or during periods with humid, stagnant air masses.

285 Hourly averages of σ_{sp} , σ_{bsp} , and σ_{ap} are generated after the data have passed the quality
286 assurance tests. The hourly-averaged σ_{sp} and σ_{bsp} are adjusted to conditions of standard
287 temperature and pressure ($T=273.15$ K, $P=1013.25$ hPa) to facilitate σ_{sp} and σ_{bsp} comparisons
288 among the sites. TSI nephelometer measurements are corrected for nephelometer angular
289 non-idealities including truncation effects (Anderson and Ogren, 1998). PSAP- and CLAP-
290 measured σ_{ap} values are corrected for sample area, flow rate, and non-idealities in the
291 manufacturer's calibration as described in Bond et al. (1999) and Ogren (2010). Absorption
292 Ångström exponent values are used to adjust the spectral σ_{ap} values to those at the
293 nephelometer wavelengths so that intensive AOPs involving both instruments (Table 2) can
294 be calculated.

295 The primary measurements σ_{sp} , σ_{bsp} , and σ_{ap} are used to derive several aerosol properties
296 (Table 2) used in radiative transfer calculations (Haywood and Shine, 1995). These
297 properties have been described in many previous papers (e.g., Sheridan et al., 2001;
298 D&O2002) so only a brief discussion follows. The light extinction coefficient (σ_{ep}) is the sum
299 of the scattering and absorption coefficients. The single-scattering albedo (ω_0) is the fraction
300 of extinction due to scattering, with lower values of ω_0 corresponding to stronger aerosol
301 light absorption. The hemispheric backscatter fraction (b) represents the fraction of light
302 scattered into the backward hemisphere in the nephelometer and provides qualitative
303 information on aerosol size, with larger values of b corresponding to optically active
304 particles with smaller diameters. The scattering and absorption Ångström exponents (α_{sp}
305 and α_{ap}) describe the wavelength dependence of light scattering and absorption,

306 respectively. The scattering Ångström exponent (typically in the range $0 \leq \alpha_{sp} \leq 3$) provides
307 semi-quantitative information about the aerosol size distribution, with larger values of α_{sp}
308 corresponding to size distributions dominated by smaller particles (van de Hulst, 1957).
309 The absorption Ångström exponent can provide information on aerosol type for certain
310 aerosols (e.g., Cazorla et al., 2013; Bergstrom, et al., 2007). For example, dust and some
311 types of organic carbon (OC) absorb light strongly in the near-UV and blue-violet regions
312 of the electromagnetic spectrum (the so-called “brown carbon”), corresponding to $\alpha_{ap} > 1$
313 (Cazorla et al., 2013; Costabile et al., 2013). Absorption by black carbon (BC) decreases as
314 λ^{-1} in the near-UV through near-IR, corresponding to $\alpha_{ap} = 1$ (Bergstrom et al., 2002). The
315 sub-1 μm scattering and absorption fractions R_{sp} and R_{ap} , respectively, indicate the
316 fractions of PM10 light scattering and absorption due to PM1 particles and serve as a
317 rough proxy for the “fine-mode” fraction of scattering and absorption coefficients.

318 Haywood and Shine (1995) presented simple equations (Table 2) for calculating top-of-
319 atmosphere (TOA) aerosol DRF and direct radiative forcing efficiency (DRFE) for an
320 optically-thin, partially- absorbing atmosphere. DRFE represents the DRF per unit AOD
321 and is to first-order independent of AOD. If globally-averaged values for all non-aerosol
322 parameters are used (Table 2), the simple equation for DRFE provides a means for
323 comparing the intrinsic forcing efficiency of the aerosols measured at different sites and
324 times, through DRFE dependence on ω_0 and on up-scatter fraction β . The DRFE values
325 themselves are only approximations when globally-averaged values are used. Up-scatter
326 fraction represents the fraction of incoming solar radiation that is scattered by
327 atmospheric aerosols back to space. Up-scatter fraction has been related to b by the
328 approximation of Wiscombe and Grams (1976). A second-order curve fit of the points in
329 their Fig. 3 as reported in Sheridan and Ogren (1999) provides the parameterization shown in
330 Table 2.

331 **2.4 Measurement uncertainties**

332 Detailed measurement uncertainty calculations and discussions are provided in Sect. S1
333 of the Supplemental Materials and are briefly summarized here. The major sources of
334 uncertainty in σ_{sp} and σ_{bsp} measured by the TSI 3563 nephelometer are (1) instrumental
335 noise; (2) uncertainty in the nephelometer calibration using filtered air and CO₂ gases; (3)

336 nephelometer calibration variability; (4) uncertainties in the correction for nephelometer
337 angular non-idealities, which result in under-estimation (e.g., truncation) of light scattered
338 in the near-forward direction; (5) uncertainty in correcting σ_{sp} and σ_{bsp} to standard
339 temperature and pressure (STP) conditions; and (6) uncertainties in correcting σ_{sp} and σ_{bsp} to
340 40% RH during humid conditions. Detailed accounts of uncertainty sources (1)-(5) are given
341 in Anderson and Ogren (1998), Anderson et al. (1999), and Sheridan et al. (2002). The major
342 sources of uncertainty in σ_{ap} measured by the PSAP are (1) instrumental noise; (2) unit-to-
343 unit instrumental variability; and (3) uncertainty in the calibration of PSAP-measured σ_{ap} ,
344 using extinction minus scattering as a reference method (Bond et al., 1999).
345 Uncertainties in the PSAP spot size and flow rate corrections are often incorporated into the
346 unit-to-unit variability term (Müller et al., 2011; Anderson et al., 1999). The total
347 measurement uncertainties $\Delta\sigma_{sp}$, $\Delta\sigma_{bsp}$, and $\Delta\sigma_{ap}$ are calculated by adding the major
348 source contributions in quadrature (Anderson and Ogren, 1998). Standard error
349 propagation techniques are applied (Sect. S1 of Supplemental Materials) to calculate
350 uncertainties in intensive AOPs, once $\Delta\sigma_{sp}$, $\Delta\sigma_{bsp}$, and $\Delta\sigma_{ap}$ are estimated and adjustments
351 made for correlations among σ_{sp} , σ_{bsp} , and σ_{ap} (Tables 3, S1-S2). Our reported uncertainties
352 are 95% confidence intervals.

353 Identical nephelometers, PSAPs, calibration and correction methods are used at the
354 four sites reported in this paper, with the exception of the late replacement of PSAP with
355 the nearly-identical CLAP at BND. As a result, some contributions to the measurement
356 uncertainties are nearly the same for different sites and times and approximately cancel when
357 comparing AOPs between different sites and times, as noted by Anderson et al. (1999).
358 Examples include the nephelometer calibration and STP correction uncertainties. The
359 nephelometer truncation correction uncertainties are also nearly the same, due to the fact that
360 the may be neglected when comparing measurements made at different sites or made at
361 different times at the same site. This was discussed in detail by Anderson and Ogren (1998)
362 and by Anderson et al. (1999). The nephelometer calibration, truncation, and STP
363 correction uncertainties are likely very similar for all sites and seasons studied in this
364 paper. The uncertainties can hence be neglected when comparing measurements made at
365 different sites and times, as was done by Anderson et al. (1999). Scattering Ångström
366 exponent used to correct for nephelometer truncation of forward-scattered lighting

367 (Anderson and Ogren, 1998) exhibits little temporal variability at ~~each of the four a given~~
368 sites and is of similar magnitude for each site ~~reported in this paper~~ (Fig. 2g).
369 ~~Nephelometers at all sites are calibrated using CO₂ and filtered air with identical protocols.~~
370 The PSAP unit-to-unit variability term can be neglected when comparing measurements
371 made at the same site but cannot be neglected when comparing measurements made at
372 different sites. The other uncertainty sources described above must be considered both for
373 intra-site and inter-site AOP comparisons. We follow a similar methodology to that
374 employed by Anderson et al. (1999). We consider the combined effect of all uncertainty
375 sources which would not be expected to cancel or nearly-cancel when comparing AOPs
376 measured at different sites or times. We refer to their combined effect as measurement
377 precision uncertainty, using the same notation as Anderson et al. (1999). We note that
378 Anderson et al. (1999) did not include the nephelometer RH correction uncertainty nor the
379 PSAP calibration uncertainty in their reported measurement precision uncertainties so our
380 reported measurement precision uncertainties may represent upper bounds. We use the
381 measurement precision uncertainties ~~calculated from near annually averaged aerosol optical~~
382 ~~properties at the four sites~~ (Table 3) for comparing AOPs measured at different sites and
383 times. Differences in AOPs between sites/seasons are assessed by comparison with the
384 measurement precision uncertainty ranges (Sect. 2.5). The uncertainties are reported for
385 1-hour averages but the values differ negligibly for averaging times larger than this (Sect.
386 1 of Supplemental Materials).

387 2.5 Data analysis methods

388 All statistics reported in this paper are based on hourly-averaged, quality-assured σ_{sp} , σ_{bsp} ,
389 and σ_{ap} measurements made continuously or near-continuously at APP, BND, EGB, and SGP
390 over the 2010-2013 period. We report only the results for the PM1 size cut at APP, BND,
391 and SGP so as to minimize redundancy and to simplify comparisons with PM1 AOPs
392 measured at EGB. The only exceptions are the use of the more-relevant PM10 scattering
393 Ångström exponent and the sub-1 μ m scattering and absorption fractions (R_{sp} and R_{ap}),
394 calculated as the ratios of PM1/ PM10 σ_{sp} and σ_{ap} , respectively (Table 2). PM10 AOP
395 variability at APP, BND, and SGP is reported in the Supplemental Materials (Fig. S8 and
396 Table S5). The intensive AOPs (Table 2) are calculated for each hour, using the hourly-
397 averaged σ_{sp} , σ_{bsp} , and σ_{ap} values. For brevity, only AOPs at 550 nm are presented with the

398 exception of the wavelength dependent α_{sp} and α_{ap} . Scattering and absorption Ångström
399 exponents are calculated based on the 450 nm and 700 nm wavelength. We follow a similar
400 approach to that taken by D&O2002 and Andrews et al. (2011) and only use hours for
401 which PM1 σ_{sp} at 550 nm is at least 1.0 Mm^{-1} to calculate the intensive AOP statistics,
402 so as to reduce noise resulting from taking ratios of two small quantities (Table 2).
403 Filtering the intensive AOPs for low- σ_{sp} hours discards 1.4% of the hours at APP, 0.1%
404 at BND, 1.8% at EGB, and 0.5% at SGP. These percentages are uniform across seasons,
405 except for slightly higher percentages during fall at EGB and SGP (Table S3). We use all
406 hours in calculating σ_{ap} , σ_{sp} and σ_{bsp} statistics, to avoid a bias toward ‘less clean’
407 conditions. Lack of PM10 measurements and use of a single-wavelength PSAP preclude
408 calculation of R_{sp} , R_{ap} , and α_{ap} at EGB.

409 **2.5.1 Temporal cycle analysis**

410 Hourly-averaged and quality-assured AOPs are binned by month, day of week, and hour
411 of day to study their annual, weekly, and diurnal cycles, respectively (Sect. 4.1). Geometric
412 means and 95% confidence intervals of the geometric means are calculated for the binned
413 σ_{sp} and σ_{ap} , whose distributions are closer to log-normal than normal. Arithmetic means
414 and 95% confidence intervals of the means are calculated for the binned intensive AOPs,
415 whose distributions are suitably-approximated as normal. Atmospheric variability for each
416 month, day of week, or hour of day is quantified by the 95% confidence intervals of the mean
417 value, which are represented as error bars on the plots. Differences in the mean AOPs are
418 termed ‘significant’ in this paper if they are larger than *both* (1) atmospheric variability
419 (e.g., if the error bars do not overlap); and (2) twice the precision measurement uncertainty
420 (Table 3). We define the magnitude of temporal variability on each of the timescales as
421 the amplitude of the cycle of mean values (difference between maximum and minimum
422 values). Cycle amplitudes are also expressed as percentages by dividing this difference by
423 the midpoint between maximum and minimum values.

424 Aerosol optical properties at the four sites vary primarily on seasonal timescales. Day
425 of week variability in AOPs can be used as a tool for distinguishing anthropogenic
426 from natural aerosol sources, since natural sources would not be expected to have
427 AOPs that vary on weekly scales (Murphy et al., 2008). Diurnal variability is used along

428 with co-located meteorological data to infer the influence of local pollution sources and
429 mixing layer height on measured AOPs. Due to the dependence of most AOPs on
430 season, their weekly and diurnal cycles are reported for both full years and individual
431 seasons.

432 **2.5.2 Meteorological analysis**

433 Data from co-located surface meteorological stations at the four sites are used to develop
434 proxies to help explain some features of the AOP cycles at each station. Pollution-rose
435 diagrams showing the dependence of σ_{sp} , σ_{ap} , and some calculated AOPs on wind direction
436 are shown for individual seasons to examine the influences of wind sectors and known
437 regional pollution sources on measured AOPs (Fig(s). 5-8 and S16-S22). We compare the
438 temperature-dependence of σ_{sp} (Fig(s). S5 and S7) with reported temperature dependence of
439 biogenic secondary organic aerosol (SOA) (Leaith et al., 2011; Goldstein et al., 2009) and
440 ammonium nitrate partitioning (Parworth et al., 2015; Rupakheti et al., 2005). We also use
441 temperature-dependence of σ_{sp} along with monthly-median temperatures at the sites (Fig.
442 S23) and monthly-averaged σ_{sp} (Fig. 2a) to hypothesize the role of photochemistry on the
443 seasonality of σ_{sp} . Mixing layer height climatologies have been reported for locations at
444 or within ~170 km of the sites. We use the seasonal dependence of the reported mixing layer
445 heights to assess the effect of convection (or lack thereof) on the annual and diurnal cycles
446 of measured near-surface σ_{sp} and σ_{ap} at the four sites.

447 **2.5.3 Significance and trend analysis**

448 Mean values of AOPs over the entire 2010-2013 period are calculated for each site
449 and the differences in mean AOPs among the sites are used as a measure of regional
450 variability (Sect. 4.2). Seasonal differences of most AOPs at individual sites are often
451 much larger than the regional differences of annual-mean AOPs so the seasonality of
452 regional AOP differences must also be taken into account. The differences in mean AOPs
453 among the sites are termed ‘significant’ if they satisfy the same two criteria stated in Sect.
454 2.5.1 for temporal differences. Of the four sites, only BND and SGP have long enough
455 time series (> 10 years) to evaluate trends in AOPs (Sect. 4.3). Slopes and significance
456 are obtained using the function ‘TheilSen’ in the R package ‘openair’ (Carslaw et al.,
457 2012; Carslaw, 2015). Data are de-seasonalized and autocorrelation is accounted for using

458 options supplied with the TheilSen function. Decadal slopes (%/10-year) are calculated
459 by multiplying the yearly slope by 10. Trends are not reported for SGP AOPs requiring
460 absorption due to PSAP data quality issues over most of the 1997-2009 period. Absorption
461 Ångström exponent trends are not calculated for BND because the available time series is
462 less than 10 years.

463 **2.5.4 Systematic relationships**

464 Systematic relationships among intensive AOPs and aerosol loading are explored on an
465 annual basis at the four North American sites for the 2010-2013 (Sect. 4.4). Relationships
466 involving α_{ap} vary with season at some sites so these relationships are also presented for
467 individual seasons. D&O2002 suggested systematic relationships would be useful for
468 constraining model parameterization of AOPs and for reducing uncertainties in satellite-
469 based retrievals of AOD, which make assumptions regarding aerosol size distributions and
470 ω_0 (e.g., Levy et al., 2010). Systematic relationships can also provide information regarding
471 aerosol source types and processes. Relationships between mean intensive AOPs and aerosol
472 loading, represented by σ_{sp} at 550 nm, are investigated for each season at each site by
473 separating hourly-averaged σ_{sp} values into bins of 10 Mm^{-1} width and then calculating the
474 mean AOPs for each σ_{sp} bin. The x-values for the data points on each plot correspond to
475 the bin center. Only bins with a number of data points exceeding 0.1% of all data points
476 are plotted. The relatively high ω_0 values at all sites justifies the use of σ_{sp} , rather than σ_{ep} ,
477 as a proxy for loading. Relationships among a few select intensive AOPs are also included
478 to provide more insight into aerosol sources and/or processes influencing the properties
479 measured at the sites.

480 **3 Site descriptions**

481 All four sites in this study are mid-latitude ($35\text{-}45^\circ\text{N}$) locations in North America with
482 elevations ranging from 230 to 1080 m above sea level (asl), placing them firmly in the
483 boundary layer. These sites can be categorized as anthropogenically-perturbed, rural
484 continental locations. Published aerosol chemistry at the sites (Link et al., 2015; Buzcu-
485 Guven et al., 2007; Rupakheti, et al., 2005; Parworth et al., 2015) indicates that the sites are
486 regionally- influenced.

487 **3.1 Appalachian State University, Boone, North Carolina, USA (APP)**

488 The APP site is situated at the highest point on the Appalachian State University campus
489 (1080 m), located in the southern Appalachian mountain town of Boone, NC (pop.
490 ~20,000). In situ aerosol measurements were initiated at APP in June 2009. APP is also
491 home to a Cimel sunphotometer as part of AERONET, a micro-pulse lidar, an aerosol
492 mass spectrometer, a solar pyranometer as part of the NASA SolRad-Net, and a suite of
493 meteorological and trace gas measurements. The region surrounding Boone is heavily forested
494 in all directions. The APP site is not located near any major highways or major industry
495 but is located 1-3 km from local commuter traffic sources during weekday mornings and
496 late afternoons. The APP site is located 40-60 km from the following towns: (1)
497 Lenoir/Hickory (population ~ 60,000) to the SE; and (2) Wilkesboro (population 3,500) to
498 the east. The Charlotte metropolitan area (population 2.5 million) is located approximately
499 160 km SE of APP and the Piedmont Triangle metropolitan area (population 1.6 million) is
500 located 200-230 km ESE of APP. However, winds are from the SE only ~5% of the time
501 for all seasons (Fig. 5) so the influence of these towns/cities on the APP site is generally
502 small.

503 Summer AOD in the warm, heavily-forested SE US is influenced by highly temperature-
504 dependent isoprene-derived SOA (Goldstein et al., 2009). The Appalachian mountain region
505 is also home to some of the highest rural ammonium sulfate concentrations in the US,
506 with maximum concentrations in summer and minimum concentrations in fall/winter (Hand
507 et al., 2012b). Link et al. (2015) reported in the Supplement to their paper that non-refractory
508 PM₁ aerosol mass at APP during summers (winter) of 2012-2013 was ~66% (49%) organic
509 aerosol, 24% (31%) sulfate, 7% (10%) ammonium, and 3% (10%) nitrate.
510 Approximately 77% of the summer organic aerosol (OA) mass was comprised of low-
511 volatility oxygenated SOA (LV-OOA) and isoprene-derived SOA while the winter OA
512 was comprised of LV- OOA and biomass-burning OA (Link et al., 2015). Wood-burning
513 stoves serve as the primary heating source for 6.2% of occupied housing units in Watauga
514 County (US Census Bureau, 2010) and likely a larger percentage of housing units in the
515 surrounding rural mountain communities. The highly- oxidized, “aged” LV-OOA factor
516 present in nearly equal concentrations during both summer and winter at APP suggests
517 that it is representative of regional background SOA (Link et al., 2015).

518 Weather patterns affecting the southern Appalachian mountain region are highly diverse
519 due to a variety of factors, including complex topography, mid-latitude location, and
520 proximity to the Gulf of Mexico and Atlantic Ocean. Common weather regimes include
521 winter storms, convective cells, dying tropical cyclones, and stagnant summertime episodes.
522 Wind directions are predominately from the west for all seasons (Fig. 5). Wind speeds are
523 highest in November-March and lowest in May- September. The annual temperature cycle
524 in Boone, NC is relatively small, with average daily high temperatures of $\sim 24\text{-}26$ °C in
525 June-Aug and ~ 5 °C in January. The annual cycle in average monthly precipitation is also
526 small, with a maximum in summer (12-13 cm) and minimum in October (~ 9 cm). Relative
527 humidity (RH) is highest during the summer at APP. Planetary boundary layer (PBL)
528 heights calculated from vertical aerosol backscatter profiles measured with a micro-pulse
529 lidar at APP from 2/2013-8/2014 reveal a relatively weak diurnal and seasonal dependence
530 of PBL heights. Median afternoon (morning) PBL heights are 920 m (820 m) in winter, 1200
531 m (880 m) in spring, 1100 m (850 m) in summer, and 1050 m (680 m) in fall (unpublished
532 result).

533 **3.2 Bondville, Illinois, USA (BND)**

534 The BND aerosol monitoring station is located on farmland at the Bondville
535 Environmental and Atmospheric Research Site (BEARS) in rural east-central Illinois. In situ
536 aerosol measurements at BND began in 1994. Additional measurements made at BND
537 include a Cimel sunphotometer as part of AERONET, a comprehensive set of
538 meteorological measurements, an IMPROVE aerosol chemistry system, and a full suite
539 of solar radiation measurements made by NOAA/ESRL. The BND station is situated
540 approximately 6.5 km south of Bondville (population 450), 16 km southwest of
541 Champaign–Urbana (population $\sim 230,000$), and is surrounded in all directions by corn,
542 soybean and hay fields. A regional airport (Willard Airport) is situated approximately
543 10 km east of the BND site. The town of Decatur (population $\sim 75,000$) lies ~ 50 km to
544 the SW and three large metropolitan areas are within 250 km of the site: (1) Chicago
545 (population 9.6 million), located ~ 240 km to the NNE; (2) Indianapolis, IN (population
546 1.8 million), located ~ 210 km to the east; and (3) St. Louis, MO (population ~ 3.7 million) is
547 located ~ 230 km to the SW. The area is crisscrossed by a network of interstate
548 highways, including I-57 (~ 7 km to the east), I-72 (~ 10 km north), I-74 (~ 15 km

549 northeast), and I-70 (~100 km south).

550 Buzcu-Guven et al. (2007) applied positive matrix factorization techniques to apportion
551 the PM_{2.5} aerosol mass at BND into the following annually-averaged factors: (1)
552 secondary sulfate (27%); (2) secondary nitrate (24%); (3) mobile/SOA factor (17%), largely
553 due to gasoline and diesel vehicle emissions; (4) biomass-burning OA (12%); (5) soil
554 (6%); (6) copper smelter (2%); (7) chromium and nickel from metal plating (5%); and (8)
555 mixed industrial (7%). The largest contributors to organic matter (OM) were biomass
556 burning (38% of OM) and mobile/SOA (24% of OM) factors, followed by factors
557 associated with industrial sources (< 20% of OM). Buzcu-Guven et al. (2007) could not
558 resolve the mobile source aerosol factor into the two fuel combustion types (gasoline vehicle
559 and diesel) because the BND site is affected by transported urban emissions rather than local
560 emissions. They reported strong seasonality in secondary sulfate (maxima in summer) and
561 nitrate (maxima in winter) at BND. Similar regional sulfate and nitrate seasonality was
562 reported for the region by Hand et al. (2012b) and by Spak and Holloway (2009). The
563 highest sulfate concentrations at BND were associated with transport from the Ohio River
564 Valley, Western Ohio, and Southern Illinois, where large numbers of coal-fired power
565 plants are located (Buzcu-Guven et al., 2007). Winter ammonium nitrate concentrations
566 in the Midwest US are among the highest in the country, due to significant sources of
567 agricultural ammonia and combustion-generated NO_x emissions, in addition to
568 meteorological conditions (low temperature and high humidity) favorable for gas-to-
569 particle partitioning (Hand et al., 2012b; Spak and Holloway, 2009).

570 Polluted air at BND is generally associated with southerly wind sectors (120°-240° wind
571 directions) and cleaner air is typically associated with NW wind sectors (Fig. 6). Winds
572 reaching BND from the SW also pass over regions with high summer biogenic isoprene
573 emissions (Fig. 3 of Parworth et al., 2015). Wind speeds are higher in November-May and
574 lower in June-September (not shown). Higher wind speeds are more common for S/SW
575 wind sectors for all seasons except winter, when higher wind speeds are more common for
576 NW wind sectors. Lowest wind speeds are associated with easterly wind sectors. Average
577 high temperatures are highest in July (29.5 °C) and lowest in January (0.5 °C). Average
578 monthly precipitation is highest in May-July (~12 cm) and lowest in Jan-Feb (~5 cm).
579 Holzworth (1964) used daily soundings at Joliet, IL (located ~130 km NNE of BND) to

580 calculate monthly mean maximum mixing layer heights: DJF (480, 480, 480 m); MAM
581 (980, 950, 1040 m); JJA (1090, 1380, 1310 m); SON (860, 790, 600 m). Climatologies of
582 surface aerosol optical properties observed at BND have been reported by Koloutsou-
583 Vakakis et al. (2001) and D&O2002. Sheridan et al. (2012) also reported BND surface
584 aerosol properties for comparison with airborne aerosol measurements.

585 **3.3 Egbert, Ontario, Canada (EGB)**

586 The EGB station at the Centre for Atmospheric Research Experiments (CARE), is situated
587 near the town of Egbert, in Ontario, Canada. In situ aerosol optical measurements at EGB
588 began in 2009. The CARE facility is also home to complementary measurements of
589 greenhouse gases such as CO₂ and CH₄, as well as meteorological instrumentation and
590 measurements of aerosol chemistry and aerosol size distributions. Egbert is a rural location
591 consisting of mixed deciduous/coniferous forest and agricultural land. The population of
592 Egbert and surrounding communities is approximately 20,000. Egbert is located 70 km
593 N/NE of Toronto, Ontario and the heavily-populated southern Ontario region, with a
594 population of approximately 8 million. A major highway (HWY 400) is located
595 approximately 8 km to the east of the EGB site. The highway experiences commuter
596 traffic during early morning and late afternoon. The town of Barrie (population ~128,000)
597 is located ~25 km NNE of the EGB site but the wind comes from this direction only ~2-3% of
598 the time for all seasons and the associated air masses are relatively clean (Fig. 7). Forest
599 density is highest to the north of EGB.

600 Southerly winds (120°-240° wind directions) typically bring more polluted air masses
601 (Fig. 7) associated with outflow from the heavily populated Toronto area, southern
602 Ontario, and eastern US (Yang et al., 2011; Liggió et al., 2010). Southerly air masses
603 contain higher levels of elemental carbon (EC), sulfates, nitrates, and OM and higher
604 EC/OC ratios than cleaner air masses from the north (Chan et al., 2010; Rupakheti et al.,
605 2005; Yang et al., 2011). Organic carbon (OC) and EC are highly-correlated (poorly-
606 correlated) during cold (warm) months, implicating primary aerosol sources during cold
607 months and a large influence of transported warm-season SOA from urban areas south of
608 EGB (Yang et al., 2011). Northerly winds (300°-60° wind directions) typically bring air
609 masses from sparsely-populated, heavily-forested regions (Slowik et al., 2010), with high
610 concentrations of temperature-dependent biogenic SOA during summer months (Leaitch et

611 al., 2011; Slowik et al., 2010). Long-distance transport of smoke from the northwest is also
612 observed during the summer forest fire season in northwest Canada. Wind speeds at EGB
613 are higher in November-April and lowest in July-August. Average daily maximum
614 temperatures are highest in July (26 °C) and lowest in January (-3 °C). Holzworth (1964)
615 used daily soundings at Buffalo, NY (located ~170 km SE of EGB) to calculate monthly
616 mean maximum mixing layer heights: DJF (510, 480, 530 m); MAM (780, 600 810, 1070
617 m); JJA (1180, 1440, 1360 m); SON (1190, 530, 700 m).

618 **3.4 Lamont, Oklahoma, USA (SGP)**

619 The DOE Southern Great Plains (SGP) Cloud, Aerosol and Radiation Testbed (CART)
620 Central Facility site is located in north central Oklahoma near the town of Lamont (pop.
621 417) in a rural, agricultural region surrounded mostly by wheat, corn and hay fields.
622 Measurements of in situ aerosol optical properties began in 1996. The site is also equipped
623 with a Cimel sunphotometer (as part of AERONET), cloud radars, lidars, meteorological
624 instruments and many remote-sensing radiometers, making it the largest climate research
625 facility in the world. The SGP site is situated 100-150 km from the following
626 metropolitan areas: (1) Wichita, KS (population ~638,000), located 112 km to the north;
627 (2) Oklahoma City (population 1.3 million), located 136 km to the south; and (3) Tulsa, OK
628 (population ~400,000), located ~150 km to the southeast. The SGP site experiences
629 infrequent local traffic but is situated approximately 15 km to the west of an interstate
630 highway (I-35). There are no major aerosol sources within several hundred km to the
631 northwest, west or southwest of the site.

632 Parworth et al. (2015) reported an average total non-refractory PM₁ aerosol mass
633 concentration at SGP (from November 2010-June 2012) of 7.0 µg m⁻³. Their reported total
634 aerosol mass concentration was broken down into (1) OA (57%); (2) nitrate (21%); (3)
635 sulfate (12%); (4) ammonium (9.4%); and (5) chloride (0.24%). Organic aerosol constituted
636 a larger and nearly constant mass fraction (~70%) from April-October. Sulfate mass
637 fraction also exhibited little seasonality. Both OA and sulfate mass concentrations
638 demonstrated fall minima, with mass concentrations ~2-3 times lower than during
639 summer. Approximately 90% of the OA was highly-oxidized aged aerosol, with biomass-
640 burning OA comprising the remaining ~10%. The aged, oxidized OA peaked in June-July.
641 Biomass-burning OA was highest in late winter and spring and was likely due to local

642 agricultural burning in preparation for crop season. (Parworth et al., 2015). Ammonium
643 nitrate was the largest PM₁ aerosol component in winter, followed by OA. Rural EC
644 concentrations in northern Oklahoma are low and peak in autumn (Fig. 3 of Hand et al.,
645 2013). The super-micron aerosol was primarily soil dust, which exhibits a summer maxima in
646 the region (Hand et al., 2012b).

647 The typical annual weather cycle at SGP involves a cold, shallow inversion layer in the
648 winter with relatively stagnant winds and a hot, humid summer with strong convection,
649 high daytime boundary layer, and southerly winds. Prevailing winds at the SGP site are
650 from the S/SE for all seasons except winter (Fig. 8). Average high temperatures are highest
651 in July-August (33-34 °C) and lowest in January (0.7 °C). Average monthly precipitation is
652 highest in May-June (~11-12 cm) and lowest in Jan-Feb (~3.0-3.5 cm). Median mixing
653 layer heights are less than 100 m (above ground level) from 2030 central standard time
654 (CST) through 0530 CST for all seasons and median afternoon mixing layer heights are
655 752 m in winter, 1260 m in spring, 1640 m in summer, and 1390 m in fall (DelleMonache et al.,
656 2004). The SW US and southern Great Plains experienced exceptionally hot and dry
657 conditions during 2010-2012, coinciding with La Niña years. Extensive fires raged across
658 the SW US during 2011-2012, particularly Texas, Arizona, Colorado, New Mexico and
659 Oklahoma. The hot, dry conditions during 2010-2012 also created conditions favorable for
660 airborne dust production and transport. Climatologies of surface and aerosol optical
661 properties observed at SGP have been reported by Sheridan et al. (2001) and D&O (2002).

662 **4 Results and Discussion**

663 Several broad features of AOP temporal variability are common to all or most of the four
664 sites. For brevity, these features are first discussed collectively before moving on to a more
665 detailed analysis of AOP variability at each site and then to comparisons among the sites.
666 Much of the seasonal AOP variability at each site can be explained using (1) published
667 results of seasonally-dependent aerosol chemistry at the sites; (2) pollution-rose diagrams,
668 which simultaneously display percentage of hours with winds arriving from each wind
669 sector and the distribution of AOP values for each sector; (3) known regional pollution
670 sources; and (4) published seasonality of PBL height and monthly-median temperature and
671 relative humidity at the sites. Temperature dependence of σ_{sp} is also helpful. Diurnal and
672 weekly cycles of select AOPs and the seasonal dependence of these cycles are used to

673 estimate the relative influences of some local and regional sources (mainly traffic) and
674 PBL heights. Regional variability in AOPs is discussed in the context of the annual AOP
675 cycles and the above-listed sources of seasonal variability at each site. Trends in AOPs at
676 BND and SGP are used to place results for the current period in a long-term context.
677 Systematic relationships among select AOPs at each site are used to help interpret the
678 temporal and regional AOP variability and to hypothesize aerosol sources or processes
679 at the sites. Numerous pieces of supporting materials for the presented results are
680 included as part of the Supplemental Materials to this paper. We reference those figures
681 and tables with the letter 'S' (ex: Fig. S13, Table S2) to distinguish them from figures
682 appearing in this paper.

683 **4.1 Temporal variability of aerosol optical properties**

684 **4.1.1 Temporal variability common to all sites**

685 The annual AOP cycle amplitudes are larger than the weekly and diurnal AOP cycle
686 amplitudes at all sites. Nearly all annual AOP cycles are significant, with cycle amplitudes
687 larger than the 95% confidence intervals of both the monthly-mean AOPs (Fig. 2) and the
688 measurement uncertainties (Table 3). July and/or August σ_{sp} maxima are observed at all sites
689 (Fig. 2a), with steeper σ_{sp} decreases from summer to fall than from summer to spring.
690 Summer-to-spring and summer-to-fall σ_{sp} decreases at EGB and APP are approximately
691 twice the magnitude of those observed at BND and SGP. Scattering coefficient reaches a
692 minima during October at all sites except APP, where it is lowest in December. Absorption
693 coefficient is highest in summer and lowest in winter at all sites (Fig. 2b), although the
694 differences between summer σ_{ap} maxima and the surrounding months are only significant at
695 BND and EGB. Summer-to-autumn σ_{sp} decreases are larger than those of σ_{ap} , leading to
696 minimum ω_0 in October at all sites (Fig. 2e). Hemispheric backscatter fraction is highest
697 in October at all sites (Fig. 2d). The confluence of early-autumn decreases in σ_{sp} and ω_0
698 and increases in b is indicative of less production and/or more efficient removal of large,
699 highly-scattering particles during early autumn, relative to summer. This effect is most
700 noticeable at EGB and APP (Fig. 2) and also is seen in the summer-spring differences at APP.
701 October ω_0 minima contribute to DRFE maxima (least negative) at EGB and BND but no
702 significant autumn DRFE changes are seen at APP and SGP (Fig. 2f). Photochemistry

703 likely influences the summer σ_{sp} maxima and σ_{sp} that are larger in spring than in fall at
704 all sites. The temperature-dependence of σ_{sp} (Fig. S5) and differences in monthly-median
705 temperatures (Fig. S23) combine to yield predicted differences in σ_{sp} that are of similar
706 magnitude to the large observed summer-spring (July-April) σ_{sp} differences at EGB and
707 APP and to the observed summer-autumn (July-October) σ_{sp} differences at EGB, BND, and
708 SGP (Fig. 2a). The summer-autumn σ_{sp} difference based on temperature considerations is less
709 at APP than the observed σ_{sp} difference, leading us to hypothesize an additional contributor
710 to the autumn σ_{sp} decrease. Cloud and fog scavenging of large, highly-reflecting particles
711 would be consistent with cooler September temperatures (Fig. 23a), higher RH (Fig. S23b),
712 and cloud cover in September at APP. The inverse relationship between σ_{sp} and b seen in the
713 annual cycles at all sites (Fig(s). 2a and 2d) is indicative of the influence of particle
714 growth (and possibly cloud or fog scavenging) on σ_{sp} . Wet deposition likely impacts σ_{sp}
715 most in summer and least in spring and fall, given the seasonality of precipitation at the
716 sites. Secondary σ_{sp} maxima are observed during winter at all sites except APP (Fig. 2a).
717 When combined with winter σ_{ap} minima, the result is a winter ω_0 maxima at these sites
718 (Fig. 2e).

719 In contrast to b , the annual R_{sp} and PM10 α_{sp} cycles (Fig(s). 2c and 2g) at APP, BND, and
720 SGP (the sites where these AOPs are calculated) do not demonstrate an obvious relationship
721 with the annual σ_{sp} cycles. Collaud Coen et al. (2007) conducted simulations based on Mie
722 theory to show that b at 550 nm is most sensitive to particle size changes for diameters
723 ~100-300 nm (their Fig. 7 and accompanying discussion). Schuster et al. (2006) combined
724 simulations based on Mie theory with volume size distributions and AOD from
725 AERONET to show that extinction Ångström exponent is relatively insensitive to fine
726 mode effective radius for bi-modal aerosol size distributions and that extinction Ångström
727 exponent may serve as a better indicator of fine-mode aerosol volume fraction than mean
728 particle size. The stronger relationship between the annual b and σ_{sp} cycles (relative to
729 relationships between the cycles of σ_{sp} with either α_{sp} or R_{sp}) suggests that the major seasonal
730 changes in the aerosol size distributions at APP, BND, and SGP may lie at the smaller
731 end of the range of optically-relevant accumulation mode particles (100-300 nm), with
732 shifts toward larger particles in summer and smaller particles in fall. Photochemistry likely
733 plays a role in the observed seasonal cycle of b , especially at APP and EGB. Gas-to-particle

734 conversion onto existing particles is most efficient for the 100-500 nm diameter range, since
735 this is where most of the aerosol surface area typically lies (Seinfeld and Pandis, 1998).
736 Reduced gas to particle conversion in fall (when photochemistry and precursor levels are
737 lower) would impact α_{sp} and R_{sp} .

738 Absorption Ångström exponent is lowest during summer months and highest during
739 winter months (Fig. 2h) at APP, BND and SGP (the three sites where α_{ap} can be calculated).
740 The summer-to-winter difference in α_{ap} is clearly larger at APP (~0.9) than at BND and
741 SGP (~0.5). Absorption Ångström exponent values near and below 1 during May-
742 September suggest that black carbon (BC) contributes most to σ_{ap} during these months
743 (Gyawali et al., 2009; Cazorla et al., 2013). Gyawali et al. (2009) performed simulations
744 using Mie theory to show that α_{ap} values much less than 1 are possible (their Fig(s). 8
745 and 9) when absorbing particles are coated with non-absorbing substances. Clarke et al.
746 (2007) also reported a large number of α_{ap} (470/660 nm) values clustered between 0.7-1.1 for
747 pollution plumes during extensive flights over North America as part the of the
748 INTEX/ICARTT experiment in summer 2004.

749 Weekly and diurnal cycle amplitudes of σ_{sp} (Fig. 3) and nearly all intensive AOPs
750 observed at the four sites are much smaller than the corresponding annual cycle amplitudes.
751 Weekly and diurnal σ_{ap} cycle amplitudes (Fig. 4) are larger than those of σ_{sp} at all sites and
752 are largest in summer. Weekly σ_{ap} cycles at all sites are marginally significant in fall with
753 σ_{ap} cycle amplitudes approximately twice the σ_{ap} measurement precision uncertainty (Table
754 3). All sites demonstrate small and/or insignificant weekly σ_{sp} cycle amplitudes (~20% or
755 less) and a lack of weekly σ_{sp} patterns across seasons (Fig. 3). This suggests that weekly σ_{sp}
756 cycles are driven by regional-scale phenomena, where any weekend effects are smoothed out
757 by mixing. The weekly cycles of intensive AOPs are nearly always minimal at all sites
758 (Fig(s). S9-S15).

759 Similar to the weekly σ_{ap} cycles, the diurnal σ_{ap} cycles are also much larger than diurnal σ_{sp}
760 cycles at all sites. However, the diurnal σ_{ap} variability is only significant during summer
761 and (at all sites except APP) fall. Diurnal cycles of nearly all intensive AOPs are
762 minimal and/or insignificant. Notable exceptions are ω_0 and DRFE during summer and
763 fall. The amplitudes of the diurnal ω_0 cycles are ~0.03-0.04 during summer and fall at all

764 sites (Fig. S12). In most of these cases, ω_0 is lowest during late evening and/or early
765 morning and highest during afternoon. At APP, the ω_0 peak extends from around noon to
766 the early morning hours. Diurnal DRFE cycles (Fig. S13) in turn follow the diurnal ω_0
767 cycles, due to the lack of diurnal variability in b . Summer and fall DRFE is more negative
768 by $\sim 3 \text{ W m}^{-2} \text{ AOD}^{-1}$ during the afternoon than during the surrounding hours (Fig. S13).
769 The lack of diurnal and weekly variability in mean b , R_{sp} , and α_{sp} indicates that particle
770 size distributions at APP, BND, and SGP likely demonstrate little variability on weekly or
771 daily timescales. D&O2002 reported similar or slightly smaller ω_0 and b diurnal cycle
772 amplitudes for BND and SGP but they did not consider the diurnal cycles for individual
773 seasons.

774 **4.1.2 Temporal variability at APP**

775 Aerosol light scattering and absorption coefficients at APP are dominated by PM1 for all
776 seasons and the relative influence of PM1 varies little with season, as seen by R_{sp} values of
777 0.80-0.88 (Fig.2c), α_{sp} values of 1.9-2.2 (Fig. 2g), and R_{ap} values of 0.90-0.95 (Fig. S8c).
778 Both σ_{sp} and σ_{ap} are moderately elevated for NE wind sectors, with 0° - 90° wind
779 directions (Fig. 5). Median σ_{ap} is \sim 20-30% higher for NE wind sectors than for the
780 prevalent westerly wind sectors for all seasons except winter, when σ_{ap} for the NE wind
781 sectors is \sim 2 times higher than σ_{ap} for westerly wind sectors (not shown). Median σ_{sp} is less
782 elevated for the NE wind sectors (typically \sim 10-15%). Wind sector does not strongly
783 influence median or mean values of most intensive AOPs, although low ω_0 (< 0.80) is more
784 frequently associated with NE wind sectors (Fig. S17a). It should be noted that the prevalent
785 westerly wind sectors represent the confluence of 3-4 (seasonally-dependent) different
786 average air mass back-trajectories, which all typically arrive at APP from the west. Link et
787 al. (2015) reported that aerosol and gas phase chemistry measured at APP displayed a
788 generally homogeneous distribution across source regions. One exception was elevated
789 levels of urban, oil and natural gas, combustion tracers, and OA mass concentrations
790 associated with air mass back-trajectories passing over the polluted Ohio River valley and
791 Appalachian mountain region before arriving at APP with $\sim 0^\circ$ - 90° wind directions (Link et
792 al., 2015).

793 PM1 σ_{sp} at APP and its seasonality (Fig. 2a) are largely influenced by regional background

794 SOA and sulfate. Biogenic SOA and sulfate both exhibit summer maxima and winter
795 minima in the SE US (Goldstein et al., 2009; Hidy et al., 2014) and both summer and
796 winter non-refractory PM1 aerosol mass at APP are dominated by SOA and sulfate
797 (Supplementary Materials of Link et al., 2015). Summer σ_{sp} at APP is correlated with
798 both OA and sulfate mass concentrations ($r=0.60$ and $r=0.62$, respectively). The
799 temperature-dependence of PM1 σ_{sp} at APP during April-October (Fig. S7) also agrees
800 well with the expected temperature dependence of biogenic emissions (Guenther et al.,
801 2006) and with the temperature-dependence of AOD over the SE US (Goldstein et al.,
802 2009). The summer σ_{sp} peak coincides with a distinct minima in b (30-40% lower than all
803 other seasons) and maxima in ω_0 (~ 0.07 higher than during winter). Aerosol number
804 concentrations measured at APP are also lower in summer than during spring and fall
805 (unpublished result). The confluence of lower concentrations of larger, highly-reflective
806 PM1 particles during months with high regional temperatures, solar irradiance, and RH is
807 consistent with gas-to-particle conversion onto existing particles.

808 The annual σ_{ap} cycle at APP (Fig. 2b) is out of phase with the annual cycle of EC
809 concentrations reported for rural eastern US IMPROVE sites (Hand et al., 2012b). Hand et al.
810 (2012b) cited sources such as residential heating for the fall and winter EC concentration
811 maxima. Absorption coefficient at APP exhibits a summer maximum and a winter
812 minimum, though the summer σ_{ap} maximum is not significantly different from early fall
813 and spring σ_{ap} (to 95% confidence). Absorption Ångström exponents of ~ 1.3 - 1.4 (Fig.
814 2h) and $\alpha_{sp} > 2$ during colder months (Fig. 2h) suggest a mixture of EC and light-absorbing
815 OC (Fig. 2 of Cazorla et al., 2013). A contribution to σ_{ap} from OC is also consistent
816 with a biomass-burning OA factor in the winter aerosol mass spectra measured at APP
817 (Fig. S2 of Link et al., 2015) and may result from winter residential wood-burning (US
818 Census Bureau, 2010; Zhang et al., 2010). However, the diurnal σ_{ap} cycles (Fig. 4b) suggest
819 an influence from local traffic during all seasons and α_{ap} values of 1 or less for non-winter
820 months suggest that BC is the major contributor to σ_{ap} during these months.

821 APP is the only site to demonstrate consistent weekly σ_{sp} and σ_{ap} cycles across seasons,
822 with the exception of winter. Local commuter traffic likely exerts the largest influence on the
823 diurnal σ_{ap} cycles (Fig. 4b) and possibly the weekly σ_{ap} cycles (Fig. 4a). Diurnal σ_{ap} cycles
824 are only significant at 95% confidence during summer but a similar bi-modal structure is

825 seen for all seasons (Fig. 4b), with morning and late afternoon/early evening commuter
826 peaks. The only sign of weekend local traffic influence is an insignificant Saturday
827 morning peak $\Delta\sigma_{ap} \sim 0.1-0.2 \text{ Mm}^{-1}$ present during most seasons (unpublished result),
828 confirming the primary influence of local commuter traffic. The absence of any influence of
829 diurnal PBL height variation on the diurnal σ_{ap} cycles at APP is consistent with the
830 relatively small afternoon/morning PBL height differences measured at the heavily-forested
831 APP site (unpublished result). PBL height is often poorly defined at APP and may be related
832 to the fact that the APP site is situated on a ridge. The PBL and free troposphere do not
833 fully decouple during the evening. As a result, pronounced late-evening thru early morning
834 σ_{sp} and σ_{ap} maxima that are characteristic of a PBL height influence are not a regular
835 feature of the diurnal cycles at APP (Fig(s). 3b and 4b). Diurnal variability of σ_{sp} and
836 intensive AOPs is insignificant and/or minimal for all seasons (Fig(s). S9-S15), with the
837 exceptions of (1) morning ω_0 decreases (by $\sim 0.02-0.03$) DRFE increases (by $2-3 \text{ W m}^{-2}$
838 AOD^{-1}) during all seasons, coinciding with the commuter traffic; and (2) a small summer
839 daytime decrease (0.6 to 0.4) in α_{ap} , possibly due to coating of absorbing particles
840 (Gyawali et al., 2009) or an artifact associated with filter-based σ_{ap} measurements (Lack et
841 al., 2008; Lack et al., 2009).

842 The spring, summer, and fall weekly σ_{sp} and σ_{ap} cycles at APP (Fig(s). 3a and 4a) are
843 characterized by early week increases leading to broad Wednesday-Friday maxima. Both
844 σ_{sp} and σ_{ap} begin to increase near the time of the Monday morning traffic peak
845 (unpublished result) and decrease over the weekend, coinciding with less weekend traffic.
846 The weekly σ_{sp} and σ_{ap} cycles are likely the result of a build-up of scattering and absorbing
847 aerosols in the PBL during the first half of the week. Sunday σ_{ap} minima and weekly cycle
848 amplitudes of $\sim 25-35\%$ during spring and fall are consistent with the timing and amplitudes
849 of weekly EC concentration cycles reported for the rural US (Murphy et al., 2008) and
850 with weekday-weekend EC concentration differences in the urban US (Bae et al., 2004;
851 Blanchard et al., 2008). Smaller but significant weekly σ_{sp} cycle amplitudes of $\sim 15-20\%$
852 during spring, summer, and fall are larger than weekly cycles in OC and sulfate reported
853 by Murphy et al. (2008). Absorption coefficient exhibits a larger summer weekly cycle
854 amplitude of $\sim 50\%$ (Fig. 4a) than σ_{sp} (Fig. 3a). Local traffic is less during summer but

855 construction activity and road repairs on the Appalachian State University campus and in
856 town are higher so a larger influence from diesel emissions could be a source for the larger
857 σ_{ap} cycle during summer. Local traffic influences on the weekly and diurnal σ_{ap} cycles
858 during winter may be masked by other sources of EC, such as wood-burning. Small
859 weekly cycles in several intensive AOPs are consistent with the above-discussed local
860 traffic influence. Single-scattering albedo decreases by ~ 0.02 from Sun-Wed during
861 fall/winter (Fig. S12) with smaller decreases during spring/summer. DRFE increases by ~ 2
862 $W m^{-2} AOD^{-1}$ from Sun-Wed during fall/winter, with smaller insignificant increases in
863 spring/summer (Fig. S13). Absorption Ångström exponent increases during the week by
864 ~ 0.2 (0.4 to 0.6) during summer, with smaller, insignificant increases (~ 0.1) during fall and
865 winter (Fig. S15).

866 **4.1.3 Temporal variability at BND**

867 PM1 particles contribute $\sim 76\%$ (72%) to the summer (winter) PM10 σ_{sp} and 88%
868 ($\sim 80\%$) to the summer (winter) PM10 σ_{ap} at BND (Fig(s). 2c and S8c). The annual PM1
869 and PM10 σ_{ap} and σ_{sp} cycles are similar for all seasons (Fig(s). 2 and S8) so the PM1 AOP
870 cycles at BND are representative of the PM10 aerosol. Many of the same general features of
871 the σ_{sp} annual cycle at BND (Fig. 2a) have been reported by others (D&O2002; Koloutsou-
872 Vakakis et al., 2001), including the July-August σ_{sp} maximum and early-autumn σ_{sp}
873 minimum. D&O2002 reported similar summer-autumn and summer-spring σ_{sp} differences,
874 with median σ_{sp} values in July approximately two times larger than σ_{sp} in October-
875 November and ~ 1.5 times larger than σ_{sp} in April-May. The σ_{ap} annual cycle reported by
876 D&O2002 was also very similar to that shown in Fig. 2b, except for an October σ_{ap} maxima
877 in their study. Planetary boundary layer heights reported for nearby Joliet, IL by
878 Holzworth (1964) were approximately three times higher in summer than in winter,
879 suggesting that summer aerosol production must be much higher (and/or sinks be much
880 lower) to maintain the observed higher summer aerosol loading in the mixed layer.

881 Regional aerosol transport associated with southerly wind sectors (SE to SW wind
882 directions) exerts a large influence on σ_{sp} during all seasons (Fig. 6a). Northerly wind sectors
883 (NW to NE wind directions) exert a comparable or larger influence on σ_{sp} during winter
884 months. Much of the light-scattering aerosol arriving from the south is likely secondary

885 sulfate associated with the high-density of coal-burning power plants in southern Illinois
886 and the Ohio River Valley region (Buzcu-Guven et al., 2007). Summer σ_{sp} may also be
887 influenced by biogenic SOA. Median summer temperatures are ~ 3 °C higher for SW winds
888 at BND than for SE winds and the forests over SW Illinois and SE Missouri emit high
889 amounts of isoprene during summer (Fig. 3 of Parworth et al., 2015). Scattering
890 coefficient for SW wind directions exhibits a sharp July peak and the temperature-
891 dependence of σ_{sp} at BND during April-October demonstrates modest agreement ($r=0.47$, as
892 shown in Fig. S7) with the exponential temperature-dependence of biogenic volatile
893 organic compound emissions (Guenther et al., 2006). The secondary PM1 σ_{sp} peak during
894 winter months at BND (Fig. 2a) may be influenced by temperature dependent gas-to-
895 particle partitioning of regional ammonia and nitric acid into ammonium nitrate.
896 Rupakheti et al (2005) reported that gas-phase ammonia correlated positively with
897 particulate ammonium and nitrate mass concentrations for temperatures below 12 °C and
898 that more ammonia remained in the gas phase for $T > 12$ °C. The temperature dependence of
899 median PM1 σ_{sp} at BND changes sign (positive to negative) for temperatures less than
900 ~ 10 °C, nearly doubling as temperature decreases from ~ 10 °C to ~ -5 °C (Fig. S5). The σ_{sp}
901 increase is accompanied by an increase in median ω_0 from 0.89 to 0.96 (Fig. S6); and a
902 decrease in median b from 0.15 to 0.13. Addition of large, highly-scattering PM1 particles
903 at low temperatures is consistent with high winter ammonium nitrate concentrations
904 reported for BND (Buzcu-Guven et al., 2007). Much of the winter σ_{sp} increase is likely
905 due to regional transport from the north. Winter σ_{sp} exhibits the largest increase for
906 northerly wind sectors (Fig. 6a) with winter σ_{sp} a factor of ~ 1.5 -3 larger than spring and
907 fall σ_{sp} . Winter ω_0 and b are highest for the northerly wind directions, with $\omega_0 \geq 0.93$
908 and $b < 0.15$ for a majority of the arriving air masses (Fig. S19). Northerly wind sectors are
909 typically associated with colder air mass traveling over regions with high concentrations of
910 ammonium and nitrate precursor gases (Hand et al., 2012b). Temperature-dependent
911 ammonium nitrate production is also consistent with the highly variable timing and
912 magnitude of the winter σ_{sp} peak for individual years (Fig. S2). Lower winter PBL heights
913 during winter (Holzworth, 1964) likely also contribute to elevated winter σ_{sp} . Variability
914 in winter PBL heights could conceivably contribute to winter σ_{sp} variability.

915 Diurnal σ_{sp} cycles are insignificant for all seasons except for a marginally significant fall

916 amplitude of ~25% (Fig. 3d). Diurnal σ_{ap} cycle amplitudes (Fig. 4d) are much larger than
917 those of σ_{sp} during all seasons except winter. Differences between σ_{ap} and σ_{sp} diurnal cycle
918 amplitudes are largest in summer (~60% versus 10%) and are also non-negligible in fall
919 (~50% versus ~25%) and spring (~40% versus ~20%). Diurnal σ_{ap} and σ_{sp} cycles are both
920 smallest during winter, with cycle amplitudes of ~10%. The influence of diurnal PBL
921 height cycle is clearly seen in the diurnal σ_{ap} cycles (Fig. 4d) and a smaller PBL height
922 influence is seen in the σ_{sp} cycles. The differences between σ_{ap} and σ_{sp} cycle amplitudes
923 during summer and (to a lesser degree) fall and spring suggests a large additional source of
924 scattering aerosols during summer daytime hours. Photochemical aerosol processing is the
925 only source of scattering particles whose diurnal and seasonal dependence can explain
926 the seasonality of differences between the σ_{ap} and σ_{sp} cycle amplitudes. It is also consistent
927 with the seasonality of sulfate mass concentrations reported for BND (Buzcu-Guven et al.,
928 2007). Weekly σ_{sp} cycles are statistically significant for all seasons but the cycle
929 amplitudes are less than 15% for all seasons except fall. Our weekly σ_{sp} cycle amplitude for
930 the entire year (Fig. 3c) is similar to that of Murphy et al. (2008).

931 Regional pollution transport associated with southerly wind sectors also influences the
932 annual σ_{ap} cycle at BND over all seasons (Fig. 6b). Highest σ_{ap} for the southerly wind
933 sectors occurs during summer and fall and southerly winds are most common in summer
934 (Fig. 6a), leading to the summer σ_{ap} maxima (Fig. 2b). Lowest σ_{ap} for the southerly wind
935 sectors occurs during winter and air masses from the less anthropogenically-perturbed
936 W/NW reach the site most frequently in winter (Fig. 6b), leading to the winter σ_{ap} minima.
937 The difference between the month of maximum σ_{ap} (August) and that reported by
938 D&O2002 (October) could be due to differences in the seasonality of wind directions between
939 the two periods. It could also arise due to differences in the seasonality of removal
940 mechanisms such as precipitation between the periods but this would have likely also
941 shifted the month of maximum σ_{sp} .

942 The weekly and diurnal σ_{ap} cycles during summer and autumn (Fig(s). 4c-d) are
943 consistent with a large influence from regional diesel emissions during these seasons and
944 possibly during other seasons, although the weekly and diurnal σ_{ap} cycles are only
945 significant in summer and autumn. Maximum σ_{ap} extends from sunset to sunrise for all

946 seasons (Fig. 4d), with a broad minimum extending from just after sunrise to just before
947 sunset. Large seasonality of PBL heights is obvious in the diurnal σ_{ap} cycles (Fig. 4d),
948 consistent with large (factor of 3) summer-to-winter PBL height differences reported for the
949 region by Holzworth (1964). The absence of early morning and late afternoon local
950 commuter peaks at BND is not surprising, since emissions from interstate highway traffic
951 and agricultural activity represent the largest local sources of absorbing aerosols. Long-
952 distance trucking comprises a large portion of interstate highway traffic in the region and both
953 this and farming activities typically persist throughout the day. The diurnal σ_{ap} cycles for
954 individual days of the week show the same broad features as the corresponding weekly-
955 integrated diurnal σ_{ap} cycles (Fig. 4d) for all seasons, with the exception of differences
956 between post-dusk and pre-dawn σ_{ap} for individual days of the week (unpublished result).
957 During summer, post-dusk σ_{ap} is slightly larger than pre-dawn σ_{ap} for each day during
958 Monday-Friday, leading to a gradual build-up of absorbing aerosols in the PBL. Post-dusk σ_{ap}
959 is less than pre-dawn σ_{ap} on Saturday and Sunday. The resulting weekly σ_{ap} cycle (Fig. 4c)
960 and the σ_{ap} cycles for individual days suggest a nearly-constant source of absorbing
961 aerosols from sunrise to sunset, with largest emissions from Monday-Friday. Both interstate
962 truck traffic and farming activities are consistent with the observed diurnal and weekly
963 patterns during summer but truck traffic is likely the source more capable of contributing to
964 the large summer diurnal and weekly σ_{ap} cycle amplitudes (60% and 40%, respectively),
965 given the higher summer PBL heights in the region. The fall weekly σ_{ap} cycle (Fig. 4c) also
966 exhibits a build-up of absorbing aerosols from Monday-Tuesday, followed by lower
967 aerosol loading during the remainder of the week. This cycle is not consistent with known
968 weekly cycles in truck traffic or agricultural practices near the site. Scattering coefficient
969 exhibits a similar weekly cycle as σ_{ap} during autumn (Fig. 3c) and the weekly σ_{ap} and
970 σ_{sp} cycle amplitudes are similar (~25%) during fall. Similarities in the autumn weekly σ_{ap}
971 and σ_{sp} cycles could simply be the result of a smaller compensating effect on σ_{sp} from
972 daytime secondary aerosol production during autumn (e.g., less photochemistry) or it
973 could be due to sources of scattering and absorbing aerosols that are more similar in autumn
974 than in summer. Diesel emissions from agricultural activity would seem more capable of
975 contributing to the weekly σ_{ap} cycle during autumn, when PBL heights are lower. Biomass
976 burning is a less likely source, even though Buzcu-Guven et al. (2007) reported a

977 significant biomass-burning influence on OM mass (38%) at BND. Absorption
978 Ångström exponent demonstrates minimal day of week variability during autumn (Fig. S15)
979 and α_{ap} values of 1.1-1.2 are not statistically different from the theoretical value of 1 for BC
980 (Bergstrom, et al., 2012).

981 **4.1.4 Temporal variability at EGB**

982 Annual PM1 σ_{sp} and σ_{ap} cycles at EGB (Fig(s). 2a and 2b) are influenced by more
983 polluted southerly air masses (120°-240° wind directions) during all seasons, along with
984 comparable contributions from less anthropogenically-perturbed W/NW wind sectors during
985 summer months (Fig. 7). Liggio et al. (2010) reported that S/SE wind directions were
986 generally associated with transport from the greater Toronto area and that SW wind
987 directions were often associated with more aged aerosol transported from the Ohio River
988 valley region or other urban areas. Wind speeds are lower in May-October and polluted
989 air masses from the south are typically associated with stagnant air masses ahead of fronts
990 (Yang et al., 2011).

991 Scattering coefficient is elevated for all wind sectors during summer (Fig. 7a). Warm-
992 season aerosol chemistry at EGB is influenced by temperature-dependent biogenic SOA
993 from forests to the north (Leaitch et al., 2011; Slowik et al., 2010) and by photo-oxidation
994 of anthropogenic pollutants from the south (Chan et al. 2010; Liggio et al., 2010).
995 Scattering coefficients exhibit larger summer increases for the less anthropogenically-
996 perturbed wind sectors (all except 120°-240° wind directions) than for the southerly wind
997 sectors (Fig. 7a). Monthly-median σ_{sp} for the southerly wind sectors are ~1.5 times higher in
998 summer than in spring and autumn, with larger summer σ_{sp} increases (factor of 2-5) for the
999 other wind sectors (unpublished result). The largest summer σ_{sp} increases are for NW wind
1000 sectors (Fig. 7a). In addition to biogenic SOA, the NW wind sectors are influenced in
1001 summer by regional tourist traffic and by episodic long-range transport of smoke during
1002 peak fire season in northwest Canada. However, it is not possible to distinguish the effects
1003 of aged smoke from biogenic SOA from forests, based on the available aerosol optical
1004 measurements during the 2010-2013 period at EGB. The secondary σ_{sp} peak in winter is
1005 influenced by higher σ_{sp} associated with air masses from the S/SW (Fig. 7a), relative to
1006 spring and autumn. Winter σ_{sp} for wind directions 150°-240° is ~2 times higher than σ_{sp} from
1007 other wind sectors (not shown). Single-scattering albedo is also highest for the 150°-240°

1008 wind sectors in winter, with values often 0.95 or above (Fig. S20a). Rupakheti et al. (2007)
1009 reported episodic high nitrate concentrations associated with air masses transported from
1010 urban areas south of EGB, mostly occurring during cold, humid conditions. Scattering
1011 coefficient does not exhibit a noticeable increase with decreasing winter temperatures at EGB
1012 during the 2010-2013 period (Fig. S5). Meteorology likely plays a role in the elevated winter
1013 σ_{sp} , as PBL heights in the region are lowest in winter at EGB (Horzworth, 1964).

1014 The annual σ_{ap} cycle (Fig. 2b) is qualitatively similar to annual EC mass concentration
1015 cycles reported for EGB (Yang et al. 2011) and for rural IMPROVE sites in the Great
1016 Lakes region (Spak and Holloway, 2009). Yang et al. (2011) reported mean EC
1017 concentrations (in units of $\mu\text{g m}^{-3}$) at EGB of 0.83 for summer, 0.71 for fall, 0.49 for
1018 winter, and 0.36 for spring. Spak and Holloway reported highest regional EC mass
1019 concentrations in summer and lowest in winter, with the June EC maxima ~ 2.2 times
1020 higher than the February EC minima. Our reported summer σ_{ap} maxima in August is 2-
1021 2.5 times larger than the broad November-April minima (Fig. 2b).

1022 Urban-influenced SE/S wind sectors are associated with highest σ_{ap} and lowest
1023 ω_0 for all seasons (Fig(s). 7b and S20a). Chan et al. (2010) attributed higher σ_{ap} , higher EC
1024 concentrations, and lower OC/EC ratios in air masses arriving at EGB from the south
1025 to diesel emissions. Absorption coefficients are lowest in winter for all wind sectors and
1026 are largest for southerly wind sectors during summer and autumn (Fig. 7b), with monthly-
1027 median σ_{ap} ~ 1.5 times higher in summer/autumn than in spring for these wind sectors.
1028 Much larger summer σ_{ap} increases (factors of $\sim 3-7$) are seen for westerly and northwesterly
1029 wind sectors (wind directions $\sim 240^\circ-360^\circ$). Episodic long-distance NW transport during the
1030 Canadian wildfire season may contribute to summer σ_{ap} but local/regional tourism traffic is
1031 more consistent with the observed summer weekly and diurnal σ_{ap} cycles.

1032 Weekly and diurnal σ_{ap} cycles at EGB are significant in summer, marginally significant in
1033 autumn, and insignificant in winter and spring (Fig(s). 4e and 4f). Summer and autumn
1034 diurnal σ_{ap} cycle amplitudes are $\sim 50\%$ and summer and autumn weakly σ_{ap} cycle amplitudes
1035 are $\sim 40\%$. The diurnal and weekly cycles in σ_{ap} during summer and autumn at EGB are more
1036 complicated than those at the other sites and are likely influenced to varying degrees by
1037 several sources, including (1) high volume of regional traffic during summer, largest on

1038 weekends; (2) transport of urban-influenced aerosol from the south; (3) diurnal PBL height
1039 evolution; and (4) local commuter traffic. Diurnal σ_{ap} cycles for individual days of the week
1040 reveal morning commuter peaks from Monday-Friday (unpublished result). Daytime σ_{ap}
1041 decreases due to lifting of the PBL height are dampened on each of these days by a large
1042 source of absorbing aerosol. Larger summer increases in σ_{ap} for westerly wind sectors
1043 suggests a source in addition to transport from the south. The large additional source is
1044 likely regional tourism traffic. Differences between post-dusk and pre-dawn σ_{ap} are small
1045 on Monday-Thursday (not shown) but are much larger on Friday ($\sim 1 \text{ Mm}^{-1}$) and Saturday
1046 ($\sim 2 \text{ Mm}^{-1}$) due to high volumes of weekend traffic. Post-dusk σ_{ap} on Sunday is $\sim 3 \text{ Mm}^{-1}$
1047 lower than pre-dawn σ_{ap} . The composite effect of these sources is the weekend σ_{ap} maxima
1048 and Monday minima during summer (Fig. 4e). The weekend σ_{ap} increase gives rise to a
1049 small decrease (0.02 to 0.03) in ω_0 and a small increase ($\sim 2 \text{ W m}^{-2} \text{ AOD}^{-1}$) in DRFE
1050 (Fig(s). S12-S13) Diurnal σ_{sp} cycles for individual days of the week during summer reveal
1051 some of the same features as σ_{ap} (unpublished result) but are further complicated by an
1052 additional large source of daytime scattering aerosol, likely photochemical production and
1053 transport of SOA.

1054 The autumn diurnal σ_{ap} cycle (Fig. 4e) appears to be more influenced by frequent
1055 transport from the south (Fig. 7b), along with less regional traffic than during summer.
1056 Monthly-averaged σ_{ap} during September-October (Fig. 2b) remains near summer levels (except
1057 for August) but σ_{ap} is much lower for all wind sectors except the urban-influenced southerly
1058 wind sectors, for which σ_{ap} was similar in value to summer (Fig. 7b). The diurnal σ_{ap} and σ_{sp}
1059 cycles exhibit very little structure during fall so lower fall PBL heights may be partially
1060 offset by lower production of scattering and absorbing aerosol and/or more efficient
1061 removal mechanisms. Some additional source may be responsible for the early-week
1062 increase in σ_{ap} , similar to that observed during autumn at BND (Fig. 4c). The source of
1063 absorbing aerosol persists throughout the day and into the evening (not shown) and may
1064 be local agricultural activities.

1065 **4.1.5 Temporal variability at SGP**

1066 PM1 particles contribute $\sim 66\%$ (78%) to the summer (winter) PM10 σ_{sp} and $\sim 85\%$ to both
1067 summer and winter PM10 σ_{ap} at SGP (Fig(s). 2c and S8c). The annual PM1 and PM10 σ_{ap}

1068 and σ_{sp} cycles are similar (Fig(s). 2a and S8a) so the PM1 AOP cycles at SGP are
1069 representative of the PM10 aerosol. The annual PM1 σ_{ap} cycle (Fig. 2b) demonstrates
1070 good overall agreement with the annual PM10 σ_{ap} cycle reported by D&O2002 for 1997-
1071 2000, with the exception that their winter σ_{ap} minima extends from November-February
1072 while our σ_{ap} minima extends from January-February. The annual PM1 σ_{sp} cycle during
1073 2010-2013 (Fig. 2a) also agrees well with that reported by D&O2002 for most non-winter
1074 months. D&O2002 reported a broad summer maxima, with monthly median σ_{sp} values
1075 lying ~30-40% above spring and autumn months. Our σ_{sp} cycle during non-winter months
1076 differs only by a larger summer-to-autumn σ_{sp} decrease of close to factor of 2. Agreement
1077 is worse for winter months. Both D&O2002 and Sheridan et al. (2001) reported minimum
1078 σ_{sp} in December and maximum in February, with median February σ_{sp} a factor of ~4 higher
1079 than December. Box plots of monthly-binned σ_{sp} for individual 2010-2013 years (Fig.
1080 S4) show that median February σ_{sp} at SGP varies by up to a factor of 4 for different
1081 years, with somewhat smaller differences between individual January months (factor of ~2)
1082 and between individual March months (factor of ~2-3). Much of the inter-annual variability
1083 is smoothed out in the monthly-binned σ_{sp} box plot for the entire period (Fig. S3), giving rise
1084 to relatively constant monthly-mean σ_{sp} during winter for the current period (Fig. 2a).
1085 Lower December σ_{sp} and much higher February σ_{sp} occurred during the period reported by
1086 D&O2002 and Sheridan et al. (2001), compared to the period reported here.

1087 Pollution transport from the S/SE impacts PM1 σ_{ap} and σ_{sp} throughout the year (Fig.
1088 8). Wind directions are primarily from the S/SE for non-winter months (especially
1089 summer). Air mass back-trajectories show that air masses arriving at SGP from the S/SE
1090 often travel over or near large regional populations centers, including Oklahoma City, Tulsa,
1091 and (in summer) Dallas/Fort Worth (Parworth et al., 2015). Single-scattering albedo is
1092 generally lower for S/SE wind sectors than for the less anthropogenically-influenced
1093 westerly and northerly wind sectors, except during summer (Fig. S22a). A large fraction of
1094 non-refractory PM1 aerosol mass (~70%) is aged SOA during April-October (Parworth et
1095 al., 2015). Many SE trajectories pass over regions of high summer isoprene emissions
1096 (Parworth et al., 2015) but the temperature-dependence of σ_{sp} (Fig(s). S5 and S7) is less
1097 than for the sites with known biogenic SOA influence (EGB and APP). Absorption
1098 Ångström exponent values close to 1 for all seasons (Fig. 2h) suggest that despite high

1099 organic composition, light-absorbing OC exerts a minimal influence on the annual σ_{ap} cycle
1100 and that most of the absorbing aerosol is BC. Daily averages of α_{ap} can have values that
1101 extend to as high as 2.5 (unpublished result), which is consistent with observed plumes of
1102 biomass burning aerosol reported by Parworth et al. (2015). Other than lower σ_{sp} during
1103 autumn, σ_{sp} and σ_{ap} for the S/SE wind sectors do not demonstrate much seasonality (Fig. 8).
1104 The lack of seasonal variability in mean σ_{ap} and σ_{sp} during non-winter months (relative to
1105 the other sites) may be due to a longer distance from the population centers (increased
1106 aerosol dispersion) and higher PBL heights at SGP during spring, summer, and autumn.
1107 Removal processes may also be more efficient in late spring and summer, when monthly-
1108 averaged rainfall at SGP is highest.

1109 The frequency of episodic transport of ammonium nitrate to SGP likely exerts some
1110 influence on winter σ_{sp} and its variability. Parworth et al. (2015) reported that ammonium
1111 nitrate comprised approximately half of the non-refractory PM1 mass at SGP during the
1112 2010-2011 and 2011-2012 winters and early-springs (e.g., March) (their Fig(s). 2 and 6).
1113 Ammonia and NO_x concentrations near SGP are relatively small and high nitrate episodes
1114 (mass concentrations $> 3 \mu\text{g m}^{-3}$) were nearly always associated with temperatures $< 3 \text{ }^\circ\text{C}$
1115 and long-distance transport from agricultural states in the Central Great Plains region.
1116 Colder temperatures and more frequent long-distance transport passing over these states
1117 likely contributed to nearly a factor of 2 higher average ammonium nitrate concentrations
1118 during the 2010-2011 winter than the 2011-2012 winter (Parworth et al., 2015). Average
1119 OA concentrations were similar between the two winters so variability in ammonium nitrate
1120 likely exerted an influence on the ~50% higher average PM1 mass concentration during the
1121 2010-2011 winter. Lower relative humidity during the 2010-2011 winter indicates that less
1122 wet deposition could also have contributed to higher PM1 aerosol mass during that winter
1123 (Parworth et al., 2015). The frequency of episodically- transported biomass burning aerosol
1124 also influences σ_{sp} and σ_{ap} at SGP. Biomass burning aerosol is most prevalent in the spring,
1125 when prescribed crop burning in preparation of planting is more common. Parworth
1126 et.al. (2015) reported a much larger biomass burning aerosol influence in spring 2011
1127 than spring 2012, primarily in March-April. Differences are observed in the mean σ_{sp} and
1128 σ_{ap} between the two springs, in addition to differences in the 50th, 75th, and 95th
1129 percentiles between the two springs (Fig. S4). Differences between the two years are more

1130 noticeable for σ_{ap} than for σ_{sp} .

1131 Diurnal σ_{ap} cycle amplitudes (Fig. 4h) are near 40% for all seasons except spring
1132 (25%). Only the summer and autumn cycles are statistically significant. Diurnal PBL height
1133 effects are clearly visible in the diurnal σ_{ap} cycles (Fig. 4h), as is a lack of commuter
1134 influence. Similar to BND, there is no local commuter traffic that would be expected to
1135 influence AOP cycles at SGP. No obvious features are seen in the individual day of
1136 week σ_{ap} cycles (unpublished result) to indicate a possible role of interstate traffic or
1137 agricultural influences in the weekly or diurnal σ_{ap} cycles (Fig(s). 4g-h). This is
1138 complicated by biased SGP σ_{ap} observations during the weekends. The diurnal σ_{sp} cycle is
1139 insignificant for all seasons (Fig. 3h), which may reflect increased daytime photochemical
1140 processing that is somewhat less in the winter months. Larger mid-day decreases in σ_{ap}
1141 than σ_{sp} lead to increases in ω_0 of ~ 0.03 . The hemispheric backscatter fraction varies
1142 negligibly during the day. The midday increase in ω_0 leads to more negative midday
1143 DRFE, by $\sim 3 \text{ W m}^{-2} \text{ AOD}^{-1}$ in all and $2 \text{ W m}^{-2} \text{ AOD}^{-1}$ in summer. The aerosol
1144 parameters related to size show contrasting trends. No visible diurnal or weekly trend is
1145 apparent in b while α_{sp} shows a decline with larger aerosol in the early evening. The trend
1146 in declining afternoon α_{sp} values starts earlier in the day during the winter and is weakest
1147 during the summer and spring.

1148 **4.2 Regional variability of aerosol optical properties**

1149 Regional differences in some annually-averaged AOPs (Fig. 2; Table S5) are unbiased by
1150 single months or seasons. PM1 σ_{sp} is highest at BND and lowest at EGB, with annual-mean
1151 σ_{sp} 70% higher at BND than at EGB (Fig. 2a). The regional differences in σ_{sp} reflect the fact
1152 that the upper Midwestern US is more anthropogenically-influenced than the other three
1153 regions, with more large population centers, high concentrations of coal-burning power
1154 plants, higher volumes of traffic, and more agricultural activity. Spak and Holloway
1155 (2009) concluded that “*PM2.5 is a year-round air quality problem in the upper*
1156 *Midwestern US and Southern Canada, driven by nitrate in the winter, sulfate in the*
1157 *summer, and ammonium, OA, EC, and other components year-round*”. The largest
1158 winter σ_{sp} peak at BND may be due to higher levels of regional ammonium nitrate
1159 precursors and cold, humid winter conditions favorable for ammonium nitrate production

1160 in the upper Midwestern US, where winter ammonium nitrate concentrations are higher than
1161 almost all other regions in the US (Hand et al., 2012b). The annual σ_{sp} cycle at APP
1162 (Fig. 2a) is driven almost completely by the seasonality of regional SOA and sulfate
1163 production (Goldstein et al., 2009; Hidy et al., 2014) due to the lack of urban influence on
1164 AOPs at APP. Both SGP and EGB are located downwind at times from large urban centers
1165 but both sites receive only a small anthropogenic contribution from all but southerly wind
1166 sectors. More frequent polluted air masses from the south may be the reason for higher σ_{sp} at
1167 SGP than at EGB for all but summer months (Fig(s). 7a and 8a).

1168 PM1 aerosol contributes a larger fraction to PM10 σ_{sp} and σ_{ap} at APP than at BND and
1169 SGP, as evidenced by higher R_{sp} (Fig. 2c) and higher R_{ap} (Fig. S8c). Both R_{sp} and R_{ap} are
1170 the highest at APP for all months. The regional differences in R_{sp} are significant for all
1171 months (Fig. 2c). Differences in R_{ap} between APP and BND are only significant for
1172 November-March (Fig. S8c). The regional differences in R_{sp} and R_{ap} are likely due to a
1173 larger influence of soil dust to PM10 AOPs at SGP and BND. Sea salt concentrations are
1174 minimal in all three regions and soil dust concentrations are higher in the agriculturally-
1175 influenced Midwestern US and Southern Great Plains than in the Appalachian mountain
1176 region (Hand et al., 2012b). Given the higher density of forests near EGB than near BND
1177 and SGP, it is likely that R_{sp} and R_{ap} would be higher at EGB (if measured there) than at
1178 SGP and BND. A larger regional agricultural influence near EGB than near APP may give
1179 rise to R_{sp} and R_{ap} that are slightly lower than those at APP. Other indicators of aerosol size
1180 distribution (PM1 b and PM10 α_{sp}) also follow similar seasonal cycles at BND and SGP
1181 (Fig(s). 2d and 2g). One notable difference is lower α_{sp} at SGP (by ~ 0.3) for nearly all
1182 months. Similar R_{sp} and b values but different α_{sp} could be indicative of differences in the
1183 larger part of the accumulation mode (particle diameters close to 1 μm). APP and EGB
1184 have very similar b values for warm-season months (May-October), which is likely due to
1185 large biogenic SOA influences during the warm season in both regions (Goldstein et al.,
1186 2009; Link et al., 2015; Leitch et al., 2011; Slowik et al., 2010). The highest annually-
1187 averaged b at APP amongst the sites (Fig. 2d) is influenced by cold-season months
1188 (November-April). EGB is influenced by large, highly-scattering PM1 particles from the
1189 south during winter months (Fig. S20). Winter PM1 aerosol at APP is largely regional
1190 SOA and sulfate, with some influence from biomass-burning aerosol (Supplemental

1191 Materials to Link et al., 2015). Higher b at APP during winter and the surrounding months
1192 could be due to less particle growth (photochemistry).

1193 The differences between annually-averaged σ_{ap} among the sites is insignificant (Fig. 2b),
1194 based on σ_{ap} precision measurement uncertainties (Table 3). Differences in monthly-mean
1195 σ_{ap} among the sites are insignificant for most months. The only exceptions are (1) EGB σ_{ap} is
1196 lower than APP in April and lower than APP and BND in November; (2) SGP σ_{ap} is lower
1197 than BND in August. The annual σ_{ap} cycle amplitudes are larger at BND and EGB than
1198 at APP and SGP. Larger σ_{ap} increases during summer and the surrounding months at
1199 BND and EGB are consistent with higher levels of regional traffic during these months.
1200 The smaller annual σ_{ap} cycle amplitudes at APP and SGP may be influenced by their further
1201 proximity from large urban centers. Biomass-burning aerosols also influence σ_{ap} to some
1202 degree at APP during winter (Supplemental Materials to Link et al., 2015) and at SGP
1203 during winter and spring (Parworth et al., 2015) and may also dampen the σ_{ap} cycles at
1204 APP and SGP. Absorption Ångström exponents (Fig. 2h) support the assertion that biomass
1205 burning aerosol may influence winter monthly-mean σ_{ap} at APP in November-February
1206 (Cazorla et al., 2013). Monthly-mean α_{ap} , however, is not significantly greater than 1 during
1207 any other months at SGP, BND, and APP, given the α_{ap} measurement precision uncertainty
1208 (Table 3).

1209 Annually-averaged PM1 ω_0 and DRFE are statistically similar for APP, BND, and SGP.
1210 Lower annually-averaged ω_0 (Fig. 2e) and higher (less-negative) annually-averaged DRFE
1211 (Fig. 2f) at EGB are marginally-significant (at 95% confidence) and these differences are
1212 heavily biased by September and October. The simple use of annually-averaged values to
1213 discuss regional ω_0 variability (Fig. 2e) is a bit misleading, given the large seasonal ω_0
1214 variability at BND and EGB (and to a lesser degree-APP and SGP). Monthly-averaged ω_0
1215 at EGB is close to 0.10 lower than that at APP and SGP during September-October and
1216 is also 0.08 lower than annually-averaged ω_0 at EGB. Single-scattering albedo differences
1217 between APP and BND are nearly this large in winter, despite the fact that annually-
1218 averaged ω_0 is statistically indistinguishable at the two sites. The regional ω_0 differences are
1219 at least as large as reported ω_0 differences among BND, SGP, and two North American
1220 coastal sites - Barrow, Alaska and Sable Island, Nova Scotia (D&O2002). In spite of the

1221 high seasonality in ω_0 and b , the co-variation of these two intensive properties lead to
1222 insignificant annual DRFE cycles at APP and SGP. Larger DRFE cycle amplitudes are
1223 observed at EGB ($\sim 9 \text{ W m}^{-2} \text{ AOD}^{-1}$) and BND ($\sim 6 \text{ W m}^{-2} \text{ AOD}^{-1}$), with September-
1224 October DRFE maxima (least negative (DRFE) at both sites (Fig. 2f).

1225 **4.3 Long-term aerosol optical property trends at BND and SGP**

1226 Trends in AOPs are calculated for the PM10 and PM1 size cuts at BND and SGP. In
1227 general, the sign of the AOP trends are the same for both size cuts, although the magnitudes
1228 of the trends differ. With the exception of α_{sp} , where the PM10 value is more meaningful, we
1229 focus on the PM1 AOP trends for consistency with the rest of the paper. Statistically
1230 significant trends in PM1 σ_{sp} (decreasing), R_{sp} (decreasing), and PM1 b (increasing) are found
1231 at BND from 1996-2013 and at SGP from 1997-2013 (Table 4). Visual examination of
1232 Figure 9 reveals that the trends in these AOPs since ~2009 are somewhat more pronounced
1233 than in earlier years, pointing out the pitfalls associated with trend analysis on short-term time
1234 series. Additionally, there is a statistically significant decreasing trend in PM10 α_{sp} at SGP
1235 (Table 4; Fig. S24); the BND trend in σ_{ap} is negative but not statistically significant. BND
1236 also demonstrates a slight, but statistically significant negative trend in ω_0 (Table 4; Fig. S25).
1237 The significant decrease in σ_{sp} at both sites is consistent with other studies (CC2013; Hand et
1238 al., 2014) that reported large decreases in near-surface aerosol light scattering and light
1239 extinction coefficients in North America during the past decade. The concurrent decreasing
1240 trend in R_{sp} implies that scattering by PM1 is decreasing at a faster rate than scattering by
1241 super-1 μm particles (which may or may not be decreasing) at both BND and SGP. One
1242 possible source for reductions in PM1 σ_{sp} at BND and SGP could be decreasing SO_2
1243 emissions by regional power plants. Annual US SO_2 emissions from power plants decreased
1244 at a rate of $\sim 6\%$ per year from 2001-2010, with similar reductions in sulfate concentrations at
1245 rural US sites (Hand et al., 2012a).

1246 CC2013, performed trend analyses on σ_{sp} , σ_{ap} , α_{sp} , and b at BND and SGP as part of a
1247 larger study looking at long term changes in in-situ aerosol properties measured around the
1248 globe. There are several key differences between our analysis and that of CC2013 so the
1249 magnitudes of the trends should not be directly compared, but the signs of the trends
1250 (positive/negative) can be compared. Differences between the two studies include: (1)

1251 monthly data are used in our analysis (CC2013 used daily); (2) our trend analysis extends the
1252 data sets three more years past that of CC2013; (3) we report trends for both PM10 and PM1
1253 AOPs (CC2013 used PM10 AOPs); and (4) we reference the percent slope to the first year
1254 value while CC2013 referenced their slope to the median value of the parameter for the entire
1255 data set.

1256 For σ_{sp} and σ_{ap} , the direction (positive/negative) of the trends in CC2013 and this study are
1257 the same. CC2013 reported larger trends for σ_{ap} and σ_{sp} than are found here, likely due to a
1258 combination of the differences between the two analyses noted above. One noticeable
1259 difference between CC2013 and this study is that CC2013 found a statistically significant
1260 decrease in BND PM10 σ_{ap} at the $p < 0.05$ level, while the decreasing trend for PM10 σ_{ap}
1261 calculated here is not statistically significant. CC2013's analysis also included b and α_{sp}
1262 trends at BND and SGP. Unlike the analysis performed here, they found no statistically
1263 significant trends in either b or α_{sp} when using the Mann-Kendall test with Sen's slope (MK),
1264 although the signs of their MK slopes match what is reported in Table 4 for this study.
1265 CC2013 found significant positive trends in b at both sites and a negative trend in α_{sp} at SGP
1266 when they applied the generalized least square trend test with autoregressive bootstrap
1267 confidence intervals (GLS/ARB). CC2013 hypothesized that this discrepancy could be the
1268 result of lower sensitivity of the MK method for trends in normally-distributed data. Most
1269 intensive AOPs are closer to normally-distributed than are σ_{sp} and σ_{ap} , a point noted by C2013
1270 and confirmed by the authors using data at the four sites reported in our study. CC2013's
1271 trend slope in b using the GLS/ARB method was nearly identical in magnitude (7.7% per 10
1272 year) to our slope for BND (Table 4) while their trend slope in b at SGP was smaller (7.8%
1273 per 10 year) than our slope. The trend slope in α_{sp} reported by CC2013 for SGP (- 4.2% at
1274 SGP) is very similar to our trend slope (Table 4). CC2013 did not analyze trends in ω_0 .

1275 **4.4 Systematic relationships among aerosol optical properties**

1276 Most systematic relationships amongst AOPs are qualitatively similar for all seasons at
1277 each site and are suitably represented by the annual relationships. Several of these annual
1278 relationships have also been reported for BND and SGP by others (D&O2002; Andrews et
1279 al., 2011) and most are similar to the relationships reported here for BND and SGP. We
1280 briefly summarize these relationships (Sect. 4.4.1) and highlight any differences in the BND

1281 and SGP relationships for our study period (compared to D&O2002 and Andrews et al.,
1282 2011), in addition to any differences in the relationships at BND and SGP and those at APP
1283 and EGB, which have not been studied. Relationships involving α_{ap} are seasonally-dependent
1284 (especially at APP) and are hence presented for individual seasons at APP, BND, and SGP in
1285 Sect. 4.4.2.

1286 **4.4.1 Annual systematic relationships among AOPs**

1287 Single scattering albedo increases and b decreases with increasing σ_{sp} at all sites (Fig(s).
1288 10a-b). Hemispheric backscatter fraction demonstrates an inverse relationship with ω_0 over
1289 the entire ω_0 range at EGN and for $\omega_0 > 0.85$ at the other sites (Fig. 10c), a condition
1290 representative of all months (Fig(s). 2d-e). The co-variability of ω_0 and b leads to a DRFE
1291 dependence on σ_{sp} that is statistically insignificant for all sites, with the exception of the
1292 lowest σ_{sp} conditions at APP (Fig. 10d). Greater influences by smaller, darker particles
1293 under low-loading conditions and by larger, brighter particles under high-loading conditions
1294 are seen in the annual σ_{sp} , b , and ω_0 cycles for the four sites in this paper (Fig(s). 2a, 2d, and
1295 2e) and have been reported for SGP and BND by D&O2002. The tendency toward lower ω_0
1296 and higher b for low-loading conditions is consistent with preferential removal of large,
1297 less-absorbing particles by cloud scavenging and/or wet deposition. It can also be the result
1298 of new particle formation with growth by condensation and/or coagulation to optically-
1299 active sizes (Andrews et al., 2011). Scattering Ångström exponent and R_{sp} are both
1300 relatively insensitive to changes in σ_{sp} at APP over the entire σ_{sp} range (Fig(s). 10e-f).
1301 Scattering Ångström exponent is insensitive to changes in σ_{sp} for all but the lowest aerosol
1302 loading levels at BND and SGP (Fig. 10e). PM1 scattering fraction shows a modest
1303 decrease with increasing σ_{sp} for $\sigma_{sp} > 20 \text{ Mm}^{-1}$ at BND and SGP (Fig. 10f). A similar lack of
1304 sensitivity of α_{sp} to changes in σ_{sp} at SGP and BND was reported by D&O2002. PM1
1305 scattering fraction increases proportionally with α_{sp} at APP, BND, and SGP (Fig. 10g).
1306 D&O2002 reported similar R_{sp} vs. α_{sp} relationships for SGP and BND. The fact that the R_{sp}
1307 vs α_{sp} relationship is much stronger than either of their relationships with σ_{sp} suggests that
1308 α_{sp} is a better indicator of the relative contributions of coarse and fine mode aerosol to PM10
1309 σ_{sp} than an indicator of average particle size—at least for APP, BND, and SGP. Based on the
1310 range of R_{sp} values measured at SGP, BND, and APP (Fig. 2c), the aerosol size distributions

1311 are on average bi-modal (with higher coarse mode fractions at SGP and BND than at APP)
1312 and care must be exercised when using α_{sp} to infer average particle size or aerosol type. The
1313 R_{sp} vs α_{sp} relationship (Fig. 10g) is consistent with decreasing trends in both R_{sp} and α_{sp} at
1314 SGP (Table 4) but seems inconsistent with the lack of change in α_{sp} at BND, despite
1315 reductions in R_{sp} similar in magnitude to those at SGP.

1316 AOPs at the rural continental sites reported here have similar relationships (Fig. 10) as
1317 those at a majority of mountain sites reported on by Andrews et al. (2011). Andrews et al.
1318 (2011) also reported relationships amongst AOPs based on long-term aircraft
1319 measurements made over BND and SGP, although their free tropospheric AOP
1320 relationships for BND and SGP only extended up to $\sigma_{sp} \sim 25 \text{ Mm}^{-1}$. Most of the free
1321 troposphere AOP relationships reported for SGP (Andrews et al., 2011) are similar to the
1322 corresponding near-surface AOP relationships (Fig. 10) but there are some noticeable
1323 differences for BND. Andrews et al. (2011) reported the following AOP relationships as σ_{sp}
1324 increased from zero to 25 Mm^{-1} at BND: (1) b increased slightly (0.12 to 0.13); (2) ω_0
1325 remained nearly constant (less than 0.01 increase); and (3) α_{sp} increased by a larger amount
1326 (~ 0.12 to 0.17) than in our study (Fig. 10e). The differences between these relationships and
1327 those in Figures 10a, 10b, and 10e could be due to smaller particles that undergo less
1328 atmospheric processing (particle growth, cloud scavenging, and deposition) in the free
1329 troposphere above BND, relative to particles near the surface.

1330 **4.4.2 Seasonal relationships involving absorption Ångström exponent**

1331 The relationships between α_{ap} and σ_{sp} for individual seasons and the annual relationship
1332 are most different at APP (Fig. 11a) and least different at BND (Fig. 11b). Absorption
1333 Ångström exponent at APP is statistically higher than 1 ($\alpha_{ap} \geq 1.2$) for all σ_{sp} bins during
1334 winter and is statistically lower than 1 ($\alpha_{ap} \leq 0.8$) for all σ_{sp} bins during summer and for
1335 higher-loading conditions ($\sigma_{sp} \geq 50 \text{ Mm}^{-1}$) during spring and autumn (Fig. 11a). Absorption
1336 Ångström exponent at BND (Fig. 11b) and SGP (Fig. 10c) is not statistically different from
1337 1 for any σ_{sp} bins except for (1) summer loading $\sigma_{sp} \geq 30 \text{ Mm}^{-1}$; and (2) spring and autumn
1338 loading $\sigma_{sp} \geq 80 \text{ Mm}^{-1}$ (SGP only). Relationships among α_{ap} and intensive AOPs (α_{sp} and
1339 ω_0) can be used to identify contributions to σ_{ap} by sources other than BC, such as dust, OC,
1340 and coated BC (Cazorla, et al., 2013; Costabile et al., 2013; Gyawali et al., 2009).

1341 Absorption Ångström exponent exhibits a systematic decrease with increasing α_{sp} for all
1342 seasons at SGP (Fig. 11f) and α_{sp} decreases in a step-wise manner for all seasons except
1343 summer at BND (Fig. 11f). The α_{ap} - α_{sp} relationship is more complicated at APP, (Fig.
1344 11d), where α_{ap} demonstrates a similar decrease with increasing α_{sp} during summer to that
1345 observed at BND but a marginally-significant increase with increasing α_{sp} during winter.
1346 Values of α_{ap} that are statistically higher than 1 ($\alpha_{sp} \geq 1.2$) tend to be associated with $\alpha_{sp} \geq$
1347 1.5 at APP (Fig. 11d), suggesting a mix of EC and OC (Fig. 2 of Cazorla, et al., 2013).
1348 Values of $\alpha_{sp} \geq 1.2$ at BND and SGP are most often associated with $\alpha_{sp} < 1$ (Fig(s).
1349 11e-f), suggesting a mix of EC and dust (Fig. 2 of Cazorla et al., 2013). Dust influences σ_{ap}
1350 at SGP during all seasons and also influences BND σ_{ap} during autumn, as seen by the
1351 number of data points with $\alpha_{sp} \geq 1.2$ and $\alpha_{sp} < 1$ in Fig(s). 11e-f. Episodic biomass
1352 burning that impacts SGP during spring (Parworth et al., 2015) also contributes to high
1353 α_{ap} values, which can reach ~ 2.5 for individual days (unpublished result). Summer values
1354 of α_{ap} are lower than those of other seasons for all α_{sp} bins at BND and APP and for all but
1355 the lowest α_{sp} bins at SGP (where dust likely influenced absorption). The slopes of the α_{ap}
1356 vs α_{sp} curves indicates that α_{ap} values significantly lower than 1 during summer coincide
1357 with higher fractions of fine-mode aerosol (higher α_{sp}).

1358 The annual α_{ap} - ω_0 relationships for all individual seasons are also most similar at BND
1359 (Fig. 11h) and least similar at APP (Fig. 11g), where the summer and winter α_{ap} - ω_0
1360 relationships are noticeably different. Absorption Ångström exponent is lowest over the
1361 entire ω_0 range during summer at all sites. All of the individual season α_{ap} - ω_0 curves are
1362 similar in that α_{ap} remains constant or slightly increasing with increasing ω_0 until ω_0
1363 approaches 0.90 (specifically the ω_0 bin centered at 0.875). This is followed by sharp
1364 decreases in α_{ap} with further increases in ω_0 . Absorption Ångström exponents significantly
1365 less than 1 ($\alpha_{ap} \leq 0.8$) during summer months coincide with $\omega_0 \geq 0.85$ at APP, $\omega_0 \geq 0.90$ at
1366 BND, and $\omega_0 \geq 0.95$ at SGP. Absorption Ångström exponent at APP is also significantly less
1367 than 1 for $\omega_0 \geq 0.95$ during autumn. From the b vs. ω_0 relationships (Fig. 10c), the lower
1368 mean α_{ap} values at all sites during summer also coincide with lower mean b values. When
1369 combined, these relationships indicate that lower α_{ap} values are associated with larger,
1370 less-absorbing, fine-mode particles. Gyawali et al. (2009) reported a similar α_{ap} - ω_0

1371 relationship for summer months with no biomass burning influence in Reno, NV. Single-
1372 scattering albedo was near constant ($\alpha_{ap} \sim 1.1-1.2$) up to $\omega_0 \sim 0.90$, followed by α_{ap} values
1373 mostly below one for higher ω_0 . Gyawali et al. (2009) attributed this wavelength dependence
1374 of absorption to EC particles coated with non-absorbing organic and inorganic matter. It
1375 should be noted that Gyawali et al. (2009) used a photo-acoustic spectrometer, as
1376 compared to the filter-based techniques that are employed at the sites in this study.
1377 Gyawali et al. (2009) also used different wavelengths (405 nm and 870 nm) so the
1378 results are not directly comparable. The summer values of α_{ap} at APP are also much lower for
1379 all ω_0 than those reported by Gyawali et al. (2009). Possible biases in filter-based absorption
1380 measurements made in high-OA environments could in principle contribute to this result
1381 (e.g., Lack et al., 2008; Lack et al., 2009). A detailed analysis of the effects, both real
1382 and artifact, of absorbing and non-absorbing coatings on the wavelength-dependence of
1383 light absorption by black carbon is beyond the scope of this paper.

1384 **5 Summary and conclusions**

1385 Seasonal variability of nearly all PM1 AOPs is generally much larger than weekly and
1386 diurnal AOP variability at the APP, BND, EGB, and SGP surface aerosol monitoring
1387 stations. All sites exhibit summer σ_{sp} maxima (Fig. 2a) and broader summer σ_{ap} maxima
1388 (Fig. 2b). Secondary winter peaks in σ_{sp} are observed at all sites except APP and coincide
1389 with minimum σ_{ap} . Scattering coefficient is lowest at all sites except APP during autumn.
1390 Low autumn σ_{sp} coincides with ω_0 minima (Fig. 2e) and b maxima (Fig. 2d) at all sites. In
1391 spite of the high seasonality in ω_0 and b , the co-variation of these two intensive properties
1392 lead to insignificant annual DRFE cycles at APP and SGP. Larger DRFE cycle amplitudes are
1393 observed at EGB (~40%) and BND (~25%), with September-October DRFE maxima (least
1394 negative (DRFE) at both sites (Fig. 2f). Regional differences in annual mean AOPs are in
1395 general much less than their seasonal variability at individual sites (Fig. 2), requiring that
1396 studies of regional AOP variability be conducted on a seasonal basis. Amplitudes of diurnal
1397 and weekly cycles in σ_{ap} at the sites (Fig. 4) are larger for all seasons than those of σ_{sp}
1398 (Fig. 3), with the largest differences occurring in summer. The weekly and diurnal cycle
1399 amplitudes of most intensive AOPs are minimal in most cases, especially those related to
1400 parameterizations of aerosol size distribution. Statistically- significant trends in σ_{sp}
1401 (decreasing), R_{sp} (decreasing), and b (increasing) are found at BND from 1996-2013 and

1402 at SGP from 1997-2013 (Table 4). A statistically significant decreasing trend in α_{sp} is also
1403 observed for SGP but not BND.

1404 Systematic relationships among ω_0 , σ_{sp} and b (Fig(s). 10a-d) show that high aerosol
1405 loading conditions are associated with larger, less absorbing particles and that low aerosol
1406 loading conditions are associated with smaller, more absorbing particles for all sites and
1407 seasons. These relationships are consistent with other studies (D&O2002; Andrews et al.,
1408 2011) and suggest the influences of particle growth, wet deposition, and cloud/fog
1409 scavenging of larger, less-absorbing particles on σ_{sp} and b (Andrews et al., 2011).
1410 Systematic relationships among α_{ap} , σ_{sp} , and α_{sp} (Fig(s). 11a-f) suggest that aerosol light
1411 absorption is largely due to EC for all sites and seasons, with the exception of a mixture of
1412 EC and light-absorbing OC during winter at APP. Dust and OC likely influence σ_{ap}
1413 episodically at SGP (Fig(s). 11c and 11f). The α_{ap} - α_{sp} relationships for SGP (Fig. 11f)
1414 and BND (Fig. 11e) are consistent with a mixture of EC and dust for the majority of higher
1415 α_{ap} values ($\alpha_{sp} \geq 1.2$) at SGP during all seasons and BND during autumn. The relationships
1416 between α_{ap} and ω_0 indicate that values of α_{ap} significantly less than 1 are associated with
1417 weakly-absorbing particles. When combined with the ω_0 - b relationships (Fig. 10c), the
1418 confluence of low α_{ap} , high ω_0 , and low b may suggest an influence of coated EC on
1419 low σ_{ap} during summer (Gyawali et al., 2009). More detailed studies involving aerosol
1420 chemistry and size distributions are clearly needed to state this more definitively.

1421 Many general features of the annual σ_{sp} and σ_{ap} cycles and the weekly and diurnal σ_{ap}
1422 cycles at the sites are explained (Sect(s) 4.1.1-4.1.5) in a self-consistent manner using (1)
1423 pollution-rose diagrams showing the seasonality of pollution transport (Figs. 5-8); (2)
1424 published aerosol chemistry at the sites (Link et al., 2015; Parworth et al., 2015; Yang et al.,
1425 2011 and references therein; Buzcu-Guven et al., 2007); (3) temperature-dependence of some
1426 known regional σ_{sp} sources; and (4) reported seasonality of PBL heights for the regions.
1427 One exception deals with the σ_{ap} cycles at APP. The influence of local traffic is seen in the
1428 diurnal σ_{ap} cycles (Fig. 4b) and possibly the weekly σ_{ap} cycles (Fig. 4a). Local and regional
1429 wood-burning influence during winter is also consistent with reported aerosol chemistry at
1430 APP (Supplemental Materials to Link et al., 2015) and with winter-month α_{ap} values (Fig.
1431 2h) and their relationship with α_{sp} (Fig. 11d). However, neither of these sources nor the

1432 seasonality of transport of moderately-elevated σ_{ap} from the northeast (Fig. 5b) adequately
1433 explain the annual σ_{ap} cycle at APP. More studies are also needed to better understand
1434 the differences in σ_{ap} and σ_{sp} cycle amplitudes on weekly and diurnal timescales,
1435 especially in summer. The potential influence of photochemistry on the annual σ_{sp} cycles is
1436 consistent with published aerosol chemistry at the sites. We hypothesize that local
1437 photochemical aerosol production could also provide the large daytime source of
1438 scattering aerosols during summer and surrounding months that counteracts diurnal PBL
1439 height variation, leading to much smaller diurnal cycles in σ_{sp} than σ_{ap} . However, the
1440 available datasets in this study are not sufficient to test this hypothesis. Relationships
1441 between AOPs and meteorology are also necessary to better understand the effects of
1442 atmospheric processing on AOPs at the four sites and their annual and diurnal cycles.

1443 **Acknowledgements**

1444 Funding for obtaining and evaluating the data came from the DOE ARM program, NOAA
1445 Climate Program Office, Appalachian State University College of Arts and Sciences,
1446 and Environment Canada, Atmospheric Science and Technology Directorate. We thank the
1447 technicians, students, and support staff at all the sites for the dedication and diligence,
1448 24/7/365, required to produce the data sets reported here.

1449 **References**

- 1450 Anderson, T.L. and Ogren, J. A.: Determining aerosol radiative properties using the TSI 3563
1451 1400 integrating nephelometer, *Aerosol Sci. Technol.*, 29, 57-69, 1998.
- 1452 Anderson, T.L., Covert, D.S., Wheeler, J.D., Harris, J. M., Perry, K.D., Trost, B.E., Jaffe,
1453 D.J., and Ogren, J.A.: Aerosol backscatter fraction and single-scattering albedo:
1454 Measured values and uncertainties at a coastal station in the Pacific Northwest, *J.*
1455 *Geophys. Res.*, 104, D21, 26793-26807, doi:10.1029/1999JD900172, 1999.
- 1456 Anderson, T.L., Masonis, S.J. Covert, D.S., Ahlquist, N.C., Howell, S.G., Clarke, A.D.,
1457 and McNaughton, C.S. : Variability of aerosol optical properties derived from in situ
1458 aircraft measurements during ACE-Asia, *J. Geophys. Res.*, 108, D23, 8647,
1459 doi:10.1029/2002JD003247, 2003.
- 1460 Andreae, M.O., Jones, C.D., and Cox, P.M.: Strong present-day aerosol cooling implies a hot

- 1461 future, *Nature*, 435, 1187-1190, 2005.
- 1462 Andrews, E., Sheridan, P.J., Ogren, J.A., and Ferrare, R.: In situ aerosol profiles over the
1463 Southern Great Plains cloud and radiation test bed site: 1. Aerosol optical properties, *J.*
1464 *Geophys. Res.* 109, D06208, doi:10.1029/2003JD004025, 2004.
- 1465 Andrews, E., Ogren, J.A., Bonasoni, P., Marinoni, A., Cuevas, E., Rodriguez, S., Sun,
1466 J.Y., Jaffe, D.A., Fischer, E.V., Baltensperger, U., Weingartner, E., Collaud Coen, M.,
1467 Sharma, S., Macdonald, A.M., Leaitch, W.R., Lin, N.-H., Laj, P., Arsov, T., Kalapov, I.,
1468 Jefferson, A., and Sheridan, P.: Climatology of aerosol radiative properties in the free
1469 troposphere, *Atmos. Res.*, 102, 365-393, 2011.
- 1470 Bae M., Schaur, J.J., DeMinter J.T., and Turner, J.R.: Hourly and daily patterns of
1471 particulate- phase organic and elemental carbon concentrations in the urban atmosphere, *J.*
1472 *Air & Waste Manage. Assoc.*, 54:7, 823-833, DOI: 10.1080/10473289.2004.10470957, 2004.
- 1473 Bergstrom, R. W., Russell, P. B., and Hignett, P. B.: The Wavelength Dependence of
1474 Black Carbon Particles: Predictions and Results from the TARFOX experiment and
1475 Implications for the Aerosol Single Scattering Albedo, *J. Atmos. Sci.*, 59, 567–577, 2002.
- 1476 Bergstrom R.W., Pilewskie P., Russell, P. B., Redemann, J., Bond, T. C., Quinn, P. K.,
1477 and Sie, B.: Spectral absorption properties of atmospheric aerosols, *Atmos. Chem. Phys.*, 7,
1478 5937–5943, 2007.
- 1479 Blanchard, C.L., Tanenbaum, S., and Lawson, D.R.: Differences between weekday and
1480 weekend air pollution levels in Atlanta; Baltimore; Chicago; Dallas-Fort Worth; Denver;
1481 Houston; New York; Phoenix; Washington,DC; and surrounding areas, *J. Air & Waste*
1482 *Manage. Assoc.* 58, 1598–1615, DOI:10.3155/1047-3289.58.12.1598, 2008.
- 1483 Bond, T. C., Anderson, T. L., and Campbell, D.: Calibration and inter-comparison of filter-
1484 based measurements of visible light absorption by aerosols, *Aerosol Sci. Technol.*, 30,
1485 582-600, doi 10.1080/027868299304435, 1999.
- 1486 Buzcu-Guven, B., Brown, S.G., Frankel, A., Hafner, H.J., and Roberts P.T.: Analysis and
1487 apportionment of organic carbon and fine particulate matter sources at multiple sites in the
1488 midwestern United States, *J. Air Waste Manage. Assoc.*, 57, 606– 619, 2007.
- 1489 Carslaw, D.C. “The openair manual — open-source tools for analysing air pollution

1490 data,” Manual version 1.1-4, King’s College London, 2015.

1491 Carslaw, D.C. and K. Ropkins, “openair — an R package for air quality data analysis,”
1492 Environmental Modelling & Software, vol 27-28, pp. 52–61, 2012.

1493 Cazorla, A., Bahadur, R., Suski, K.J., Cahill, J.F., Chand, D., Schmid, B., Ramanathan,
1494 V., and Prather, K.A.: Relating aerosol absorption due to soot, organic carbon, and dust to
1495 emission sources determined from in-situ chemical measurements, Atmos. Chem. Phys., 13,
1496 9337–9350, doi:10.5194/acp-13-9337-2013, 2013.

1497 Chan, T. W., Huang, L., Leaitch, W. R., Sharma, S., Brook, J. R., Slowik, J. G., Abbatt, J. P.,
1498 Brickell, P. C., Liggió, J., Li, S.-M., and Moosmüller, H.: Observations of OM/OC and specific
1499 attenuation coefficients (SAC) in ambient fine PM at a rural site in central Ontario, Canada,
1500 Atmos. Chem. Phys., 10, 2393-2411, doi:10.5194/acp-10-2393-2010, 2010.

1501 Clarke, A., McNaughton C., Kapustin, V., Shinozuka, V., Howell, S., Dibb, J., Zhou, J.,
1502 Anderson, B., Brekhovskikh, V., Turner, H., and Pinkerton, M.: Biomass burning and pollution
1503 aerosol over North America: Organic components and their influence on spectral optical
1504 properties and humidification response, J. Geophys Res., 112, D12S18,
1505 doi:10.1029/2006JD007777, 2007.

1506 Collaud Coen, M., Weingartner, E., Nyeki, S., Cozic, J., Henning, S., Verheggen, B., Gehrig,
1507 R., and Baltensperger, U.: Long-term trend analysis of aerosol variables at the high-alpine site
1508 Jungfraujoch, J. Geophys. Res., 112, D13213, doi:10.1029/2006JD007995, 2007.

1509 Collaud Coen M., Andrews, E., Asmi, A., Baltensperger, U., Bukowiecki, N., Day, D., Fiebig,
1510 M., Fjaeraa, A.M., Flentje, H., Hyvärinen, A., Jefferson, A., Jennings, S.G., Kouvarakis, G.,
1511 Lihavainen, H., Lund Myhre, C., Malm, W.C., Mihapopoulos, N., Molenaar, J.V., O’Dowd,
1512 C., Ogren, J.A., Schichtel, B.A., Sheridan, P., Virkkula, A., Weingartner, E., Weller, R., and
1513 Laj, P.: Aerosol decadal trends – Part 1: In-situ optical measurements at GAW and
1514 IMPROVE stations, Atmos. Chem. Phys., 13, 869–894, doi:10.5194/acp-13-869-2013, 2013.

1515 Costabile, F., Barnaba, F., Angelini, F., and G. P. Gobbi, G.P.: Identification of key aerosol
1516 populations through their size and composition resolved spectral scattering and
1517 absorption, Atmos. Chem. Phys., 13, 2455-2470, doi:10.5194/acp-13-2455-2013, 2013.

1518 Delene, D. J., and Ogren, J. A.: Variability of aerosol optical properties at four North

- 1519 American surface monitoring sites, *J. Atmos. Sci.*, 59, 1135-1150, 2002.
- 1520 Dubovik, O., Smirnov, A., Holben, B. N., King, M. D., Kaufman, Y. J., Eck, T. F., and
1521 Slutsker, I.: Accuracy assessments of aerosol optical properties retrieved from Aerosol
1522 Robotic Network (AERONET) Sun and sky radiance measurements, *J. Geophys. Res.*, 105,
1523 9791–9806, 2000.
- 1524 Dubovik, O., Holben, B., Eck, T.F., Smirnov, A., Kaufman, Y.J., King, M.D., Tanre, D., and
1525 Slutsker, I.: Variability of absorption and optical properties of key aerosol types
1526 observed in worldwide locations, *J. Atmos. Sci.*, 59, 590-607, 2005
- 1527 Goldstein, A.H., Koven, C.D., Heald, C.L., and Fung, I.Y.: Biogenic carbon and
1528 anthropogenic pollutants combine to form a cooling haze over the southeastern United
1529 States. *P. Natl. Acad. Sci. USA*, 106, 8835-8840, doi:10.1073/pnas.0904128106, 2009.
- 1530 Guenther, A., Karl, T., Harley, P., Wiedinmyer, C., Palmer, P.I., and Geron, C.: Estimates
1531 of global terrestrial isoprene emissions using MEGAN (Model of Emissions of Gases and
1532 Aerosols from Nature), *Atmos. Chem. Phys.*, 6, 3181–3210, 2006.
- 1533 Gyawali, M., Arnott, W. P., Lewis, K., and Moosmuller, H.: In situ aerosol optics in Reno,
1534 NV, USA during and after the summer 2008 California wildfires and the influence of
1535 absorbing and non- absorbing organic coatings on spectral light absorption, *Atmos. Chem.*
1536 *Phys*, 9, 8007–8015, 2009.
- 1537 Hand, J.L., Schichtel, B. A., Malm, W. C., and Pitchford, M. L.: Particulate sulfate ion
1538 concentration and SO₂ emission trends in the United States from the early 1990s through 2010,
1539 *Atmos. Chem. Phys.*, 12, 10353–10365, doi:10.5194/acp-12-10353-2012, 2012a.
- 1540 Hand, J.L., Schichtel, B.A., Pitchford, M. L., Malm, W. C., and Frank, N.H.: Seasonal
1541 composition of remote and urban fine particulate matter in the United States, *J. Geophys.*
1542 *Res.*, 117, D05209, doi:10.1029/2011JD017122, 2012b.
- 1543 Hand, J.L., Schichtel, B.A., Pitchford, M. L., Malm, W. C., and Frank, N.H.: Spatial and
1544 temporal trends in PM_{2.5} organic and elemental carbon across the United States, *Advances*
1545 *in Meteorology*, 2003, 367674, <http://dx.doi.org/10.1155/2013/367674>, 2013.
- 1546 Hand, J.L, Schichtel, B.A., Malm, W.C., Copeland, S., Molenaar, J.V., Frank, N., and
1547 Pitchford, M.: Widespread reductions in haze across the United States from the early

1548 1990s through 2011, *Atmos. Environ.*, 94, 671-679, doi: 10.1016/j.atmosenv.2014.05.062,
1549 2014.

1550 \Haywood, J. M., and Shine, K. P.: The effect of anthropogenic sulfate and soot aerosol on
1551 the clear sky planetary radiation budget, *Geophys. Res. Lett.*, 22, 5, 603-606,
1552 doi:10.1029/95GL00075, 1995.

1553 Hidy, G.M., Blanchard, C.L., Baumann, K., Edgerton, E., Tanenbaum, S., Shaw, S.,
1554 Knipping, E., Tombach, I., Jansen, J., and J. Walters.: Chemical climatology of the
1555 southeastern United States, 1999-2013, *Atmos. Chem. Phys.*, 14, 11893-11914, 2014.

1556 Holzworth, G.C.: Estimates of mean maximum mixing depths in the contiguous United
1557 States, *Mon. Weather. Rev.*, 92 235-242, 1964.

1558 Kahn, R. A., Yu, H., Schwartz, S.E., Chin, M., Feingold, G., Remer, L.A., Rind, D., Halthore,
1559 R., and DeCola, P.: Introduction, in *Atmospheric Aerosol Properties and Climate Impacts,*
1560 *A Report by the US Climate Change Science Program and the Subcommittee on Global*
1561 *Change Research.* [Mian Chin, Ralph A. Kahn, and Stephen E. Schwartz (eds.)], National
1562 Aeronautics and Space Administration, Washington, D.C., USA, 2009.

1563 Koloutsou-Vakakis, S., Carrico, C.M., Kus, P., Rood, M.J., Li, Z., Shrestha, R., Ogren,
1564 J.A., Chow, J.C., and Watson, J.G.: Aerosol properties at a midlatitude Northern
1565 Hemisphere continental site, *J. Geophys. Res.*, 106, D3, 3019-3032,
1566 doi:10.1029/2000JD900126, 2001.

1567 Lack, D.A., Cappa, C.D., Covert, D.S., Baynard, T., Massoli, P., Sierau, B., Bates, T.S.,
1568 Quinn, P.K., Lovejoy, E.R., and Ravishankara, A. R.: Bias in Filter-Based Aerosol Light
1569 Absorption Measurements Due to Organic Aerosol Loading: Evidence from Ambient
1570 Measurements, *Aerosol Sci. Technol*, 42, 1033–1041, doi: 10.1080/02786820802389277,
1571 2008.

1572 Lack, D.A., Cappa, C.D., Cross, E.S., Massoli, P., Ahern, A.T., Davidovits, P., and
1573 Onasch, T.B.: Absorption Enhancement of Coated Absorbing Aerosols: Validation of the
1574 Photo-Acoustic Technique for Measuring the Enhancement, *Aerosol Sci. Technol*, 43,10,
1575 1006-1012, doi: 10.1080/02786820903117932, 2009.

1576 Leaitch, W.R., Macdonald, A.M., Brickell, P.C., Liggio, J., Siostedt, S.L., Vlasenko, A.,

1577 Bottenheim, J.W., Huang, L., Li, S., Liu, S.K., Toom-Sauntry, D., Hayden, K.A., Sharma, S.,
1578 Shantz, N.C., Wiebe, H.A., Zhang, W., Abbatt, J., Slowik, J.G., Chang, R., Russell,
1579 L.M., Schwartz, R.E., Takahama, S., Jayne, J.T., and Ng, N.: Temperature response of the
1580 submicron organic aerosol from temperate forests, *Atm. Env.*, 45, 6696-6704, 2011.

1581 Levy, R.C., Remer, L. A., Kleidman, R. G., Mattoo, S., Ichoku, C., Kahn, R., and Eck, T.
1582 F.: Global evaluation of the Collection 5 MODIS dark-target aerosol products over land,
1583 *Atmos. Chem. Phys.*, 10, 10399–10420, doi:10.5194/acp-10-10399-2010, 2010.

1584 Li, J., Carlson, B.E., Dubovik, O., and Lacis, A.A.: Recent trends in aerosol optical
1585 properties derived from AERONET measurements, *Atmos. Chem. Phys. Discuss.*, 14,
1586 14351-14397, doi:10.5194/acpd-14-14351-2014, 2014.

1587 Liggió, J., Li, S., Vlasenko, A., Siostedt, S.L., Chang, R., Shantz, N., Abbatt, J., Slowik,
1588 J.G., Bottenheim, J.W., Brickell, P.C., Stroud, C., and Leitch, R.R.: Primary and secondary
1589 organic aerosols in urban air masses intercepted at a rural site, *J. Geophys. Res.*, 115,
1590 D21305, doi: 12010JD0144260.1029/, 2010.

1591 Link, M.F., Zhou, Y., Taubman, B.F., Sherman, J.P., Sive, B.C., Morrow, H., Krintz, I.,
1592 Robertson, L., Cook, R., Stocks, J., and West, M.: A characterization of volatile organic
1593 compounds and secondary organic aerosol at a mountain site in the southeastern United
1594 States Estimating background secondary organic aerosol in the southeastern United
1595 States from a regionally representative site, *J. Atmos. Chem.*, doi: 10.1007/s10874-015-9305-
1596 5, 2015.

1597 Malm, W.C., Schichtel, B.A., Pitchford, M.L., Ashbaugh, L.L., and Eldred, R.A.: Spatial and
1598 monthly trends in speciated fine particle concentration in the United States. *J. Geophys.*
1599 *Res.*, 109, D03306, doi: 10.1029/2003JD003739, 2004.

1600 Müller, T., Henzing, J.S., de Leeuw, G., Wiedensohler, A., Alastuey, A., Angelov, H.,
1601 Bizjak, M., Collaud Coen, M., Engstrom, J. E. Gruening, C., Hillamo, R., Hoffer, A.,
1602 Imre, K., Ivanow, P., Jennings, G., Sun, J.Y., Kalivitis, N., Karlsson, H., Komppula, M.,
1603 Laj, P., Li, S-M., Lunder, C., Marinoni, A., Martins dos Santos, S., Moerman, M.,
1604 Nowak, A., Ogren, J.A., Petzold, A., Pichon, J.M., Rodriguez, S., Sharma, S., Sheridan,
1605 P.J., Teinila, K., Tuch, T., Viana, M., Virkkula, A., Weingartner, E., Wilhelm, R., and
1606 Wang, Y.Q.: Characterization and inter-comparison of aerosol absorption photometers:

1607 result of two inter-comparison workshops, *Atmos. Meas. Tech.*, 4, 245–268, 2011.

1608 Murphy, D.M., Capps, S. L., Daniel, J. S., Frost, G. J., and White, W. H.: Weekly patterns
1609 of aerosol in the United States, *Atmos. Chem. Phys.*, 8, 2729–2739, doi:10.5194/acp-8-
1610 2729-2008, 2008.

1611 Murphy, D.M., Chow, J.C., Leibensperger, E.M., Malm, W.C., Pitchford, M., Schichtel,
1612 B.A., Watson, J.G., and White, W.H.: Decreases in elemental carbon and fine particle
1613 mass in the United States, *Atmos. Chem. Phys.*, 11, 4679–4686, doi:10.5194/acp-11-4679-
1614 2011, 2011.

1615 Ogren, J. A.: Comment on "Calibration and Intercomparison of Filter-Based Measurements
1616 of Visible Light Absorption by Aerosols", *Aerosol Sci. Technol.*, 44, 589-591,
1617 doi:10.1080/02786826.2010.482111, 2010.

1618 Ogren, J.A., Wendell, J. Sheridan, P.J., Hageman, D., and Jefferson, A.: Continuous
1619 light absorption photometer performance, ASR Science Team Meeting, Potomac, Md,
1620 USA, March 18-21, 2013, available at
1621 <http://asr.science.energy.gov/meetings/stm/posters/view?id=781>, last access: 26 October
1622 2014.

1623 Parworth C., Fast, J, Mei, F., Shippert, T., Sivaraman, C., Tilp, A., Watson, T., and Zhang,
1624 Q.: Long- term measurements of sub-micrometer aerosol chemistry at the Southern Great
1625 Plains (SGP) using an aerosol chemical speciation monitor (ACSM), *Atm. Env.*, 106, 43-55,
1626 2015.

1627 Quinn, P. K., Bates, T. S., Baynard, T., Clarke, A. D., Onasch, T. B., Wang, W., Rood, M.,
1628 Andrews, E., Allan, J., Carrico, C. M., Coffman, D., and Worsnop, D.: Impact of
1629 particulate organic matter on the relative humidity dependence of light scattering: A
1630 simplified parameterization, *Geophys. Res. Lett.*, 32(L22809), doi:101029/2005GL024322,
1631 2005.

1632 Rupakheti, M., Leaitch, R., Lohmann, U., Hayden, K., Brickell, P., Lu, G., Li, S.,
1633 Toom-Saunty D., Bottenheim, J.W., Brook, J.R., Vet, R., Jayne, J.T., and Worsnop,
1634 D.R.: An Intensive Study of the Size and Composition of Submicron Atmospheric Aerosols
1635 at a Rural Site in Ontario, Canada, *Aerosol Science and Technology*, 39:8, 722-736,
1636 DOI: 10.1080/02786820500182420, 2005.

1637 Schuster, G.L., Dubovik, O., and Holben, B.N.: Angstrom exponent and bimodal aerosol size
1638 distributions, *J. Geophys. Res.*, 111, D07207, doi:10.1029/2005JD006328, 2006.

1639 Seinfeld, J. H. and Pandis, S. N.: Atmospheric chemistry and physics: from air pollution to
1640 climate change, 2nd edition, John Wiley & Sons, New York, New York, USA, 1998.

1641 Sheridan, P. J., and Ogren, J. A.: Observations of the vertical and regional variability of aerosol
1642 optical properties over central and eastern North America, *J. Geophys. Res.*, 104, D14, 16793-
1643 16805, doi:10.1029/1999JD900241, 1999.

1644 Sheridan, P. J., Delene, D. J., and Ogren, J. A.: Four years of continuous surface
1645 aerosol measurements from the Department of Energy's Atmospheric Radiation Measurement
1646 Program Southern Great Plains Cloud and Radiation Testbed site, *J. Geophys. Res.*,
1647 106, D18, 20735-20747, doi:10.1029/2001JD000785, 2001.

1648 Sheridan, P. J., Jefferson, A., and Ogren, J. A.: Spatial variability of submicrometer
1649 aerosol radiative properties over the Indian Ocean during INDOEX, *J. Geophys. Res.*, 107,
1650 D19, 8011, doi:10.1029/2000JD000166, 2002.

1651 Sheridan, P. J., Andrews, E., Ogren, J. A., Tackett, J. L., and Winker, D. M.: Vertical
1652 profiles of aerosol optical properties over central Illinois and comparison with surface and
1653 satellite measurements, *Atmos. Chem. Phys.*, 12, 11695–11721, doi:10.5194/acp-12-11695-
1654 2012, 2012.

1655 Slowik, J. G., Stroud, C., Bottenheim, J. W., Brickell, P. C., Chang, R. Y.-W., Liggio, J.,
1656 Makar, P. A., Martin, R. V., Moran, M. D., Shantz, N. C., Sjostedt, S. J., van Donkelaar, A.,
1657 Vlasenko, A., Wiebe, H. A., Xia, A. G., Zhang, J., Leaitch, W. R., and Abbatt, J. P. D.:
1658 Characterization of a large biogenic secondary organic aerosol event from eastern
1659 Canadian forests, *Atmos. Chem. Phys.*, 10, 2825–2845, doi:10.5194/acp-10-2825-2010,
1660 2010.

1661 Spak, S.N and Holloway, T.: Seasonality of speciated aerosol transport over the Great Lakes
1662 region, *J. Geophys. Res.*, 114, D08302, doi:10.1029/2008JD010598, 2009.

1663 US Census Bureau. 2010. 2006–2010 American Community Survey. Available at
1664 <http://www.census.gov/acs/www/>, Accessed January 3, 2012.

1665 van de Hulst, H.C.: Light scattering by small particles, John Wiley and Sons, New York, 1957.

1666 Wiscombe, W. J. and Grams, G. W.: The backscattered fraction in two-stream approximations,
1667 J. Atmos. Sciences, 33, 2440-2451, 1976.

1668 WMO: WMO/GAW Aerosol Measurement procedures guidelines and recommendations.
1669 World Meteorological Organization, Technical Document No. 1178, GAW Report No. 153,
1670 2003.

1671 Yang, F., Huang, L., Sharma, S., Brook, J.R., Zhang, W., Li, S., and Tan, J.: Two-year
1672 observations of fine carbonaceous particles in variable sampling intervals, *Atm. Env.*, 45,
1673 2418-2426, 2011.

1674 Yoon, J., von Hoyningen-Huene, W., Kokhanovsky, A.A., Vountas M., and Burrows.
1675 J.P.: Trend analysis of aerosol optical thickness and Ångström exponent derived from
1676 the global AERONET spectral observations, *Atmos. Meas. Tech.*, 5, 1271–1299,
1677 doi:10.5194/amt-5-1271-2012, 2012.

1678 Yu, H., Kaufman, Y., Chin, M., Feingold, G., Remer, L., Anderson, T., Balkanski, Y.,
1679 Bellouin, N., Boucher, O., Christopher, S., DeCola, P., Kahn, R., Koch, D., Loeb, N.,
1680 Reddy, M. S., Schulz, M., Takemura, T., and Zhou, M.: A review of measurement-based
1681 assessments of aerosol direct radiative effect and forcing, *Atmos. Chem. Phys.*, 6, 613-666.
1682 2006.

1683 Yu, H., Quinn, P.K., Feingold, G., Remer, L.A., Kahn, R.A., Chin, M., and Schwartz,
1684 S.E.: Remote Sensing and *In Situ* Measurements of Aerosol Properties, Burdens, and
1685 Radiative Forcing, in *Atmospheric Aerosol Properties and Climate Impacts*, A Report by the
1686 US Climate Change Science Program and the Subcommittee on Global Change Research.
1687 [Mian Chin, Ralph A. Kahn, and Stephen E. Schwartz (eds.)], National Aeronautics and
1688 Space Administration, Washington, D.C., USA, 2009.

1689 Zhang, X., Hecobian, A., Zheng, M., Frank, N. H., and Weber, R. J.: Biomass burning
1690 impact on PM_{2.5} over the southeastern US during 2007: integrating chemically
1691 speciated FRM filter measurements, MODIS fire counts and PMF analysis, *Atmos. Chem.*
1692 *Phys.*, 10, 6839–6853, doi:10.5194/acp-10-6839-2010, 2010.

1693

Table 1. Sites, instruments and data period included in the study, listed from west to east. Aerosol sampling size cuts and the instrument used to measure absorption is also included. All sites used a TSI 3563 3- λ nephelometer¹ to measure total scattering and hemispheric backscattering

Site	Lat/Long (deg)	Elev.(m) asl	Yrs data used	# Hrs used 2010-2013	Size cut (μm)	Absorption instrument (dates used mm/yy)
SGP	36.6N, 97.5W	315	1997- 2013 ⁵	32,971(σ_{sp}) 25,140(σ_{ap})	1,10	3- λ PSAP ³ (1/10-12/13)
BND	40.0N, 88.4W	230	1996- 2013	33,449(σ_{sp}) 32,040(σ_{ap})	1,10	1- λ PSAP ² (9/96-2/06) 3- λ PSAP (3/06-2/12) 3- λ CLAP ⁴ (3/12-12/13)
EGB	44.2N, 79.8W	253	2010- 2013	32,448(σ_{sp}) 26,304(σ_{ap})		1- λ PSAP (1/10-12/13)
APP	36.2N, 81.7W	1080	2010- 2013	34,220(σ_{sp}) 34,178(σ_{ap})	1,10	3- λ PSAP (1/10-12/13)

¹3- λ TSI nephelometer measures at $\lambda=450, 550, 700$ nm; ²1- λ PSAP measures at 565 nm, adjusted to 550 nm using Bond et al. (1999) correction; ³3- λ PSAP measures at 467, 530, 660 nm; ⁴3- λ CLAP measures at 467, 529, 653 nm; ⁵SGP aerosol light scattering data from 1997-2013 is used but absorption data is only used from 2010-2013.

Table 2. Parameters and equations used to calculate aerosol optical properties. Constants and parameters used in the formula to calculate globally-averaged top-of-atmosphere direct radiative forcing (DRFE) for each site are also included and are denoted with **.

Parameter	Equation (or value)
Extinction Coefficient	$\sigma_{ep} = \sigma_{sp} + \sigma_{ap}$
Single-scattering albedo	$\omega_0 = \sigma_{sp} / \sigma_{ep} = \sigma_{sp} / (\sigma_{sp} + \sigma_{ap})$
Hemispheric backscatter fraction	$b = \sigma_{bsp} / \sigma_{sp}$
Scattering Ångström exponent	$\alpha_{sp} = -\log(\sigma_{sp}(\lambda_1) / \sigma_{sp}(\lambda_2)) / \log(\lambda_1 / \lambda_2)$
Absorption Ångström exponent	$\alpha_{ap} = -\log(\sigma_{ap}(\lambda_1) / \sigma_{ap}(\lambda_2)) / \log(\lambda_1 / \lambda_2)$
Sub-micron scattering fraction	$R_{sp} = \sigma_{sp,1} / \sigma_{sp,10}$
Sub-micron absorption fraction	$R_{ap} = \sigma_{ap,1} / \sigma_{ap,10}$
Direct Radiative Forcing Efficiency	$DRFE = DRF / AOD = -D S_0 T_{atm}^2 (1 - A_c) \beta \omega_0 * [(1 - R_s)^2 - (2 R_s / \omega_0 \beta) (1 - \omega_0)]$
Upscatter Fraction**	$\beta = 0.0817 + 1.8495 * b - 2.9682 * b^2$
Fractional Day Length**	$D = 0.50$ (globally-averaged)
Solar Constant**	$S_0 = 1370 \text{ W m}^{-2}$
Atmospheric Transmission**	$T_{atm} = 0.76$ (globally-averaged)
Cloud Fraction**	$A_c = 0.60$ (globally-averaged)
Spectrally-averaged surface albedo**	$R_s = 0.15$ (globally-averaged)

Table 3. Total and precision fractional uncertainties (%) of measured aerosol optical properties (AOPs) σ_{sp} , σ_{bsp} , and σ_{ap} and calculated AOPs (e.g., the intensive AOPs) for 1-hour averaging time. Uncertainties are expressed as 95% confidence intervals. All calculated uncertainties are for $\lambda=550$ nm except for α_{sp} and α_{ap} , which are calculated for the 450/700 nm wavelength pair. All AOPs are PM1 except for PM10 α_{sp} and the PM1 scattering and absorption fractions (R_{sp} and R_{ap} , respectively). The uncertainties in columns 3 and 4 differ only by inclusion of the PSAP unit-to-unit variability term (Eq. S3) in column 3. All uncertainties except $\Delta\sigma_{sp}$, $\Delta\sigma_{bsp}$, and $\Delta\sigma_{ap}$ depend nonlinearly on the measured value, and cannot rigorously be represented as a percentage¹. For these intensive AOP uncertainties, we use approximate annual-mean values $\sigma_{sp,10}=30$ Mm⁻¹, $\sigma_{ap,10}=3.0$ Mm⁻¹, $R_{sp}=0.80$, $R_{ap}=0.88$, $b=0.14$, $\omega_0=0.91$, $\alpha_{sp}=2.0$, and $\alpha_{ap}=1.0$ to calculate fractional uncertainties. The intensive AOP fractional uncertainties apply for the average conditions listed above, and the equations in the Supplementary Materials to this manuscript should be used to calculate uncertainties at different sites or for different conditions.

	Total uncertainty %	Precision uncertainty % for comparisons among sites	Precision uncertainty % for comparisons at single site
$\Delta\sigma_{sp}$	8.0	3.8	3.8
$\Delta\sigma_{bsp}$	8.1	4.0	4.0
$\Delta\sigma_{ap}$	20	20	12
ΔR_{sp}	2.7	1.1	1.1
ΔR_{ap}	4.2	4.2	2.5
Δb	2.3	1.1	1.1
$\Delta \omega_0$	1.5	1.7	0.9
$\Delta \alpha_{sp}$ (PM10)	1.8	1.4	1.4
$\Delta \alpha_{ap}$	17	17	10
$\Delta DRFE$	4.8	5.2	4.8

¹The uncertainties $\Delta\sigma_{sp}$, $\Delta\sigma_{bsp}$, and $\Delta\sigma_{ap}$ depend very weakly on measured values, through the noise term. This term represents a negligible contribution to the uncertainty for averaging times of 1 hour or more.

Table 4. Mann-Kendall slopes (%/decade) and trend significance¹ for long-term trends in several PM10 and PM1 aerosol optical properties measured at BND and SGP. Monthly-averaged data is used for the calculations. BND data for the time period 1996-2013 is used; SGP data for the time period 1997-2013 is used. Trends that are significant at or above the $p < 0.05$ level are in bold.

	BND slope (%/10yr), significance	SGP Slope (%/10yr), significance
$\sigma_{sp,10}$	-16.3, $p < 0.01$	-19.6, $p < 0.001$
$\sigma_{sp,1}$	-23.1, $p < 0.001$	-24.0, $p < 0.001$
$\sigma_{ap,10}$	-15.2, not significant	N/A
$\sigma_{ap,1}$	-10.5, $p < 0.1$	N/A
$\alpha_{sp,10}$	1.9, not significant	-5.3, $p < 0.05$
b_{10}	7.6, $p < 0.001$	11.2, $p < 0.001$
b_1	11.8, $p < 0.001$	15.1, $p < 0.001$
R_{sp}	-8.1, $p < 0.001$	-9.1, $p < 0.001$
$\omega_{0,10}$	-0.5, not significant	N/A
$\omega_{0,1}$	-1.55, $p < 0.01$	N/A

¹Slopes and significance were obtained using the function ‘TheilSen’ in the R package ‘openair’ (Carslaw et al., 2012, Carslaw, 2015). Data were de-seasonalized and autocorrelation was accounted for using options supplied with the TheilSen function. Decadal slopes (%/10year) were calculated by multiplying the yearly slope by 10, i.e., $10 * \% / \text{year}$.

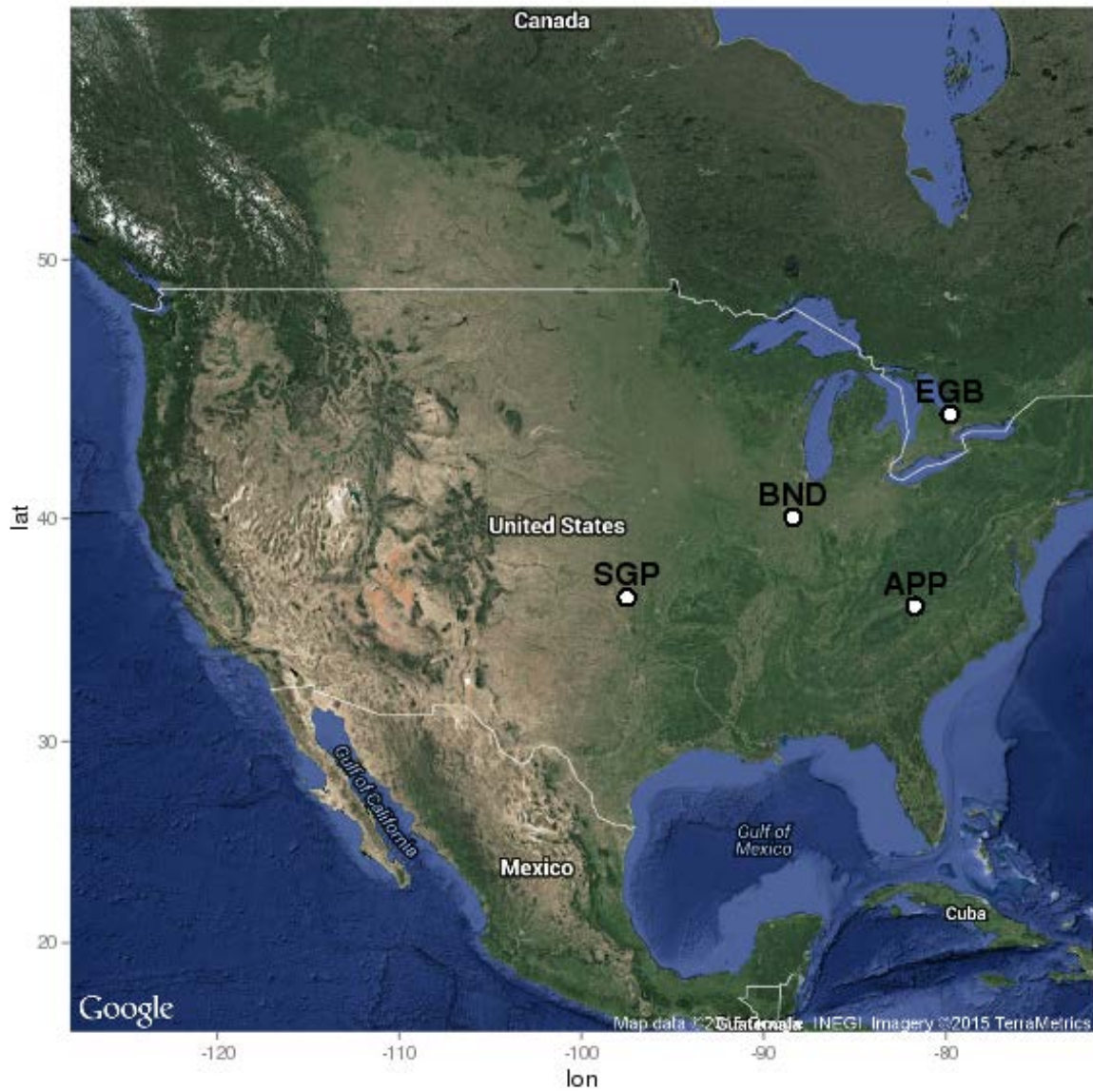


Figure 1. Locations of the four NOAA-ESRL sites in this study- Southern Great Plains, OK (SGP); Bondville, IL (BND); Appalachian State (APP) in Boone, NC; and Egbert, Ontario, Canada (EGB).

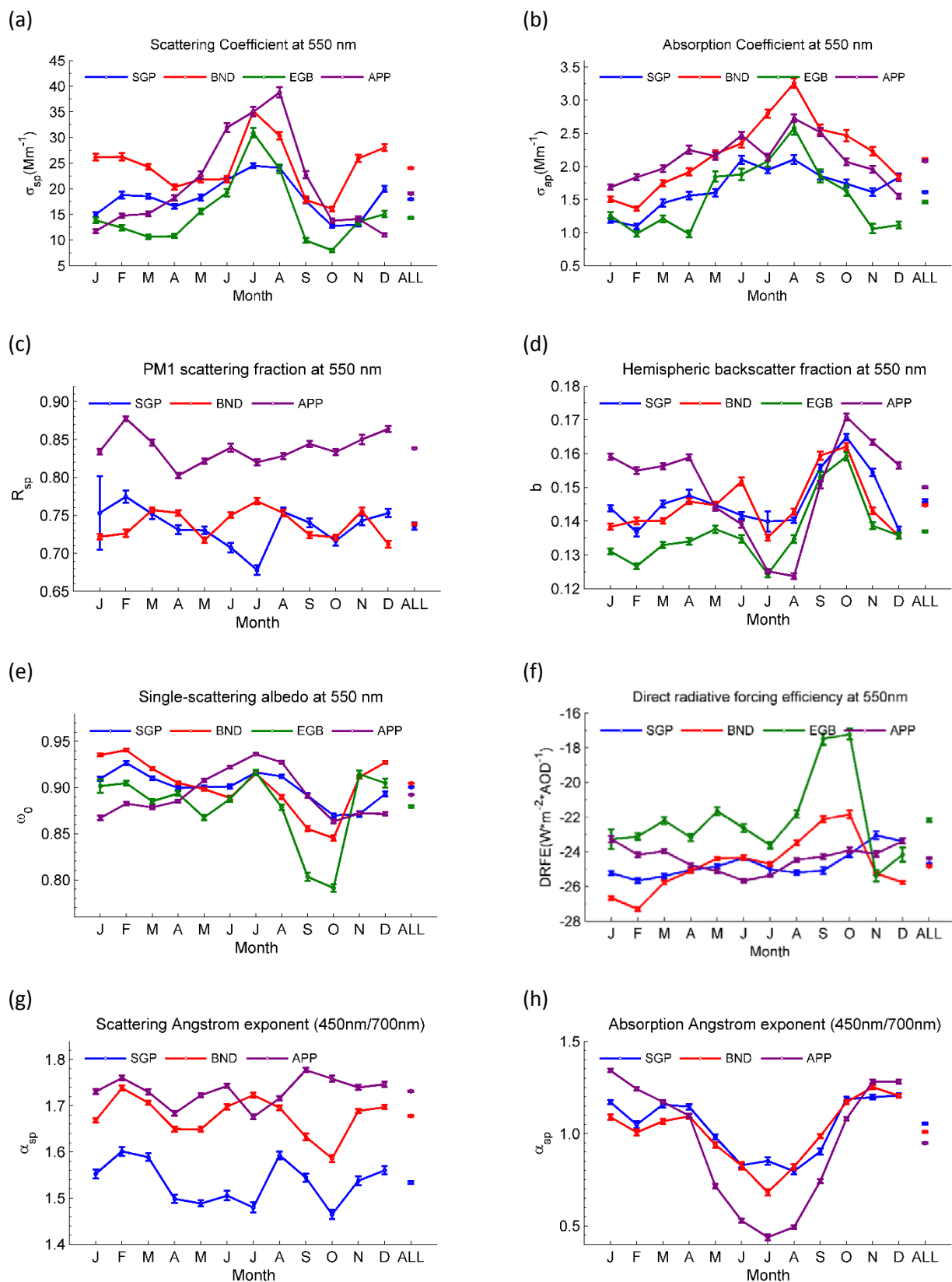


Figure 2. Annual cycle of (a) geometric mean PM1 σ_{sp} ; (b) geometric mean PM1 σ_{ap} ; (c) mean R_{sp} ; (d) mean PM1 b ; (e) mean PM1 ω_0 ; (f) mean PM1 DRFE; (g) mean PM10 α'_{sp} (450/700 nm); and (h) mean PM1 α_{sp} 450/700 nm) at APP, BND, EGB, and SGP over the 2010-2013 period. The values corresponding to 'ALL' are geometric mean or mean values for the entire 2010-2013 period (all months). Error bars represent 95% confidence intervals of the mean values.

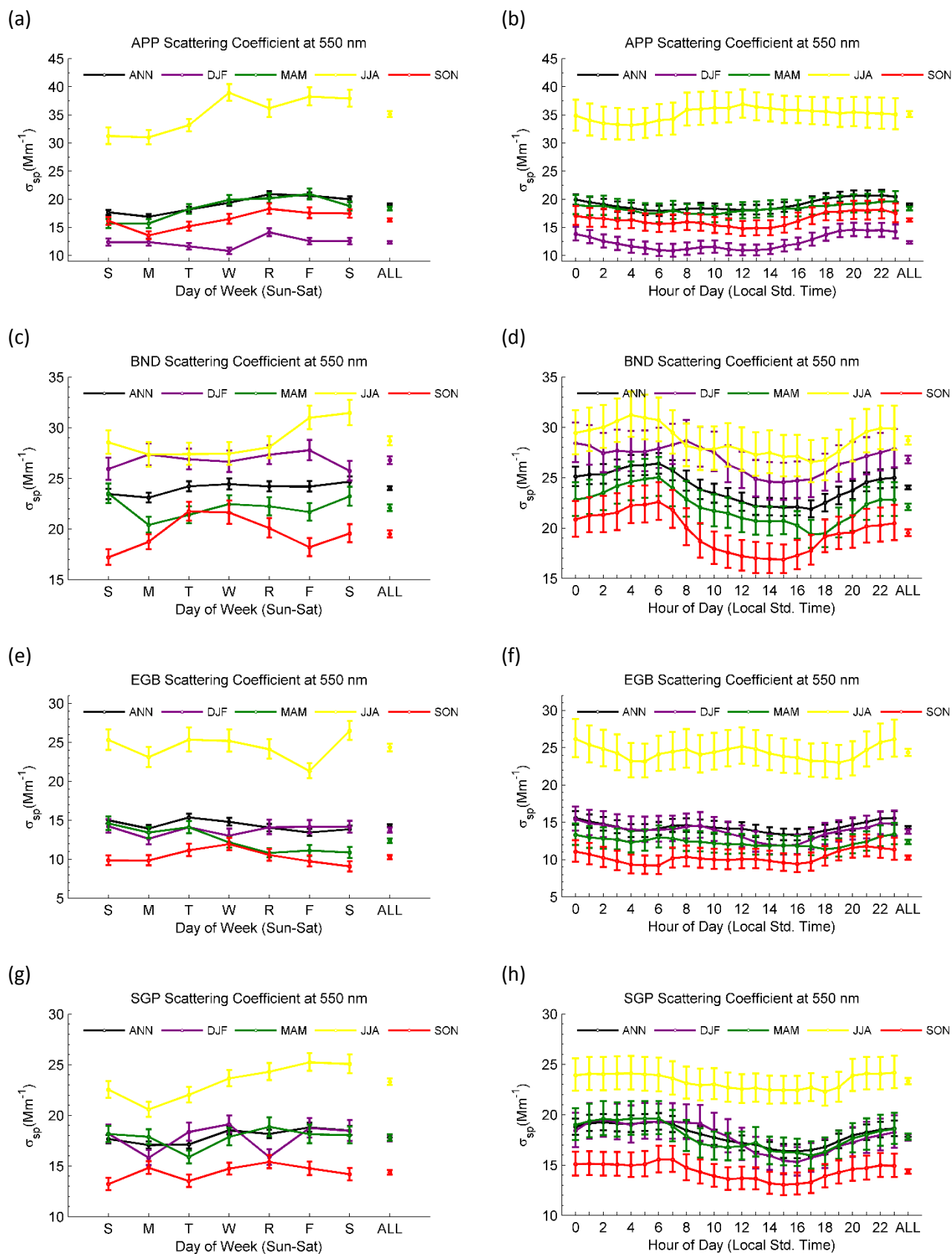


Figure 3. Weekly and diurnal cycles of geometric mean PM1 σ_{sp} over full years (ANN traces) and for winter (DJF), spring (MAM), summer (JJA), and fall (SON) at APP, BND, EGB, and SGP over the 2010-2013 period. The value corresponding to the 'ALL' data point of each trace is the mean value over all days of week or over all hours of day. Error bars represent 95% confidence intervals of mean σ_{sp} values.

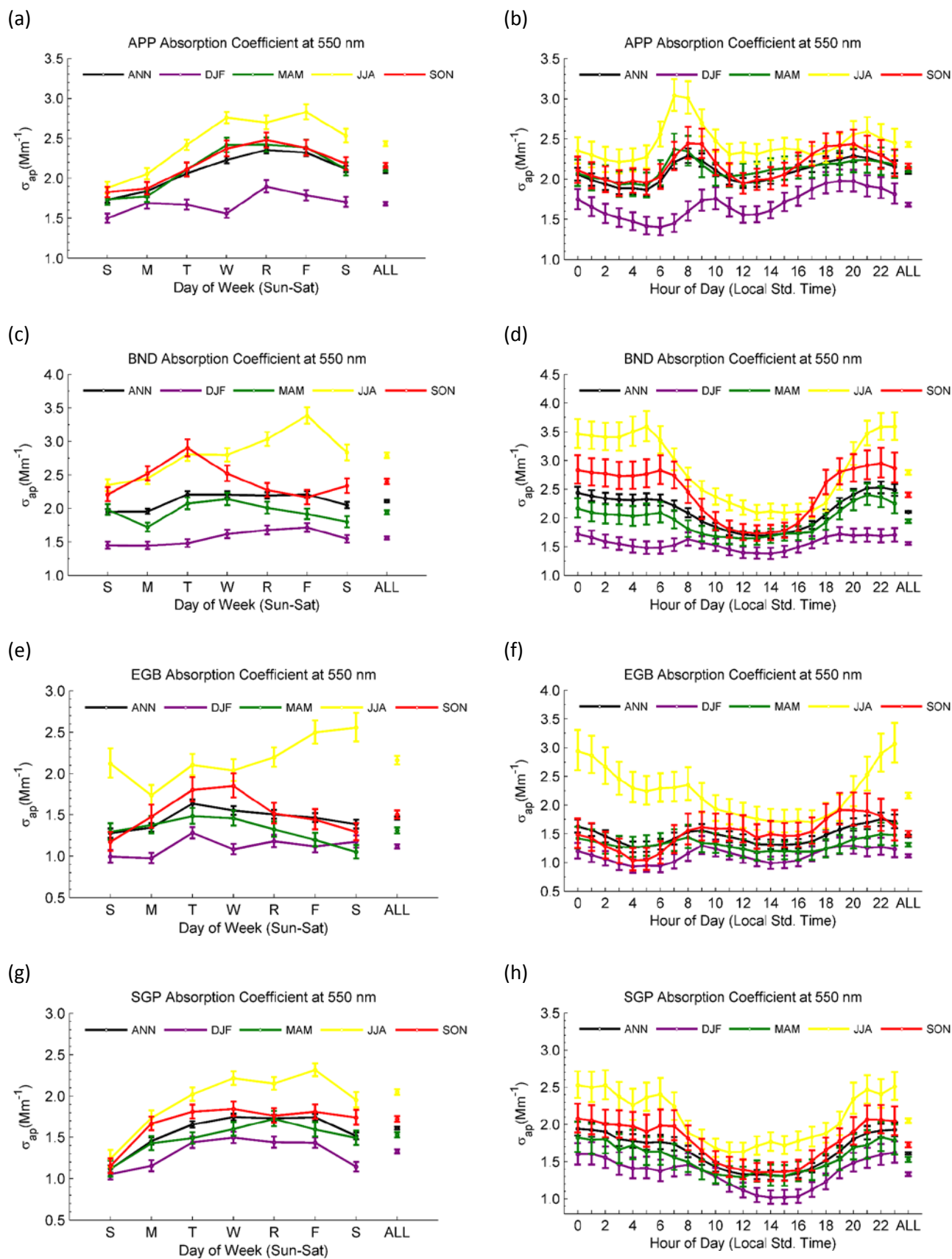
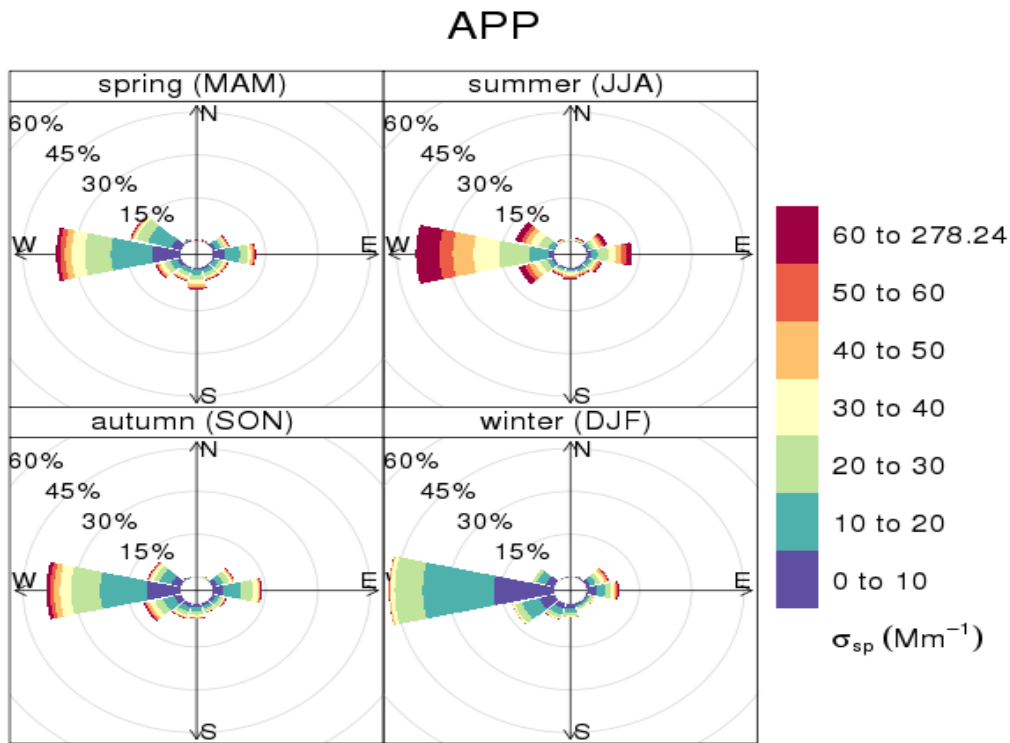


Figure 4. Weekly and diurnal cycles of geometric mean PM1 σ_{ap} over full years (ANN traces) and for individual seasons at APP, BND, EGB, and SGP over the 2010-2013 period. The value corresponding to the 'ALL' data point is the mean value over all days of week or over all hours of day. Error bars represent 95% confidence intervals of the mean values.

(a)



(b)

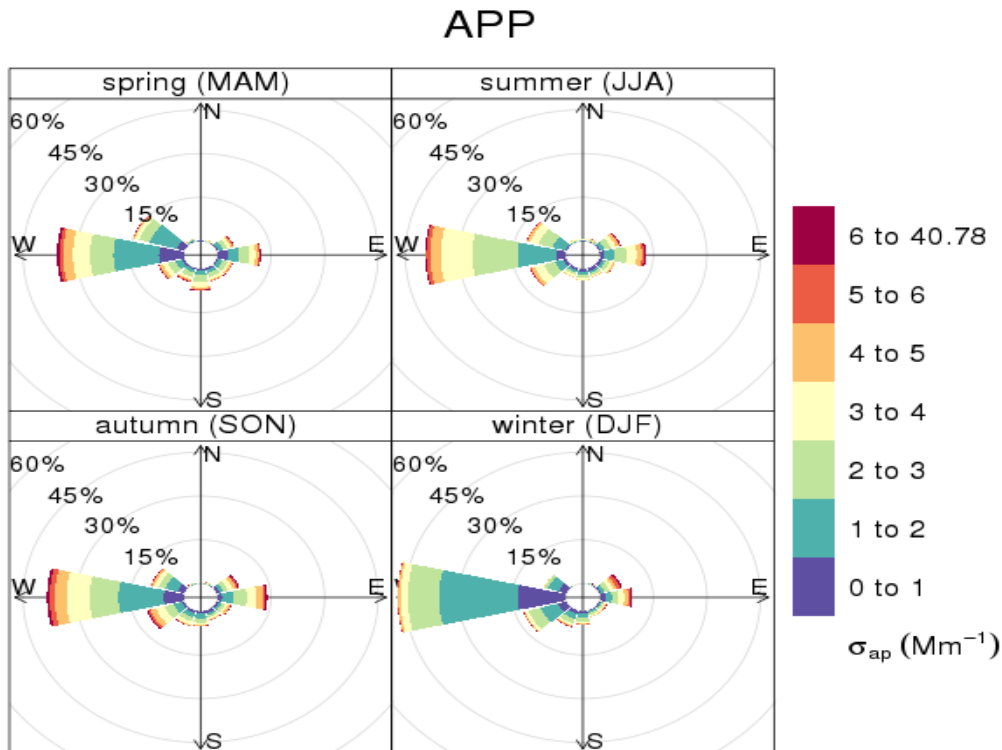
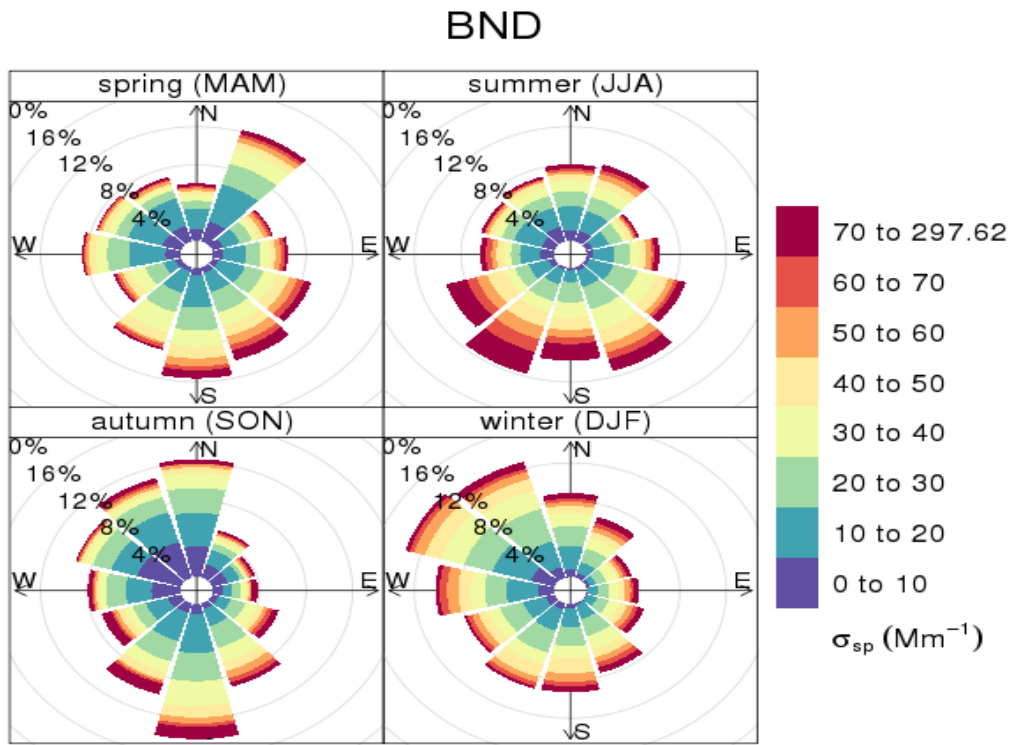


Figure 5. Pollution rose diagrams of σ_{sp} and σ_{ap} for individual seasons at APP over the 2010-2013 period. The percentages at a given radius represent the percentage of hourly profiles for a given wind sector.

(a)



(b)

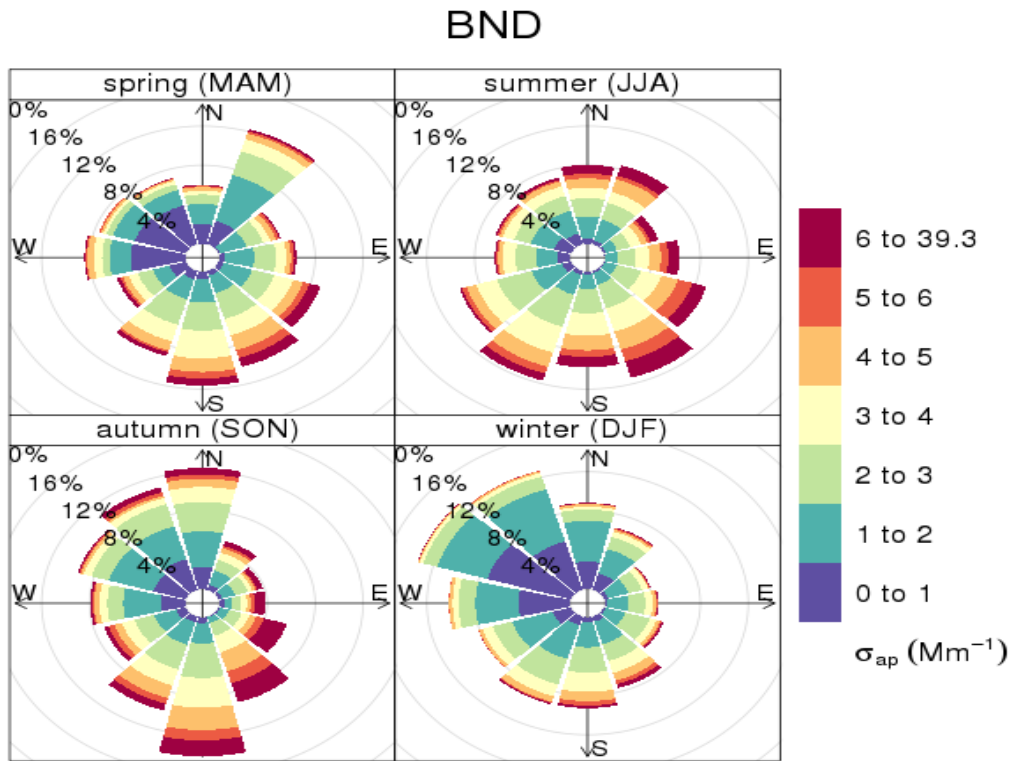
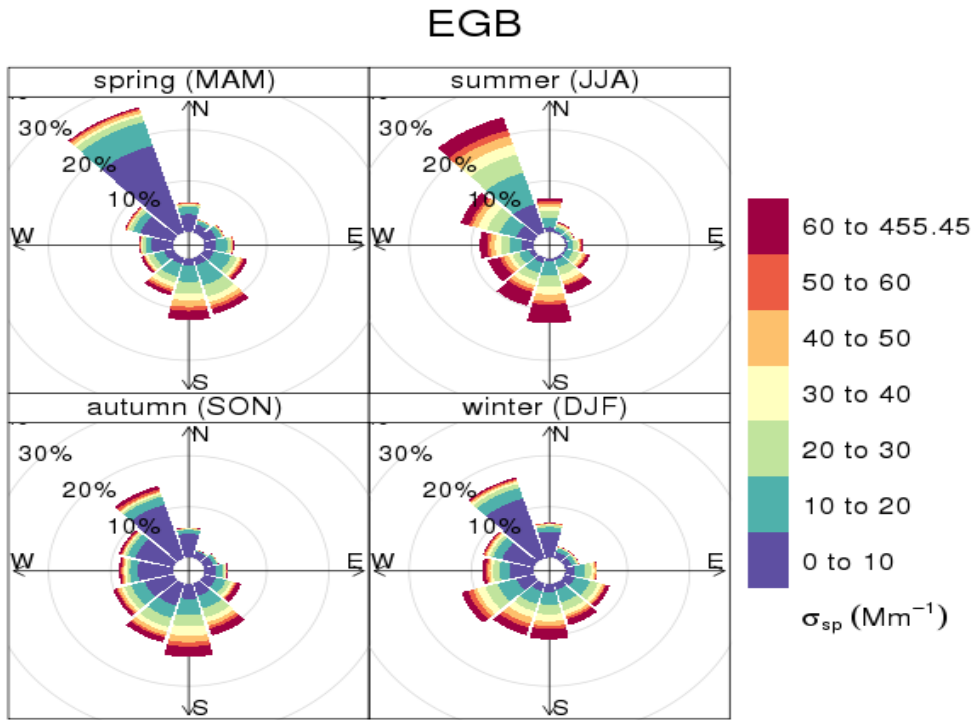


Figure 6. Pollution rose diagrams of σ_{sp} and σ_{ap} for individual seasons at BND over the 2010-2013 period. The percentages at a given radius represent the percentage of hourly profiles for a given wind sector.

(a)



(b)

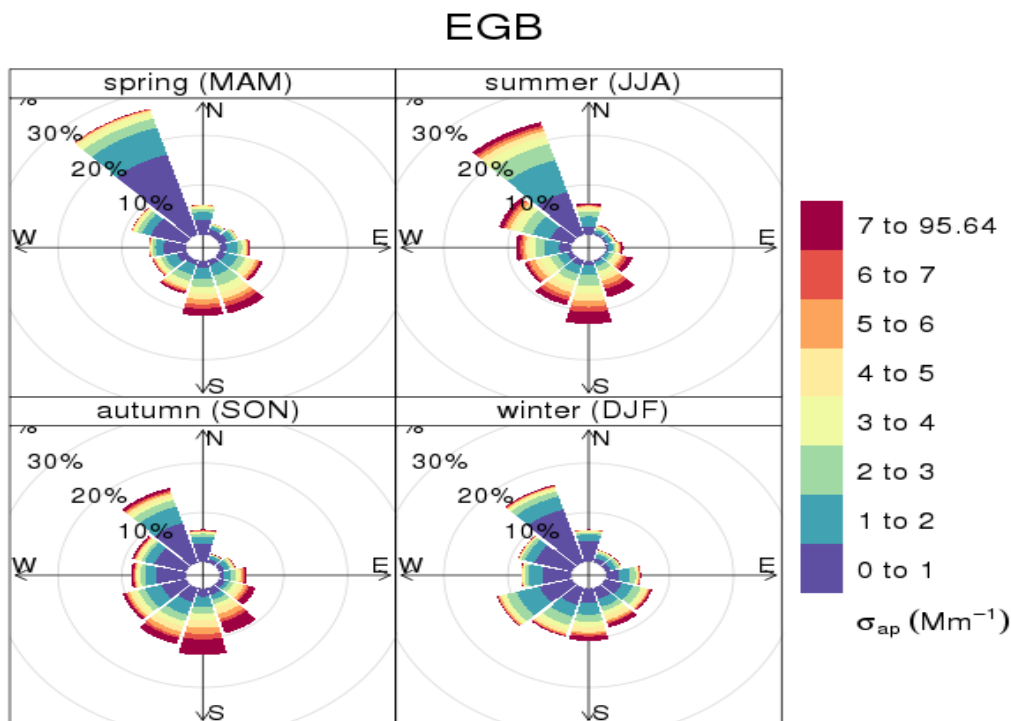
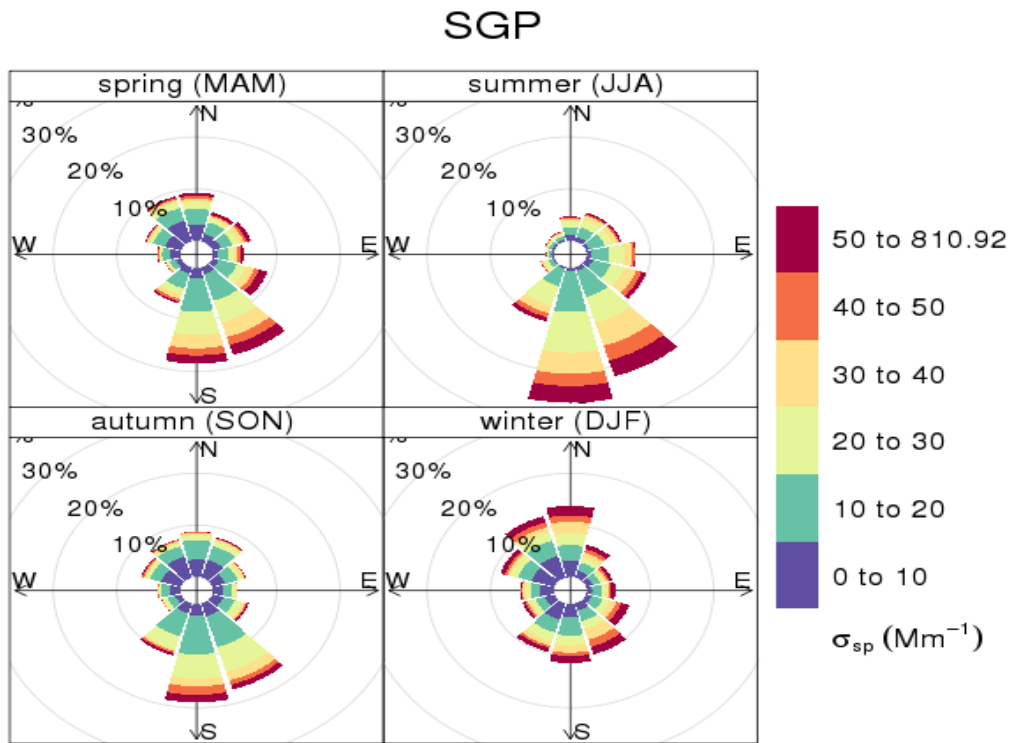


Figure 7. Pollution rose diagrams of σ_{sp} and σ_{ap} for individual seasons at EGB over the 2010-2013 period. The percentages at a given radius represent the percentage of hourly profiles for a given wind sector.

(a)



(b)

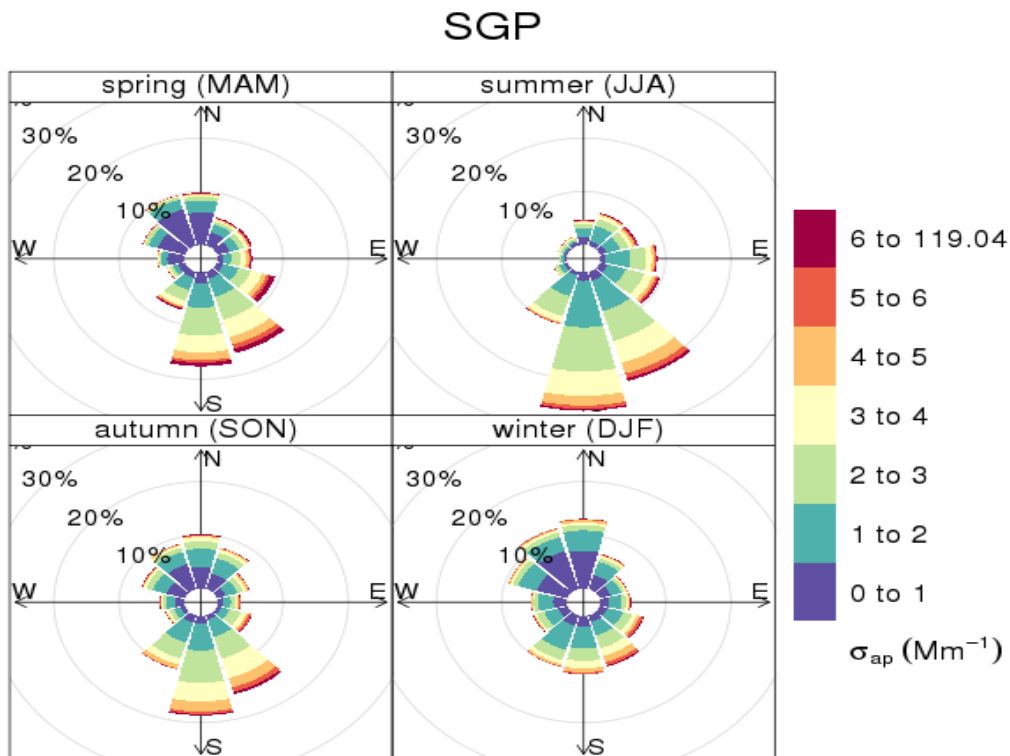


Figure 8. Pollution rose diagrams of σ_{sp} and σ_{ap} for individual seasons at SGP over the 2010-2013 period. The percentages at a given radius represent the percentage of hourly profiles for a given wind sector.

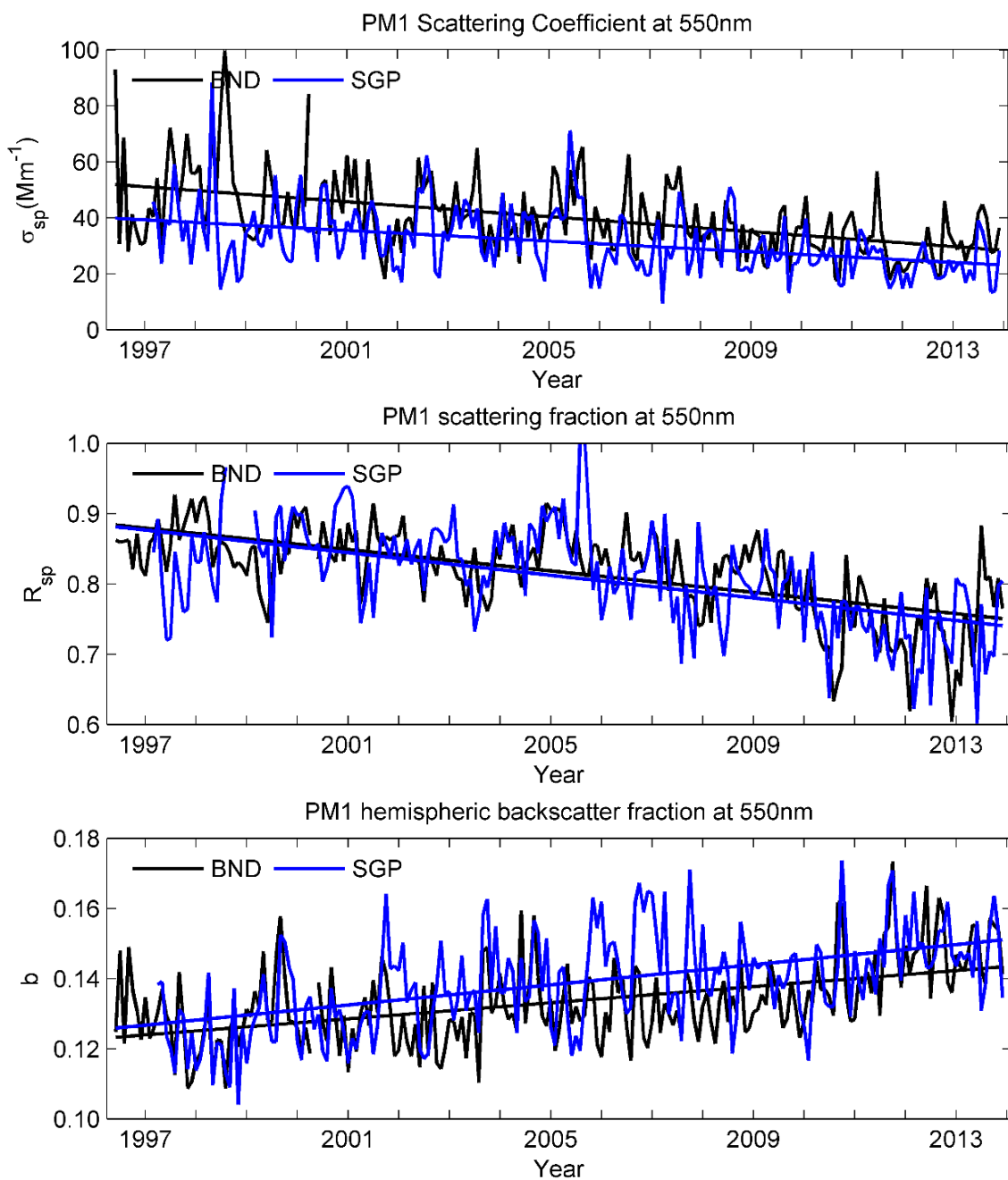


Figure 9. Time series of monthly-averaged PM1 σ_{sp} , R_{sp} , and b at 550 nm for BND (1996-2013) and SGP (1997-2013). Trend lines, representing least-squared fits of the data, are also shown.

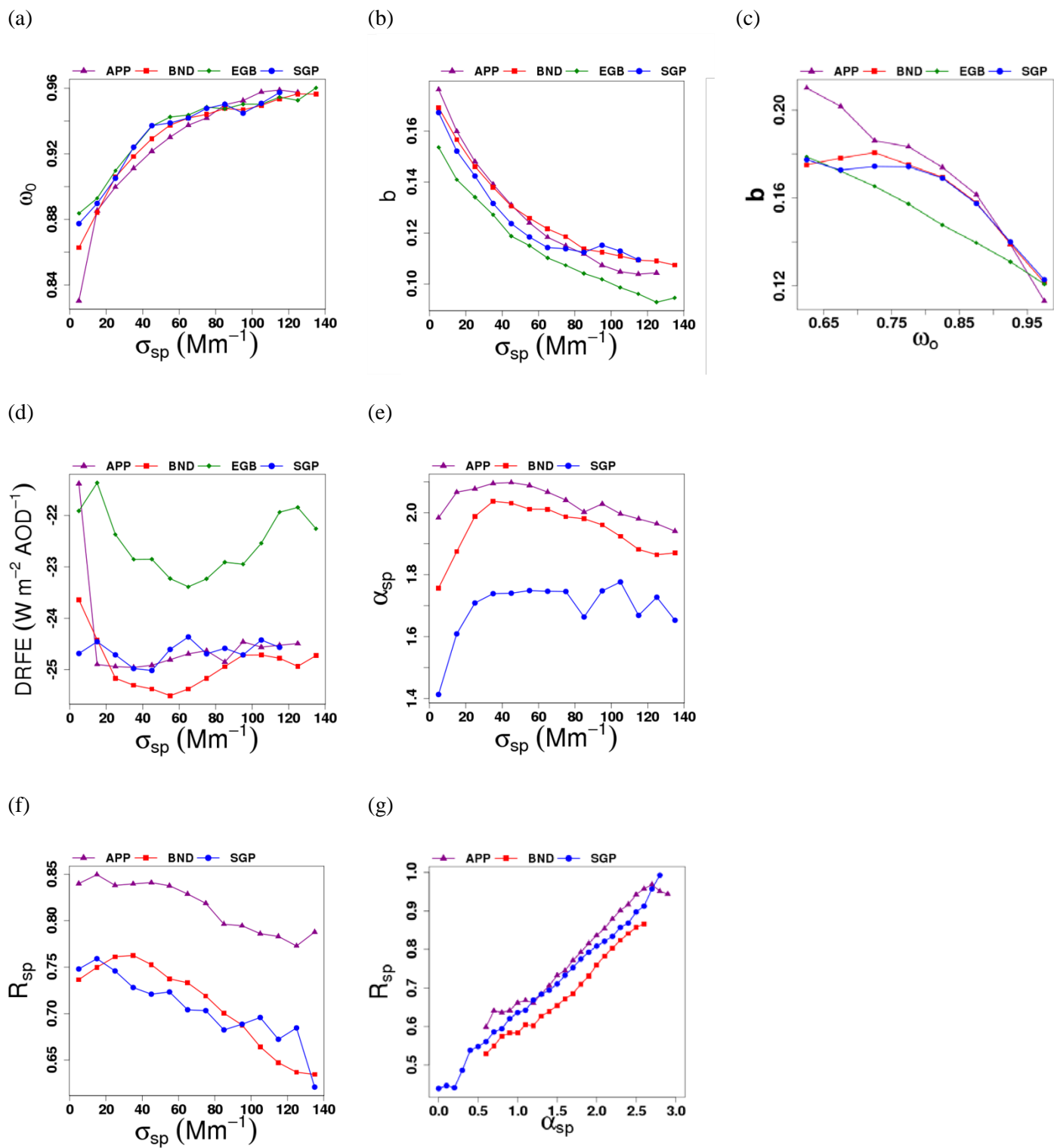


Figure 10. Systematic relationships among mean AOPs over full annual cycles of the 2010-2013 period at APP, BND, EGB, and SGP: (a) PM1 ω_0 versus PM1 σ_{sp} ; (b) PM1 b versus PM1 σ_{sp} ; (c) PM1 b versus PM1 ω_0 ; (d) PM1 DRFE versus PM1 σ_{sp} ; (e) PM10 α_{sp} versus PM1 σ_{sp} ; (f) R_{sp} versus PM1 σ_{sp} ; and (g) R_{sp} versus PM10 α_{sp} .

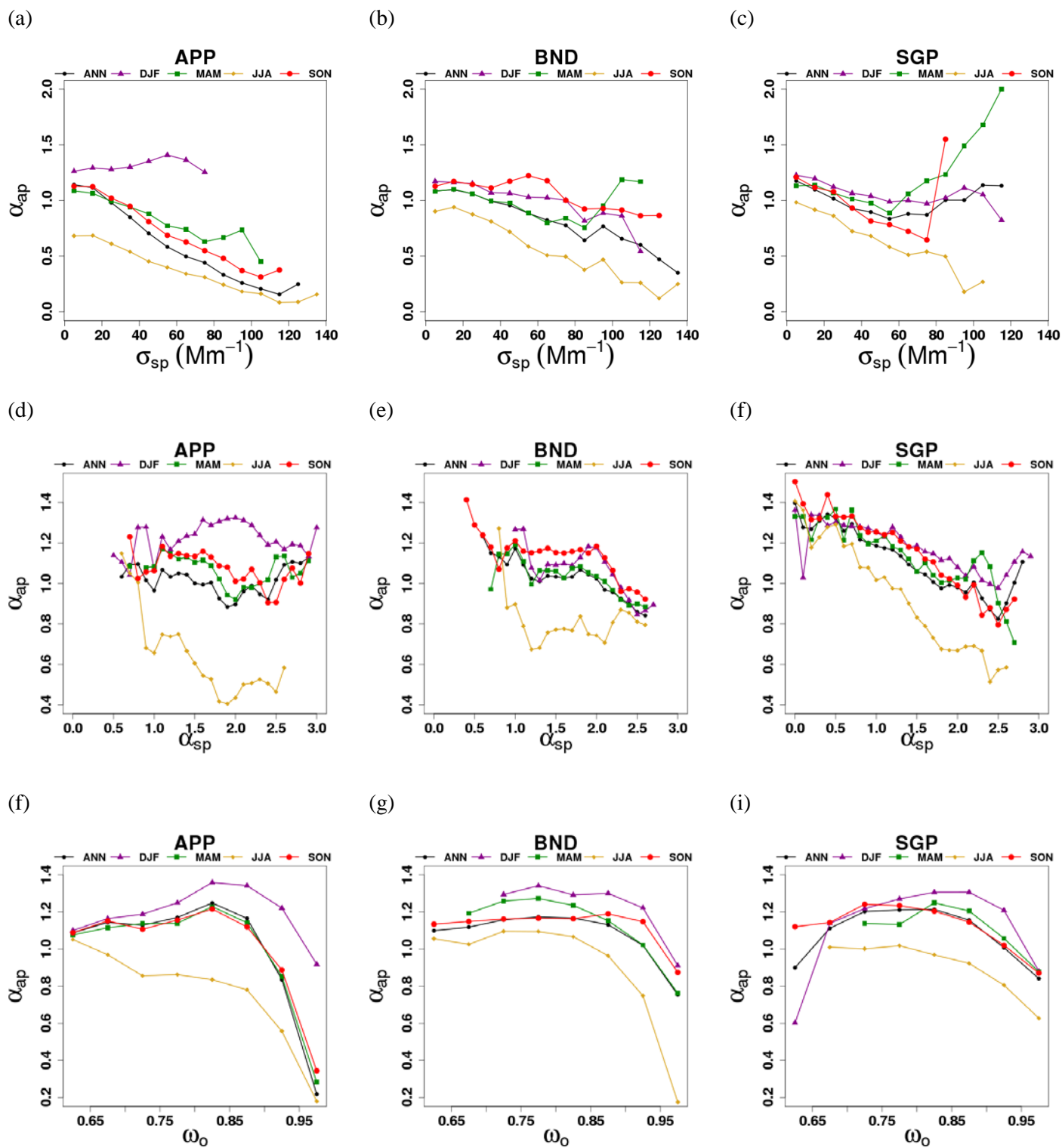


Figure 11. Systematic relationships among mean AOPs involving absorption Ångström exponent (α_{ap}) for individual seasons of the 2010-2013 period at APP, BND, and SGP: (a) α_{ap} versus σ_{sp} at APP; (b) α_{ap} versus σ_{sp} at BND; (c) α_{ap} versus σ_{sp} at SGP; (d) α_{ap} versus α_{sp} at APP; (e) α_{ap} versus α_{sp} at BND; (f) α_{ap} versus α_{sp} at SGP; (g) α_{ap} versus ω_0 at APP; (h) α_{ap} versus ω_0 at BND; (i) α_{ap} versus ω_0 at SGP.